ELUCIDATING THE IMPACTS OF STRUCTURAL HETEROGENEITY ON EXCITED STATE DYNAMICS IN SOLUTION-PROCESSED MATERIALS

by

Sajia Afrin

A dissertation submitted in partial fulfillment of the
requirements for the degree

of

Doctor of Philosophy

in

Materials Science

MONTANA STATE UNIVERSITY
Bozeman, Montana

May 2024

DEDICATION

To

my grandfather

MOHAMMAD SAIDUR RAHMAN

and

my entire family for their unconditional support, encouragement, and belief in me during the moments when I struggled to believe in myself.

ACKNOWLEDGEMENTS

I want to express my deepest gratitude to Dr. Erik Grumstrup, my advisor, for giving me the opportunity to learn and grow in the realm of ultrafast spectroscopy. Dr. Grumstrup not only guided me but also imparted to me a rigorous commitment to scientific skepticism and integrity, qualities essential for any aspiring scientist.

My heartfelt appreciation goes out to my colleagues in the Grumstrup research group. Their unwavering support, friendship, and constructive feedback have been indispensable throughout my grad school journey. I am fortunate to be surrounded by such brilliant minds who also happen to be wonderful individuals. A special thank you goes to Dr. Casey Hickey, a former colleague whose mentorship has been invaluable to me. Additionally, I extend my sincerest appreciation to my esteemed committee members, Dr. Rob Walker, Dr. Nick Stadie, Dr. Pat Callis, and Dr. Jack Skinner, for their invaluable insights, constructive feedback, and encouragement throughout my research endeavors.

My family deserves profound recognition for their steadfast support and love. I am profoundly grateful to my parents for wholeheartedly embracing and nurturing my aspirations. To Ammu-Abbu, Bubu-Dulavai, and Maa-Baba, your presence and encouragement, despite the miles between us, have been a constant source of strength.

A special tribute is reserved for my husband, Shanil, whose courage and unconditional support have been my rock. Despite the challenges of a long-distance marriage amidst my Ph.D. journey, his strong belief in me has been nothing short of remarkable. Thank you for being my pillar of strength.

TABLE OF CONTENTS

1. INTRODUCTION 1

1.1. Motivation 1
1.2. Pump Probe Microscopy 5
1.2.1. Spatially Overlapped Imaging 9
1.2.2. Kinetics 9
1.2.3. Spatially Separated Imaging 10
1.3. Solution Processed Materials 12
1.3.1. Lead Halide Perovskites 12
1.3.2. Metal-Organic Frameworks 15
1.4. Thesis Organization 19

2. INSTRUMENTATION AND SYNTHESIS 20

2.1. Instrumentation 20
2.2.1. Two-color Pump-Probe Microscope 20
2.2.2. Broadband Pump-Probe Microscope 23
2.2.3. Photoluminescence Microscope 26
2.2.2. Electron Backscatter Diffraction 28
2.2. Sample Preparation 30
2.2.1. Cesium Lead Tribromide ($CsPbBr_3$) 30
2.3.2. PCN-222 Metal-Organic Framework 31

3. IMPACTS OF INTRINSIC LATTICE STRAIN ON THE EXCITED-STATE CARRIER TRANSPORT IN LEAD HALIDE PEROVSKITE MICROCRYSTALS 32

3.1. Introduction 32
3.2. Results and Discussions 35
3.3. Conclusions 47

4. RAPID EXCITON TRANSPORT AND STRUCTURAL DEFECTS IN INDIVIDUAL PORPHYRINIC METAL-ORGANIC FRAMEWORK MICROCRYSTALS 49

Contributions of Authors and Co-Authors 49
Manuscript Information 50
4.1. Abstract 51
4.2. Introduction 52
4.3. Results and Discussion 54
4.4. Conclusions 63

TABLE OF CONTENTS CONTINUED

5. ENERGETICALLY DEPENDENT TRANSPORT AND RELAXATION DYNAMICS WITHIN A SINGLE POPHYRINIC METAL-ORGANIC FRAMEWORK MICROCRYSTAL64

Contributions of Authors and Co-Authors 64
Manuscript Information 65
5.1. Abstract 66
5.2. Introduction 67
5.3. Synthesis 69
5.4. Results and Discussion 69
5.5. Conclusions 85

6. CONCLUSIONS AND FUTURE DIRECTIONS 86

6.1. Conclusions 86
6.2. Future Work 88
6.2.1. Understanding the Soret Band Evolution 88
6.2.2. Determining the Observed Blue Shift of the $Q_x(0,0)$ Peak in Structures with Chemical Heterogeneity 90
6.2.3. Careful Synthesis and Characterization of Excited State dynamics in other Porphyrin MOF structures: 91

CUMULATIVE REFERENCES CITED 93

APPENDICES 108

APPENDIX A SUPPORTING INFORMATION FOR CHAPTER 4 109
APPENDIX B SUPPORTING INFORMATION FOR CHAPTER 5 118

LIST OF FIGURES

Figure Page

1.1. Transient pump-probe signal....6

1.2. Pump-probe imaging 11

1.3. Crystal structure of $CsPbBr_3$....13

1.4. Crystal structure of PCN-222....16

1.5. TCPP spectroscopic characterization....17

2.1. Schematic of two-color pump-probe microscope....22

2.1. Schematic of broadband pump-probe microscope....25

2.2. schematic of photoluminescence microscope....27

2.3. Schematic electron backscatter diffraction....29

2.4. Brightfield image of $CsPbBr_3$ domains....30

2.5. Brightfield image of PCN-222 microstructure....31

3.1. Schematic of band structure modification due to lattice strain....34

3.2. Imaging of PCN-222 using SEM and pump-probe microscopy....36

3.3.Transport measurements in $CsPbBr_3$....37

3.4. Radom transportation illustration....41

3.5. Strain correlation between pump-probe image and strain image....42

3.6. Band energy correlation between band energy image and pump-probe image....45

4.1.Structural characterization of PCN-222 micro rods....55

4.2.Transport measurement in PCN-2222 micro rods....57

LIST OF FIGURES CONTINUED

Figure Page

4.3. Relaxation dynamics in PCN-222 60

4.4. Spectroscopic comparison of straight and bent rods. 61

5.1. Steady-state characterization of PCN-222.....70

5.2. Spectroscopic and dynamic characterization OF PCN-222. 73

5.3. Spectral evolution within a bent structure. 77

5.4. Excitation energy-dependent relaxation dynamics.....80

5.5. Excitation energy-dependent transport measurements 83

5.6. Fluorescence measurements 84

6.1. Absorption emission spectra of TCPP and PCN-222 89

6.2. Blue shift in transient absorption spectra 91

6.3. Excited state dynamics in different porphyrin MOF structures 92

ABSTRACT

Solution-processed inorganic and organic semiconductors hold enormous promises due to their low manufacturing cost, scalability, and compatibility with flexible substrates. However, solution processing techniques do not require control over crystal growth, which can lead to structural defects within the crystal structure. The defects within solution-processed semiconductors can create significant challenges in optimizing device functionality; therefore, it is crucial to understand the impact of structural defects on photophysical properties. Traditional ensemble measurement techniques can conceal the effects of microscale structural defects on functional properties in the structure-averaged observation of solution-processed materials. The work presented in this dissertation employs time-resolved and spectrally resolved microscopy techniques to investigate the influence of structural heterogeneity on the photophysical properties of microscale solution-processed materials. Measurements collected across multiple discrete and highly crystalline domains of multiple classes of solution-processed materials have helped establish a relationship between the functionality and the local structure of these materials. Initially, the focus was on elucidating anisotropic carrier transport in lead halide perovskites by investigating lattice strain and energetic distribution in microcrystals. Later, the focus shifted towards characterizing and understanding the impact of structural defects on the excited state dynamics in another class of solution-processed material called metal-organic frameworks (MOFs). PCN-222 exhibited rapid exciton transport with time-averaged diffusion coefficients ranging from 0.27 to 1.0 cm^2/s and subdiffusive behavior, showing transport slowing on the tens of ps time scale. Subdiffusivity indicated that excited states were rapidly transported through the porphyrin network of PCN-222 before being trapped. Moreover, the first transport measurements and transient absorption microscopic measurements in PCN-222 are reported here. Photoluminescence quenching and heterogeneous relaxation pathways were noted in regions with higher structural heterogeneity. Furthermore, the spectral evolution of porphyrinic PCN-222 MOF was investigated, which revealed excitation-dependent chromophore coupling in the MOF structure. Soret band excitation with enhanced coupling can create more mobile excited states, whereas Q band excitation with reduced coupling will generate fewer mobile excited states. Excitation-dependent chromophore coupling strongly dictates the transport and relaxation properties in MOF microstructures that also illustrate the impact of structural defects on the excited state transport and relaxation dynamics. A significant spectral shift has also been observed in microrods stemming from structural heterogeneity. These findings contribute to a deeper understanding of the impact of structural defects on the photophysical properties of solution-processed materials, facilitating the development of optimized semiconductor devices for various applications. The results reported in this dissertation will not only continue to aid in the characterization of MOFs but will also advance our understanding of excited state dynamics in a variety of solution-processed materials.

CHAPTER ONE

INTRODUCTION

1.1 Motivation

Solution-processed materials hold immense promise for propelling the frontier of next-generation optoelectronics, particularly in directing revolutionary advancements in photovoltaic (PV) technologies.[1] The evolution of photovoltaic (PV) technologies stands out as a paramount and practical solution to the energy crisis caused by the depletion of nonrenewable resources, with PV devices continuously advancing through several generations.[2] PV is generally categorized according to its technological generation. The first generation (1G) of photovoltaics was developed utilizing crystalline silicon, while the second generation (2G) introduced materials such as amorphous silicon, copper indium gallium selenide, and cadmium telluride.[3, 4] Due to the high fabrication cost of 1G and 2G photovoltaics, research and development have been directed towards finding alternative solutions for photovoltaic materials.[5] Third-generation photovoltaics started employing solution-processed semiconductor materials, such as inorganic-organic perovskites, organic semiconductors, polymers, nanoparticles, and quantum dots.[6] Solution-processed materials have gained significant attention due to their increasing efficiency, low cost, scalability, and minimal environmental impact, suggesting they have the potential to revolutionize the photovoltaic industry. [7-9] In addition to photovoltaics, a plethora of optoelectronic devices, including photodetectors, photodiodes, and phototransistors, are commonly fabricated using solution processing techniques.[10] The realm of solution-processed flexible electronics and optoelectronics, exemplified by organic light-emitting diodes (OLEDs),

has garnered substantial attention due to their immense market potential across various technologies and applications. This interest stems from the ability to produce large-size, high-quality devices, paving the way for diverse and impactful advancements.

The advantages inherent in solution processing techniques have motivated the fabrication of inorganic-organic semiconductor materials from laboratory research to widespread adoption in industrial manufacturing. Solution processing enables the use of large, flexible, and lightweight substrates to deposit photovoltaic material, which results in the fabrication of low-cost light-absorbing material.[11] The versatility of solution-processing techniques is highlighted by the wide range of deposition methods available, such as sputter coating, spin coating, drop casting, dip coating, and sol-gel.[12] Another important advantage of the solution processing technique is the ability to modify the chemical composition of inorganic-organic semiconductors, which can tune the bandgap of the photovoltaic materials.[13] Tunability of the bandgap allows the utilization of a wide range of visible light to photoexcite photovoltaic materials. Overall, solution-processing techniques present an array of enticing advantages, notably their tunability, compatibility with diverse substrates, and low-temperature, low-cost fabrication processes.

The solution-processed technique has gained significant attention due to its many advantages, particularly its easy fabrication process. Unlike conventional solid-state materials, solution processing alleviates the need for meticulous control over crystallization. However, a significant challenge with solution-processed materials lies in the inherent introduction of defects stemming from uncontrolled crystal growth. Microscale defects in high-performance inorganic-organic electronics critically influence device performance by orders of magnitude.[14] The defects in solution-processed materials can be classified as either structural or chemical. Chemical defects can cause spatial variation in functionality through, for example, compositional gradients or trap gradients.[15] On the other hand, structural defects can affect both the surfaces and the bulk of the material.[16] Some well-known forms of defects developed in solution-processed thin films are polycrystallinity, interfaces, and impurities. These defects can result from the mismatch between the coefficient of thermal expansion of the substrate and the material [17, 18] or from variations in precursor concentrations within the reaction vessel during the crystal growth through solution processing.[19, 20] These disorders are an intrinsic characteristic of solution-processed materials and have long-range implications on functional properties.

To optimize solution-processed optoelectronic device functionality, it is important to have a clear understanding of how structural defects impact the functional properties of the material. The current understanding of the consequences of structural heterogeneity on functional properties in solution-processed photovoltaic material primarily relies on ensemble spectroscopic measurements. However, ensemble measurements only provide structure-averaged spectroscopic observables, which may conceal the significance of disorder in determining photophysical functionality. One way to address this limitation is through time-resolved microscopy, which

provides a means to probe the disorder at its characteristic length scale. Utilizing microscopy techniques can reveal the influence of structural heterogeneity on photophysical properties. Ultrafast microscopy, with its high spatial resolution (sub-micron), spectral resolution (~nanometer), and temporal resolution (sub-picosecond), has proven to be an effective tool for examining photoinduced excitations in disordered semiconductor materials.[21-23] Ultrafast microscopy techniques provide resolution at the length scale of structural heterogeneities, enabling a better understanding of how structural and chemical disorder influences the dynamics of photoexcited populations in solution-processed materials.

This dissertation presents research that aims to illustrate the impacts of chemical and structural heterogeneity on the functional properties of lead halide perovskites and a porphyrin-based Metal-Organic Framework. The body of work utilizes a range of experimental approaches, employing two-color and broadband ultrafast pump-probe microscopy (PPM) techniques alongside the development of a more precise and resilient method for evaluating the influence of structural defects on excited state dynamics. The remaining sections of Chapter 1 provide a brief discussion of how pump-probe microscopy can illustrate the excited state dynamics measurements in materials to remove existing knowledge gaps and introduce the solution-processed materials that will be investigated in later chapters.

1.2 Pump-Probe Microscopy

The primary focus of this dissertation is the excited state properties of solution-processed light-harvesting materials. This section briefly summarizes the principal investigation tool for this dissertation, which is ultrafast pump-probe microscopy, also known as transient absorption microscopy, to elucidate the excited state dynamics in solution-processed thin films. This nonlinear optical imaging technique utilizes a combination of femtosecond temporal resolution and diffraction-limited spatial resolution to explore the direct correlation of material morphology and excited state dynamics of nano- and microscale materials. Directly imaging the excited state dynamics can reduce the contributions of microscale chemical and structural heterogeneities that are averaged in traditional bulk spectroscopic techniques. Pump-probe microscopy typically uses two pulses of different energies. The first pulse, the pump, creates an excited state population in the material. The second pulse, known as the probe, monitors the changes in the photogenerated excited-state density over temporal and spatial evolution by measuring the intensity of the detected transmitted (ΔT) or reflected (ΔR) probe pulse.[24]

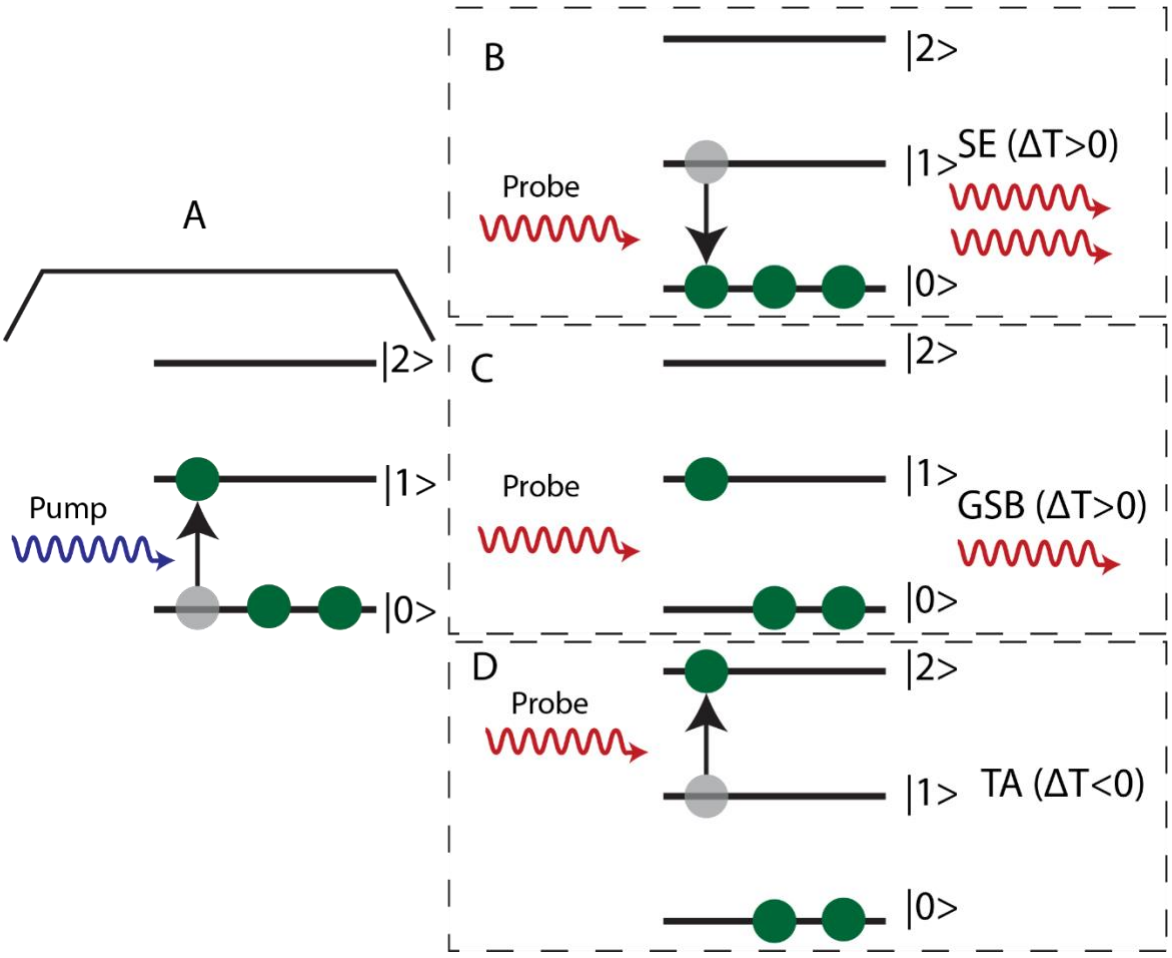

Figure 1.1 Transient pump-probe signals. (A) represents pump-induced photoexcitation, and (B), (C), and (D) illustrate SE, GSB, and TA, respectively.

In transmissive mode, the nonlinear material response arises from the pump-dependent transient change in the transmitted probe light. Depending on the transient spectrum of the material at specific pump and probe wavelengths, three transient responses may contribute to the observed signal: stimulated emission (SE), ground state bleach (GSB), and transient absorption (TA).[25] The energy level diagrams in Figure 1.1 illustrate a pump-induced excited state (panel A) and subsequent light-matter interactions, which provide the observable (panels B, C, and D). As shown in panel B, SE results in the coherent emission of a photon equal in energy to the probe

and, therefore, contributes positively to the observed signal (+ΔT). In the case of GSB (panel C), the pump-induced excitation of the material depletes the ground state population. As a result, absorption of the probe is less when there is an excited state population. Thus, GSB also contributes positively to the change in probe transmittance. Panel D depicts TA, which occurs when pump-induced excitation creates optically allowed transitions such that absorption of the probe pulse will occur, contributing negatively (-ΔT) to the detected signal. PPM can also be performed in a reflective geometry where changes in reflectivity (ΔR) are related to changes in the dielectric function. [26]

In semiconductor materials and molecules, photoexcitation with light of energy that is greater than the bandgap energy generally produces a population of free electrons and holes, which we collectively refer to as free carriers, and excitons, which are coulombically bound electron-hole pairs. When photoexcitation creates excited states, it changes the dielectric function ($\hat{\varepsilon} = \varepsilon_r' + \varepsilon_r^{"}$) of the material.[27-30] The dielectric function and the complex index of refraction is related by Equation 1.1 where $\hat{n}$ is the complex index of refraction, n is the real part of refractive index and k is the extinction coefficient.

$$\hat{\varepsilon} = \hat{n}^2 = (n + ik)^2 \qquad (1.1)$$

When photoexcitation generates excited states in the material, it causes a change in the dielectric constant in proportion to the density of free charges. In the limit where the probe energy is significantly lower than the material bandgap, the value of k approaches 0. Consequently, photo-induced changes in the refractive index can be minimized to the real component of the complex refractive index function ($\varepsilon \approx n^2$). The relationship between the

photogenerated carrier density (N) and the change in refractive index (Δn) can be expressed using Eq. 1.2 below, where q is the fundamental charge of an electron, τ is the free carrier mean scattering time, m^* is the optical mass of the carrier, n_0 is the ground state refractive index of the material, ε_0 is the static permittivity and ω is the angular frequency of the probe pulse.[31]

$$\Delta n = -\frac{Nq^2\tau^2}{2m^* n_0 \varepsilon_0 (1+\omega^2\tau^2)} \qquad (1.2)$$

Since the change in reflectance scales with Δn, the observable is the pump-induced change in the probe light $\frac{\Delta R}{R} = \frac{4\Delta n(1+\Delta n * n_0 - {n_0}^2)}{(n_0-1)^2(1-\Delta n+n_0)^2}$. Experiments designed to detect changes in the transmitted or reflected probe intensity are referred to as transient absorption experiments. With Equation 2 in consideration, the observed transient absorption signal exhibits a direct proportionality to the density of photoexcited carriers. As a result, the movement and recombination processes of excited state within the material can be probed with pump-probe microscopy. Figure 1.2 illustrates three types of pump-probe measurements: spatially overlapped imaging, spatially separated imaging, and excited state kinetics in panels A, B, and C. These methods provide a unique understanding of excited state dynamics in diffraction-limited volumes of complex materials, as discussed below.

1.2.1 Spatially Overlapped Imaging

Pump-probe microscopy (PPM) collects spatially overlapped images by raster scanning both pump and probe pulses with a fixed temporal delay across the sample surface. The transient signal can manifest as any of the three processes described in Figure. 1.1, while the signal magnitude is proportional to the number of excited states, as discussed above. Panel A of Figure. 1.2 shows an example of the spatially overlapped image of a metal-organic framework PCN-222 microwire at 1 ps time delay. The spatial resolution of the images is acquired by the product of the point spread functions of the pump and probe beams. Spatially overlapped images collected at increasing pump-probe time delays can be used to build a spatiotemporal map of the excited state across individual domains.

1.2.2 Kinetics

The recombination mechanism of the excited state is monitored by the excited state decay kinetics, which illustrates excited state relaxation pathways (Figure 1.2 panel C). Decay kinetics are collected by spatially overlapping the pump and probe beams while varying them temporally through a translation stage. Kinetics measurements determine the precise overlap of the pump and probe pulses, which enables us to probe specific time points in the progression of the excited state. The lifetimes of the excited state population can be determined by fitting the kinetics to an exponential decay model given by equation 1.3.

$$f(x) = \sum_{i=1}^{n} A_i e^{-t_i x} \qquad (1.3)$$

Excited state kinetics measurements can be used to determine the power-dependent regime for a material if the relaxation dynamics are sensitive to the excitation density. In that case, increasing excitation pump fluence creates more excited states that leads to faster relaxation as a consequence of nonlinear exciton–exciton annihilation processes. The power dependence on the relaxation dynamics suggests that the excitons are highly mobile due to the interactions among excitons.[32-34] Studies of the recombination dynamics are essential for attaining an understanding of recombination of materials. In Chapter 4, we will illustrate power dependence relaxation dynamics and global fits to the decay kinetics in more detail. Exciton transport can be measured by spatially separated imaging, which we will discuss later on.

1.2.3 Spatially Separated Imaging.

Spatially separated pump-probe images are utilized to determine how fast the photoexcited population moves through a material. The spatial and temporal progression of the excited state is used to calculate the diffusion coefficients. To capture the evolution of the excited state over time, images are obtained by spatially scanning the pump beam over the fixed probe beam at a series of delay times using galvanometer mirrors. The excited state populations move from high excitation density to low-density regions with time. Spatially separated images at a specific delay time (Δt) demonstrate the spatial distribution of the excited state population (figure 1.2 panel B). Profiles of the time (Δt) dependent images are obtained by integrating the spatially separated images along a particular angle. As the excited state population tends to diffuse with time, the width of the profile broadens as a function of Δt. The excited state diffusion coefficients can be quantified by plotting the mean square deviation (MSD) of the full-width-half-maximum (FWHM) of the integrated population profiles as a function of delay time

(Δt). Exciton transport occurs through diffusion processes, with a hopping mechanism directing transport from high to low areas of exciton concentration due to population gradient.[35] One method to estimate excitation energy transfer is through Förster resonance energy transfer theory. Förster-limited diffusion coefficient can be estimated by Förster resonance energy transfer theory. The details of the calculation to estimate the diffusion coefficient are shown in APPENDIX A.

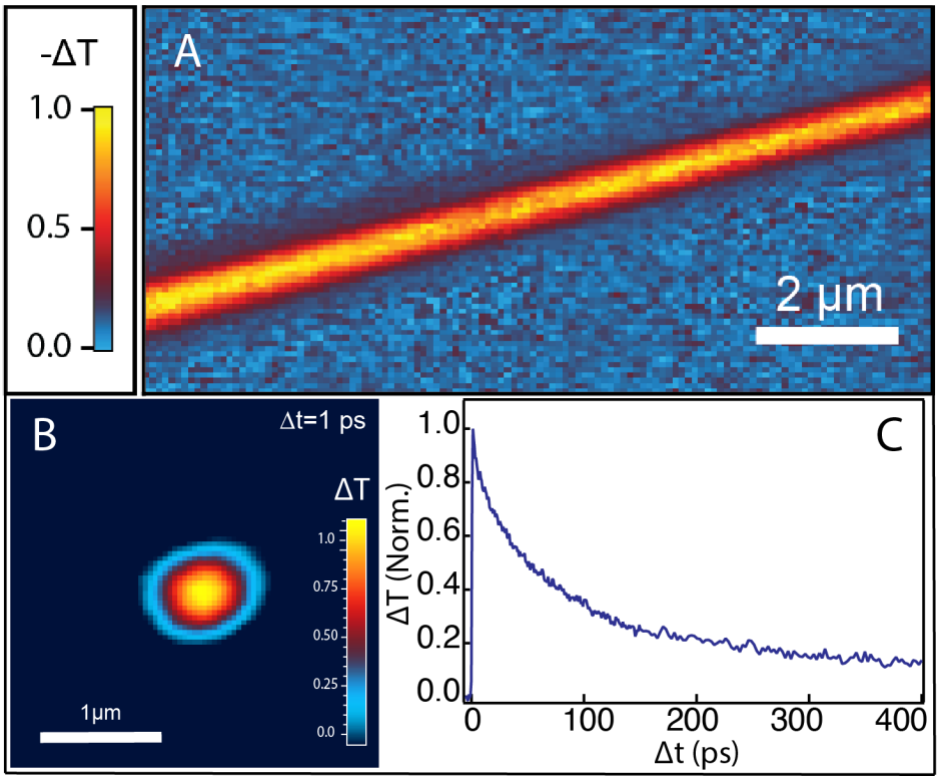

Figure 1.2 (A) Spatially overlapped image of a MOF microrod. B) Spatially separated image of excited state population (t = 1 ps) upon photoexcitation of a MOF microrod. (C) Excited state kinetics of excitons in a MOF microrod.

1.3 Solution-Processed Materials

This thesis explores two types of solution-processed material: lead halide perovskite and metal-organic frameworks, which are discussed below.

1.3.1 Lead Halide Perovskites

Perovskite is a calcium titanate ($CaTiO_3$) mineral, discovered by Gustav Rose in 1839 and named after Russian mineralogist Lev Perovski.[36] Since then, any compound with a crystal structure that follows the same form, ABX_3, is also called a perovskite. In the case of halide perovskites, the ABX_3 structure, a divalent metal (B) coordinates with six anions (X) to form corner-sharing octahedra $[BX_6]^{4-}$ surrounds an A-site cation (shown in Figure 1.3). For lead halide perovskites, the divalent metal is lead (Pb), X represents I^-, Br^-, or Cl^-, and the A-site cation is typically cesium (Cs^+), methylammonium (CH_6N^+), or formamidinium ($CN_2H_5^+$).[6] Among the enormous number of lead halide perovskites, the work described in this dissertation focuses on only lead bromide perovskites ($CsPbBr_3$). At room temperature, $CsPbBr_3$ holds an orthorhombic crystal structure, shown in Figure 1.3. $CsPbBr_3$ is a direct bandgap semiconductor, where the energy required to create an excited state in the material is determined by the bandgap energy (E_{bg}=2.3 eV).[37]

Despite being a very promising class of semiconductors for high-performance optoelectronics, lead halide perovskite thin films show substantial microscale heterogeneity in optoelectronic properties such as device performance.[38] Perovskite films have shown an emission heterogeneity on the microscale, where the PL lifetime and intensity have been reported to vary between different grains in the highest-performing polycrystalline films.[39] Optoelectronic properties such as charge carrier diffusion lengths,[40] photocurrent, and open-circuit voltage have

shown microscale spatial heterogeneity in solar cell devices.[41] Structural defects act as non-radiative recombination centers in semiconductor materials and can strongly impact the charge-carrier lifetime and recombination.[42] Furthermore, perovskite films have shown some degree of lattice strain, which directly influences the macroscopic optoelectronic properties and stability.[18] However, the current understanding of strain in perovskite material is derived from structure-averaged bulk measurements, where photophysical observables are typically averaged over obscuring the direct impact of structural defects.

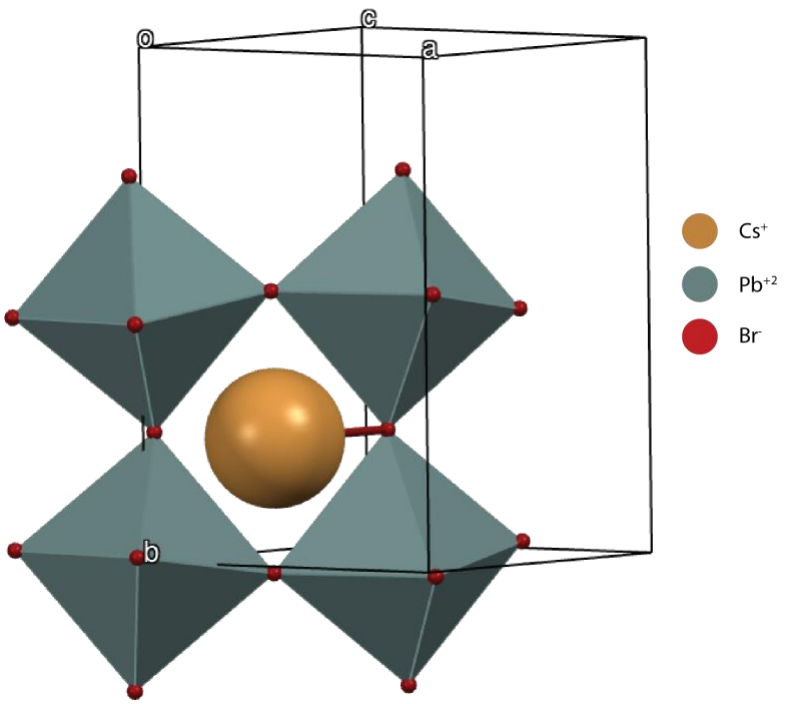

Figure 1.3: Octahedral Crystal structure of $CsPbBr_3$ perovskite material.

In recent years, a handful of microscopic studies have been carried out to investigate ultrafast dynamics in lead halide perovskites.[17, 43] Ultrafast excited state dynamics in perovskite microplates show trap-mediated inhomogeneous diffusive motion studied through time-resolved photoluminescence spectroscopy.[43] Trap density has been mapped using ultrafast photoemission electron microscopy, illustrating bulk shallow trap sites and surface deep traps.[15] Non-radiative recombination reveals that local strain leads to defects such as halide vacancies associated with local non-radiative decay.[17] Nevertheless, the direct characterization of excited state transport and quantifying microscale local lattice strain still remains undetermined. Establishing a correlation between the microscale lattice strain and excited state dynamics is essential to understanding the impact of structural heterogeneity. Chapter 3 attempts to elucidate excited state transport in lead halide perovskites utilizing pump-probe microscopy. The chapter also investigates structural heterogeneity by measuring lattice strain to determine the impact of structural heterogeneity on the excited state dynamics in lead halide perovskites.

1.3.2 Metal-Organic Framework

Metal-organic frameworks (MOFs) are a class of molecular assemblies in which organic linkers connect metal clusters, forming an ordered porous network of chromophores.[44-47] These frameworks have been the subject of immense scientific interest for their functional properties, such as high porosity[48], large specific surface area[49], tunability[50], photocatalysis,[51] and diversity of topological structure[52] . Light active metal-organic frameworks exhibit great potential in light harvesting and photochemical applications. Densely packed chromophores in a highly ordered structure achieve advantageous photophysical properties, such as high extinction coefficients and efficient energy transfer.[51, 53, 54] Porphyrin-based MOFs, like PCN-222, are interesting systems

due to their exceptional chemical stability, even under harsh experimental conditions, and their diverse range of functionalities, including catalysis, light harvesting, gas storage, and sensing.[55-58] PCN-222 (or MOF-545), based on tetrakis (4-carboxyphenyl)-porphyrin (H_2TCPP), is a highly stable mesoporous zirconium−porphyrin MOF where the H_2TCPP ligand in PCN-222 functions as a visible-light-absorbing ligand linked with zirconium (Zr_6) metal clusters.[56, 59] The crystal structure of PCN-222 is shown in Figure 1.4 along different crystal orientations.

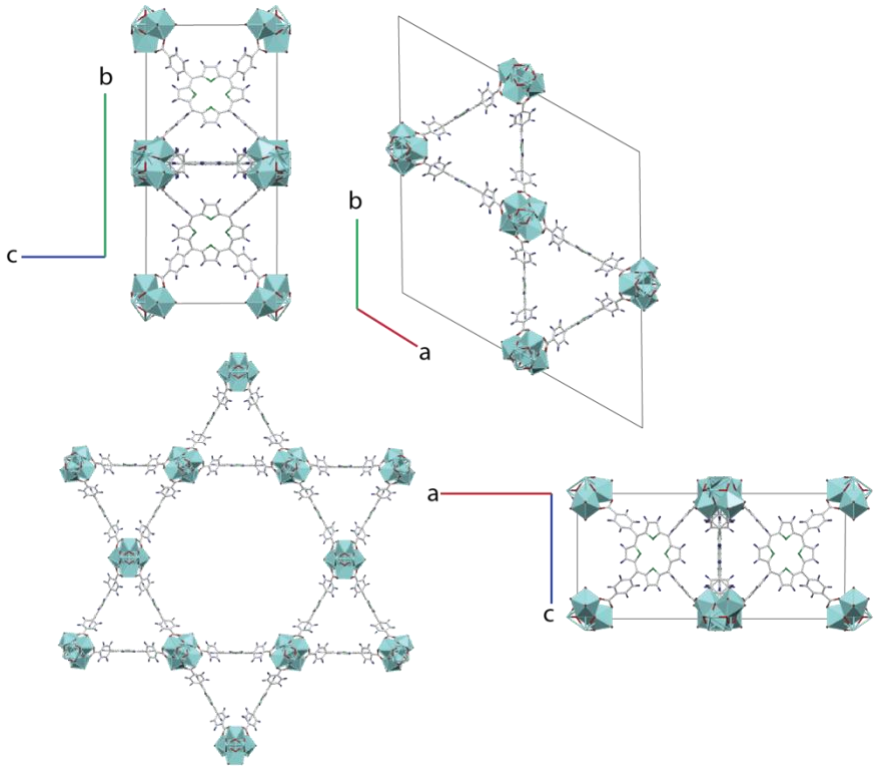

Figure 1.4 Unit cell of PCN-222(fb) representing planes (100) (top, left), (001) (top right), and (010) (bottom, right). Expanded structure of the polymer in the plane (100) (bottom, left).

The H_2TCPP ligand in PCN-222 functions as a visible-light-harvesting unit. The spectroscopic character of ligand TCPP has been extensively studied in the last few decades. The steady-state absorption spectra (Figure 1.5 panel A) show the $S_{(0,0)}$, $Q_{y(0,1)}$, $Q_{y(0,0)}$, $Q_{x(0,1)}$, and $Q_{x(0,0)}$ absorption bands. [60] The characteristic S and Q bands arise from electronic transitions from two HOMOs (a_{1u} and a_{2u} orbital) to two LUMOs (degenerate e_g orbitals) (Figure 1.5 panel B). The transitions between these orbitals and orbital mixing split the excited states, creating a higher energy state with greater oscillator strength, giving rise to the Soret band, and a lower energy state with less oscillator strength, giving rise to the Q-bands [61]. According to the selection rule, the allowed, higher energy singlet is the (HOMO→LUMO+1) transition and is termed the Soret (S or B) band. The lower energy singlet is pseudo parity forbidden Q band transitions (HOMO→LUMO) (relative low intensity of the Q bands in figure 1.3 inset), which are split by vibronic coupling and macrocycle protonation in free base porphyrin.[62] Even though H_2TCPP is a widely studied molecular system, when it is coupled with the metal clusters in MOF structures, the photophysical changes, such as the absorption spectra and their relaxation dynamics, are not well understood.

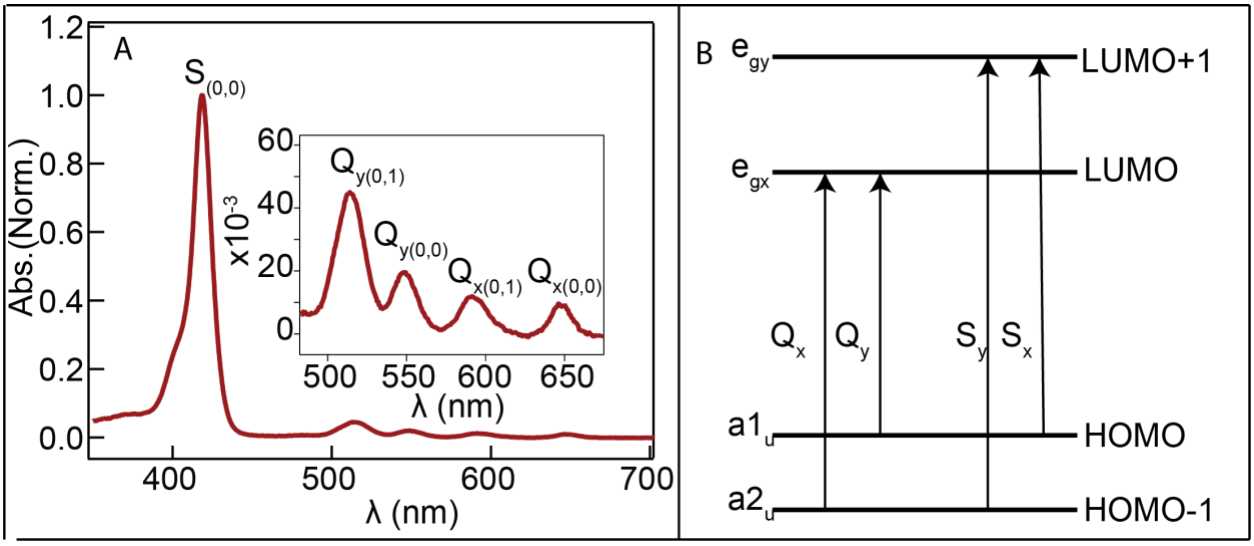

Figure 1.5: TCPP Spectroscopic characterization. A)Normalized steady-state absorption of TCPP. B) drawing of the four-energy level and transition giving rise to Soret and Q bands.

A very few ultrafast spectroscopic studies have explored the excited state dynamics of porphyrinic metal-organic frameworks. Steady-state and time-resolved photoluminescence studies have explored photophysical aspects of a few MOF structures. [53, 54, 63] A highly chromophoric bodipy and porphyrin-based MOF exhibits efficient and rapid energy transfer between ligands.[53] Internal fluorescence quenching experiments demonstrate an incoherent, hopping-type mechanism for excitation energy transfer from the freebase porphyrin linkers to N-protonated porphyrin linkers in PCN-223 MOF.[64] A transient absorption study on PCN-222 exhibits electron-hole separation via electron trap states.[65] Nonetheless, photophysical investigations of porphyrinic MOFs have been limited to ensemble techniques till-date, providing only structure-averaged observables and are susceptible to solvent effects.

The evolution of spectroscopic properties of porphyrin ligands when integrated into MOF structure has never been investigated to our knowledge. Microscopic investigations of excited state transport properties and radiative-nonradiative relaxation dynamics of single-crystalline MOF structures in the solid phase have also remained unexplored. Understanding the influence of structural heterogeneity on the functional properties within porphyrinic MOF structures requires the utilization of time-resolved and spectrally resolved microscopic measurements. To address this existing knowledge gap, Chapters 4 and 5 will focus on investigating PCN-222 microstructures using two-color and broadband pump-probe microscopy to uncover the intricacies of excited state dynamics in porphyrin MOFs.

1.4 Thesis Organization

The remainder of this dissertation is organized as follows:

Chapter 2 reports a detailed explanation of the instrumentation used in the experiments discussed in the following chapters. Our focus is on characterizing excited state dynamics. Specifically, we cover ultrafast two-color pump-probe microscopy, ultrafast broadband pump-probe microscopy, electron backscatter diffraction (EBSD), and photoluminescence microscopy techniques, including detailed instrumentation and measurement procedures.

Chapter 3 illustrates diffusion measurements and the quantification of structural heterogeneity in single-crystalline cesium lead tribromide perovskite domains. Additionally, the chapter explores how structural defects impact the excited state dynamics by analyzing the correlation between diffusion coefficients and energetic distribution.

Chapter 4 provides insight into the rapid transportation of excitons through a chain of porphyrin networks. This chapter also highlights the impact of microscale structural defects on transport and relaxation in individual PCN-222 microcrystals.

Chapter 5 reports the spectral evolution of broadband ultrafast pump-probe microscopy on individual structures of PCN-222 micro rods. We also unravel the rapid exciton transport, energetically dependent transport, and relaxation dynamics within a single porphyrinic metal-organic framework microcrystal.

Chapter 6 delves into the far-reaching implications of the research delineated in this dissertation, presenting several future challenges aimed at advancing the comprehension of the photophysics of PCN-222 MOF.

CHAPTER TWO

INSTRUMENTATION AND SYSTHESIS

2.1 Instrumentation

2.1.1 Two Color Pump-probe Microscope

The primary spectroscopic tool used for this dissertation is an ultrafast pump-probe microscope. The instrument described here is called a two-color pump-probe microscope because it utilizes two pulses of different energies: a pump pulse (400nm) that creates the excited state population and a probe pulse (800 nm) that monitors the spatial and temporal evolution of the excited state population through the changes in the detected probe intensity. Figure 2.1 illustrates a schematic diagram of the two-color pump-probe microscope used for the experiments presented in this dissertation. The homebuilt pump-probe microscope used here is based on a Ti:Sapphire oscillator (Spectra-Physics MaiTai) that produces 70 fs pulses centered at 800 nm. The fundamental is tunable in the spectral range of 690-1040 nm. The primary beam from the oscillator is split by a 50:50 beam splitter. Both pump and probe are passed through acousto-optic modulators to control the repetition rate. The experiments presented in this dissertation have used the repetition rate from 1 to 8 MHz. The pump is further modulated with a 50% duty cycle square wave at 101 kHz referenced to a lock-in amplifier. The pump is frequency doubled in a BBO (400 nm) and coupled onto a pair of computer-controlled galvanometer-mounted mirrors at the conjugate plane of a 4f telescope. Galvanometer-mounted mirrors are used to achieve the spatial control of the pump and probe. The other conjugate plane of the 4f lens system is the back aperture of a 100X achromat objective, which serves to focus the beam onto the sample. To

control the temporal coordinates of the probe relative to the pump, the probe is passed onto an optical delay stage and then coupled collinearly with the pump between the objective and the last lens of the 4f telescope with a dichroic beam splitter. The polarization of the pump and the probe can be independently controlled. The sample is mounted vertically on a piezoelectric translation stage (Mad City Labs). The transmitted pump and probe are collected with a condenser, the pump is filtered out with a long pass filter, and the probe is focused onto a balanced photodiode. The signal is demodulated using an SR830 lock-in amplifier and recorded using a National Instruments DAQ card. [66] The homebuilt pump-probe microscope described above is configured such that three types of measurements can be collected: decay kinetics, spatially overlapped images, and spatially separated images that were described in Chapter 1. Spatially overlapped images are collected by raster scanning both pump and probe pulses using the nano piezoelectric translation stage at a fixed temporal delay across the sample surface (spatially overlapped image shown at nanopiezo stage in Figure 2.1). Kinetics traces are collected by spatially overlapping the pump and probe beams while varying them temporally through the translation stage (Decay kinetics shown at the delay stage in Figure 2.1). Spatially separated images are collected by spatially scanning the pump beam using galvanometer mirrors over the fixed probe beam at a series of delay times (spatially separated spot at 1 ps shown at the galvanometer mirrors in Figure 2.1). The schematic shown here is in transmissive geometry, but each measurement can be performed by detecting the reflected probe light as well.

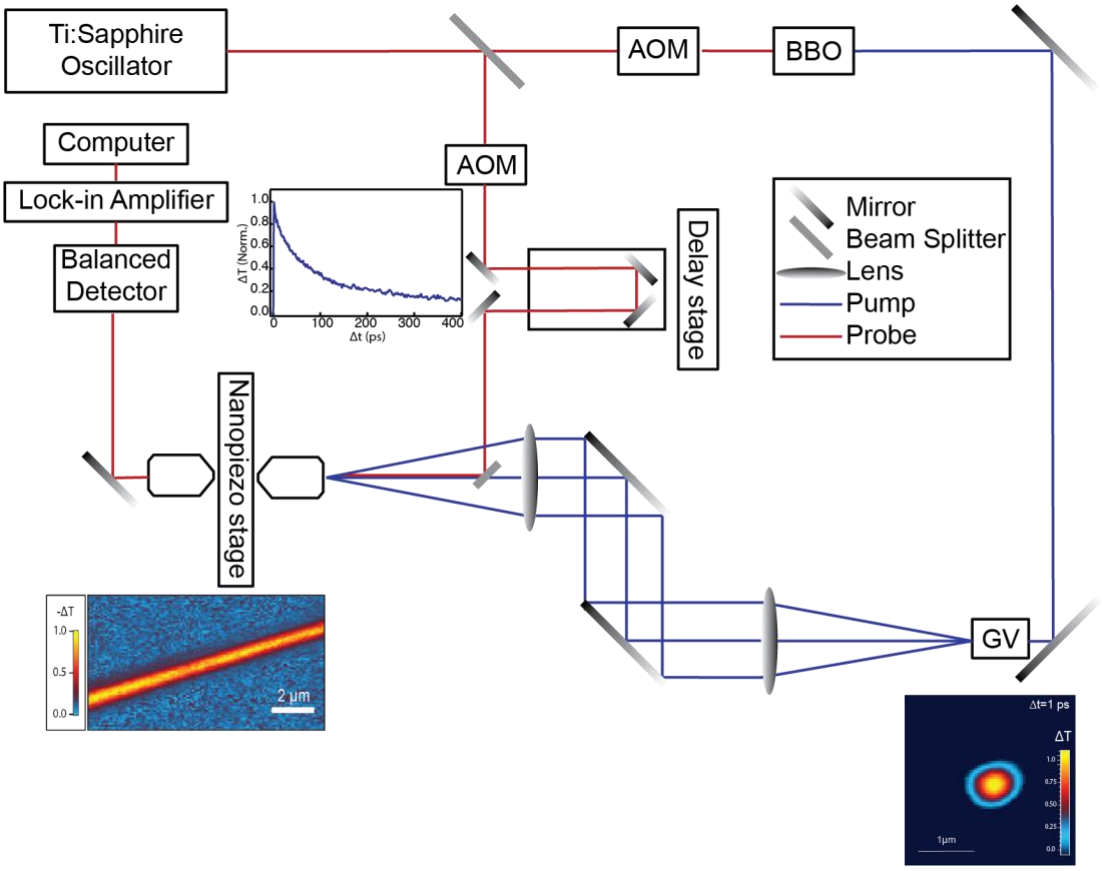

Figure 2.1. Diagram of a pump-probe microscope in transmissive mode. The fundamental out of the laser (red) is split into two lines: The probe (red) and the pump (blue). Both beams are recombined using a dichroic beam splitter and directed onto the back aperture of a 100x objective. Pump-induced changes in the transmitted probe beam are detected using a balanced photodiode and lock-in amplifier. Spatially overlapped imaging, Kinetics, and spatially separated imaging that were discussed in Chapter 1 earlier are shown here.

2.1.2 Broadband Pump-Probe Microscope

A different pump-probe instrument is utilized for broadband pump-probe microscopy measurements. Figure 2.2 illustrates a schematic diagram of the broadband pump-probe microscope. The primary difference between two color and broadband pump-probe microscopes is that the broadband microscope can measure excited state spectra and observe the spectral and temporal evolution utilizing a white light continuum as the probe beam. The broadband pump-probe microscope is based on a Coherent Monaco 40W 1035nm fiber laser with a 125 kHz repetition rate and a standard pulse width of ~300fs. The probe beam is focused into a 1 cm thick yttrium aluminum garnet (YAG) crystal to generate the white light continuum (WLC) and collimated to the microscope objective. The pump is modulated at 16 kHz with a 50% duty cycle by an acousto-optic modulator. The pump is passed through a BBO to generate a second harmonic (517 nm), then passed onto an optical delay line and coupled onto a pair of computer-controlled galvanometer-mounted mirrors at the conjugate plane of a 4f telescope. The other conjugate plane of the 4f lens system is the back aperture of a 100X, 0.9 NA achromat objective, which serves to focus the beam onto the sample. The WLC probe is collimated with an achromatic lens, and a short pass filter is used to filter out the IR components. The WLC probe is coupled collinearly with the pump between the objective and the last lens of the 4f telescope with a dichroic beam splitter. The pump and WLC probe are both polarized vertically (with respect to the optical table). The polarization of both beams can be controlled independently. The sample is mounted vertically on a piezoelectric translation stage (Mad City Labs, Nano-H100). The transmitted pump and probe are collected with a condenser, the pump is filtered out with a long pass filter, and the broadband probe is dispersed in a spectrometer consisting of two 50mm 1.8F camera lenses and a holographic grating. The dispersed probe focused onto a Teledyne DALSA

OctoPlus line camera with 2048 pixels.[67] The line camera is connected to a computer and sends collected line data frames to a LabVIEW software VI with a guided user interface (GUI). The line acquisition is triggered at a rate of 62.5kHz, while frames are triggered at a different rate of 78.125Hz. The OctoPlus line camera modulates line acquisition in two different trigger levels because it uses two different ADCs with different noise characteristics to bin the signal from sequential lines. Collecting two lines with the pump on and two with the pump off averages the noise of the two ADCs, minimizes the introduction of artifacts, and provides us with a spectrum with 1024 pixels. The spectral range and the number of pixels determine the spectral resolution of the instrument (0.57 nm). Furthermore, the line rate of the camera can be controlled depending on the stability of the material. A lower line rate allows for the integration of a greater number of pulses and utilization of more of the dynamic range of the camera, which reduces the relative amplitude of the electronic noise of the instrument. The broadband instrument provides the ability to collect time-resolved and spatially resolved transient spectra. Broadband pump-probe microscope can also perform three types of measurements: decay kinetics, spatially overlapped images, and spatially separated images, as described in Chapter 1. Spatially overlapped images are collected by raster scanning both pump and broadband probe pulses using the nano piezoelectric translation stage at a fixed temporal delay across the sample surface. In this case, a transient spectrum for each pixel of the spatially separated image is acquired. The spatial analysis of spectral changes will be discussed in detail in Chapter 5. Kinetics traces are collected by spatially overlapping the pump and broadband probe beams while varying them temporally through the translation stage. For each time point, a corresponding transient spectrum is obtained, and the spectrally resolved decay kinetics are shown in Figure 2.2.

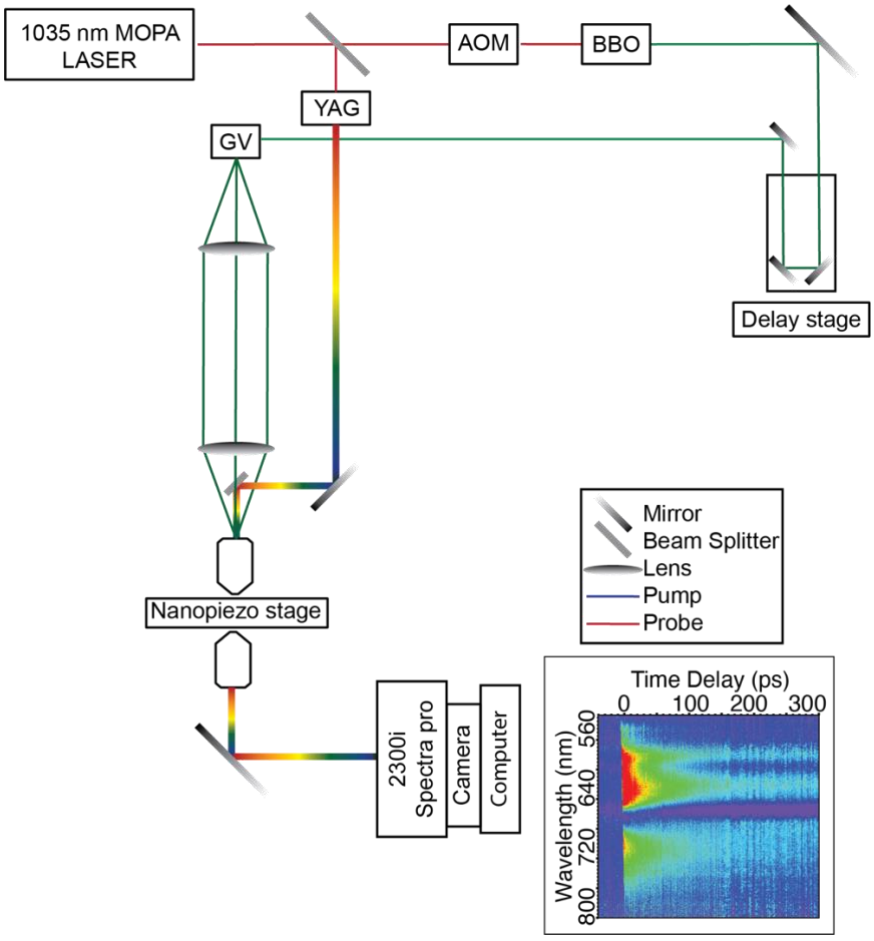

Figure 2.2. Diagram of a broadband pump-probe microscope in the transmissive mode. The fundamental out of the laser (red) is split into two lines: The probe (rainbow) and the pump (green). Both beams are recombined using a dichroic beam splitter and then directed onto the back aperture of a 100x objective. Pump-induced changes in the transmitted broadband probe beam are detected using a spectrometer and a line camera. (spectrally resolved kinetics are shown).

2.1.3 Photoluminescence Microscopy

Photoluminescence microscopy measurements involve capturing the emitted photons resulting from material photoexcitation. The two-color pump-probe microscope explained above has been modified to collect the emission due to 400 nm photoexcitation. Figure 2.3 illustrates a schematic diagram of the two-color pump-probe microscope with measuring photoluminescence measurement capabilities. The photoluminescence (green beam) is guided to a home-built spectrometer through a 450 nm long pass and a 750 nm short pass filter to eliminate the pump and probe beam, respectively. Subsequently, the emission is directed to the spectrometer via a 25 μm fiber optic cable. The homebuilt spectrometer consists of two 50 mm 1.8F camera lenses and a diffraction grating. The diffraction grating in the spectrometer separates the spectral components of the emission beam, and the dispersed emission is focused onto a FLIR BFS-U3-16S camera. The camera is connected to the computer, and LabVIEW software is used to plot the emission intensity as a function of wavelength. The spectral resolution of the instrument is determined to be 0.2 nm. Figure 2.3 shows a photoluminescence spectrum collected from the location indicated on the pump-probe image through the photoluminescence microscopy setup. The primary advantage of this instrument is the unique capability to collect the pump-probe signal and photoluminescence simultaneously.

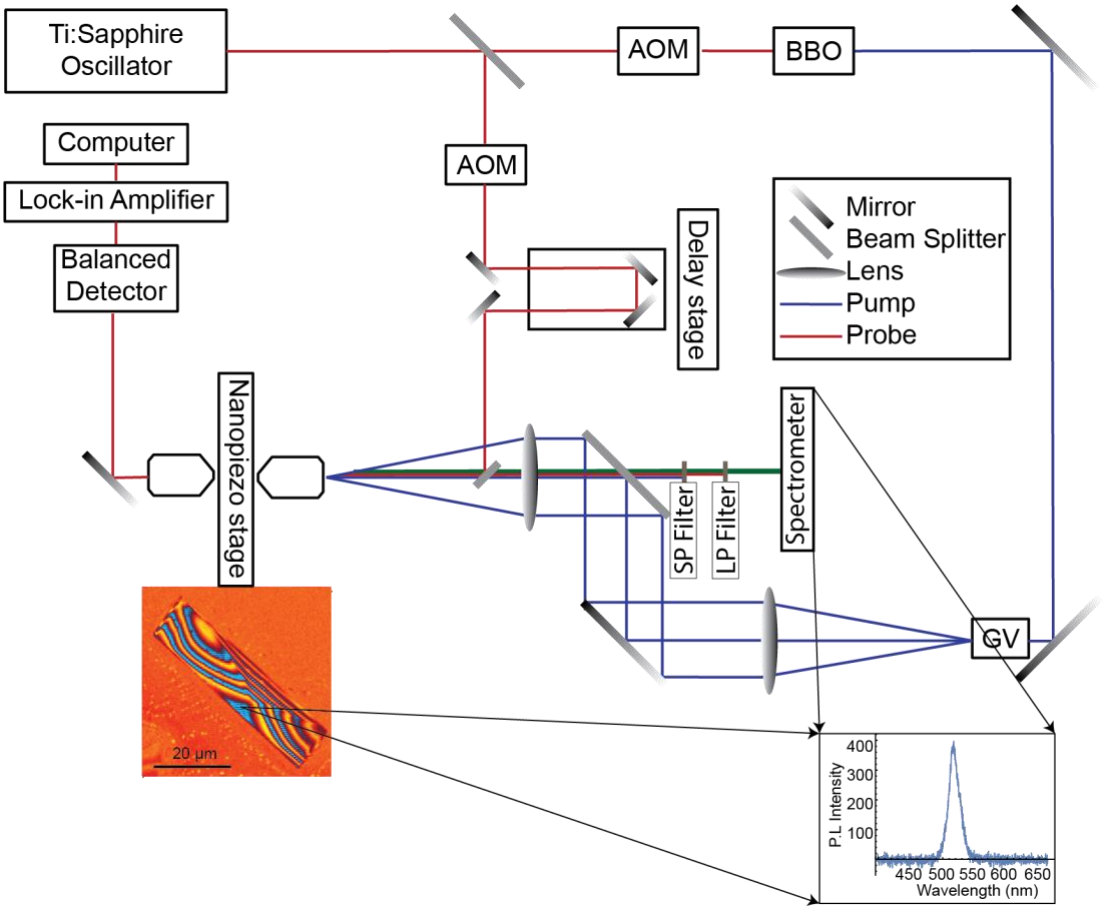

Figure 2.3: modification of pump-probe microscope to measure photoluminescence (green beam) simultaneously with the pump-probe imaging.

2.1.4 Electron Backscatter Diffraction (EBSD)

Electron backscatter diffraction (EBSD) is a powerful technique to determine spatial variation of crystal orientation. EBSD is a crystallographic characterization technique based on scanning electron microscopy. Figure 2.4 Panel A shows a schematic arrangement of EBSD inside the SEM chamber. Physical Electronics 710 scanning Auger nanoprobe was used to perform EBSD. The crystalline sample is kept at a high angle (typically 70°) in the chamber. The primary electron beam is focused on the sample surface about 10-200 nm. The incident electrons from the primary 20 keV electron beam diffract from the planes of atoms in the crystal lattice following Brag's law. These diffracted electrons will form a pair of large-angle cones representing each diffracting plane. In Figure 2.4 panel B, the blue and red cones correspond to the plane electrons are diffracting from. The diffracted electrons will create a pair of lines for each lattice plane on the phosphor screen shown in Figure 2.4 panel B. This pair of lines are called Kikuchi Lines. Incident electrons diffract from a number of lattice planes in the sample and create a number of kikuchi lines on the phosphor screen. All the overlapping Kikuchi lines will form a distinct line pattern for a distinct crystal orientation, which is called the Kikuchi line pattern (shown in Figure 2.4 panel A). When the incident electron beam is spatially scanned over an area on the sample, a distinct kikuchi pattern is collected for each location on the region. The experiments reported in this dissertation were conducted at a spatial resolution of 400 nm. Each pattern created on the phosphor screen of the CCD camera is then sent to the computer to determine the phase and orientation of the sample. A commercial computer software (EDAX's TEAM) was used to fit each diffraction pattern to a user-defined reference pattern constructed

from structure data obtained on the Crystallographic Open Database (COD).[68, 69] The analysis of Kikuchi line patterns will discussed in detail in Chapter 3.

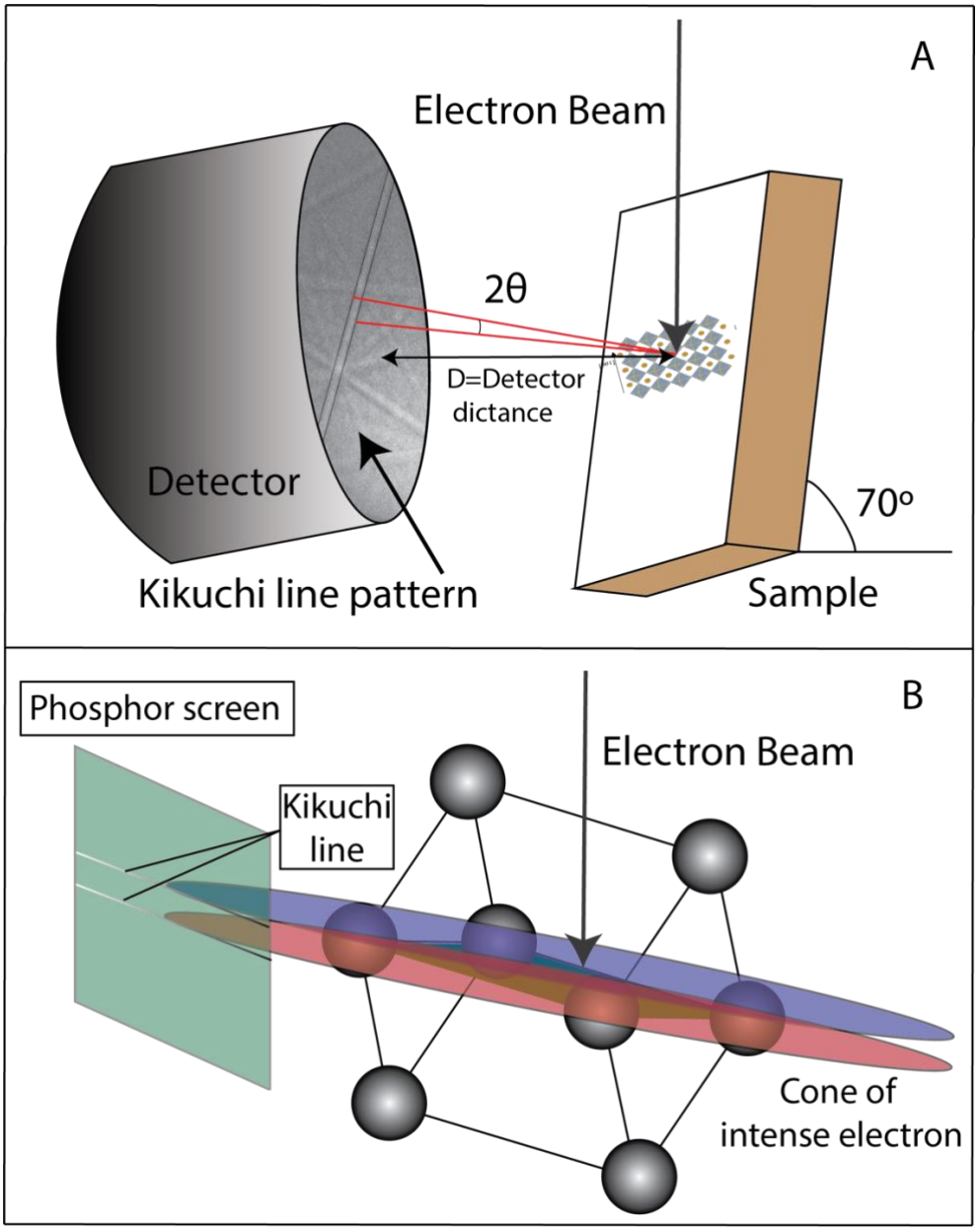

Figure 2.4: A) Schematic of EBSD in the SEM chamber B) Formation of Kikuchi lines on the phosphor screen

2.2 Sample Preparation

2.2.1 Cesium Lead Tribromide ($CsPbBr_3$)

The single-crystalline $CsPbBr_3$ domains we have investigated in our experiments were prepared in a two-step procedure. $CsPbBr_3$ precursor solution was prepared by dissolving $PbBr_2$ and CsBr in a 1:1 molar ratio in dimethyl sulfoxide (DMSO). The quartz substrates were sputter coated with gold using an EmitechK575X Peltier cooled metal coater. A 35mA current and 60-sec sputter coating gave a thin conductive layer of gold (thickness ≈ 10-20 nm), which was also beneficial for the dispersion of precursor solution, resulting in excellent quality crystal growth. 20 μL 0.2M $CsPbBr_3$ precursor solution was drop cast onto gold-coated quartz substrates and annealed at 45 °C for 3 hours in a DMSO-saturated atmosphere. Solvent evaporation resulted in a $CsPbBr_3$ film with crystalline microstructures, as shown in Figure 2.5.[70]

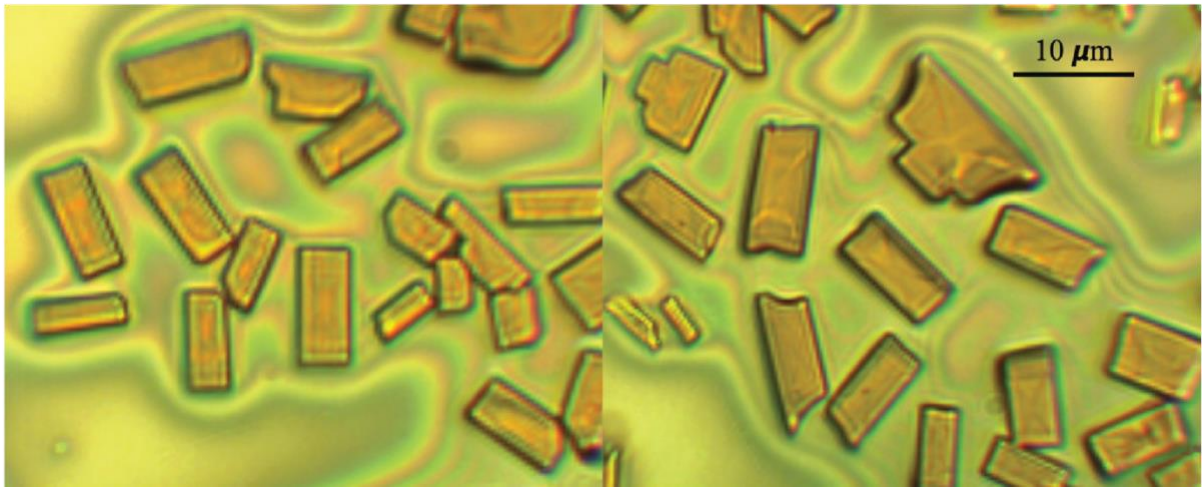

Figure 2.5: Brightfield image of a $CsPbBr_3$ thin film on a gold-coated glass substrate.

2.2.2 PCN-222 Metal-Organic Framework

PCN-222 microrods were prepared by suspending $ZrOCl_2 \cdot 8H_2O$ (151 mg, 0.469 mmol), TCPP(37 mg, 0.0468 mmol), and difluoroacetic acid (DFA) (1.476 mL, 23.45 mmol) in N,N-dimethylformamide (DMF) (14.5 mL) in a scintillation vial and placing the suspension in an oven held at 120°C for 18 hours. The resultant violet powder was centrifuged and washed with DMF and acetone. The obtained microrod powder was dried under vacuum at 60 °C overnight.[71, 72] To prepare samples for microscopy studies, The PCN-222 microrods were dispersed in ethanol, spin-coated onto a glass substrate, and heated at 200°C for 10 minutes to ensure complete solvent evaporation.

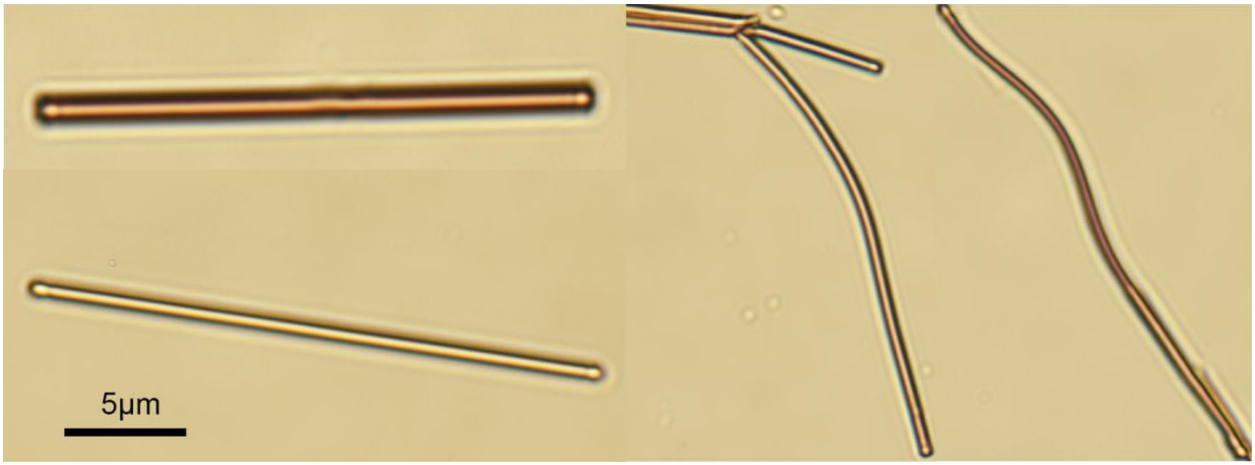

Figure 2.6: Brightfield image of straight and bent PCN-222 microwires.

CHAPTER THREE

IMPACTS OF INTRINSIC LATTICE STRAIN ON THE EXCITED-STATE CARRIER TRANSPORT IN LEAD HALIDE PEROVSKITE MICROCRYSTALS

3.1 Introduction:

Lead halide perovskites (LHP) are a class of direct bandgap semiconductor materials that are widely used in photovoltaic solar cells and light-emitting devices.[6, 73, 74] By changing the chemical composition of the halides, the bandgap of LHP materials can be modified, making them better suited for designing a wide variety of optoelectronic applications.[75-77] Solution processing techniques offer a cost-effective avenue for the production of Lead Halide Perovskite (LHP) materials.[78-80] However, solution processing can introduce structural heterogeneity that impacts the functional properties of the LHP materials.[81] Comprehending the impacts of structural heterogeneity in Lead Halide Perovskite (LHP) materials poses significant experimental challenges. The current photophysical understanding of solution processed LHP materials is primarily derived from bulk measurements[82, 83]. However bulk measurements only illustrate structure-averaged functional properties, which do not provide insight into the role played by microscopic structural defects on the photophysical properties in microscale LHP crystals.[84] Therefore, designing robust microscopic experiments is essential for understanding the intricate structure-function relationship within LHP materials.

Intrinsically, solution processing introduces both plastic and elastic deformations in the lead halide perovskite crystal structure during fabrication.[85] Structural deformations (defects, dislocations, misorientations) can occur due to non-equilibrium processes such as spin coating and solvent evaporation, which can kinetically trap the local crystal structure. Structural heterogeneities may also arise from the mismatch of the coefficient of thermal expansion between the substrate and the perovskite material during crystal growth.[17, 18] Structural deformations can disrupt the periodicity of the crystal structure, leading to lattice strain.[86] This intrinsic strain has the potential to alter the electronic band structure, consequently affecting the mobility of photogenerated carriers.[87] Strain analysis in Si has revealed the influence of lattice strain on photoluminescence and excitonic diffusive motion resulting from potential gradient due to strain distribution.[88] Strain variation has been reported to cause photoluminescence peak position shifts due to strain variation in single heterostructures of GaAs thin films.[89]

Similarly, intrinsic lattice strain has consequences on the electronic band structure in solution-processed perovskite thin films. In lead halide perovskites, the valence band is formed from Pb-s and X-p orbitals that are strongly anti-bonding in character. In contrast, the conduction band is primarily derived from the weakly anti-bonding Pb-p orbitals.[87] When the perovskite film experiences defect-mediated tensile strain, the lattice expands, which weakens the Pb-X bonds. This, in principle, should drop both the anti-bonding valence band and conduction band energy levels. The valence band, with strong anti-bonding hybridization, is significantly decreased, while the conduction band is less affected by the changes in the bandgap lattice strain.[87, 90-92] A schematic of band structure modification due to lattice strain is shown in Figure 3.1. While the formation of microscale regions with variable strain levels suggests that there are corresponding

domains of modulated electronic structure, it is not well understood how these local strain gradients affect excited state dynamics.

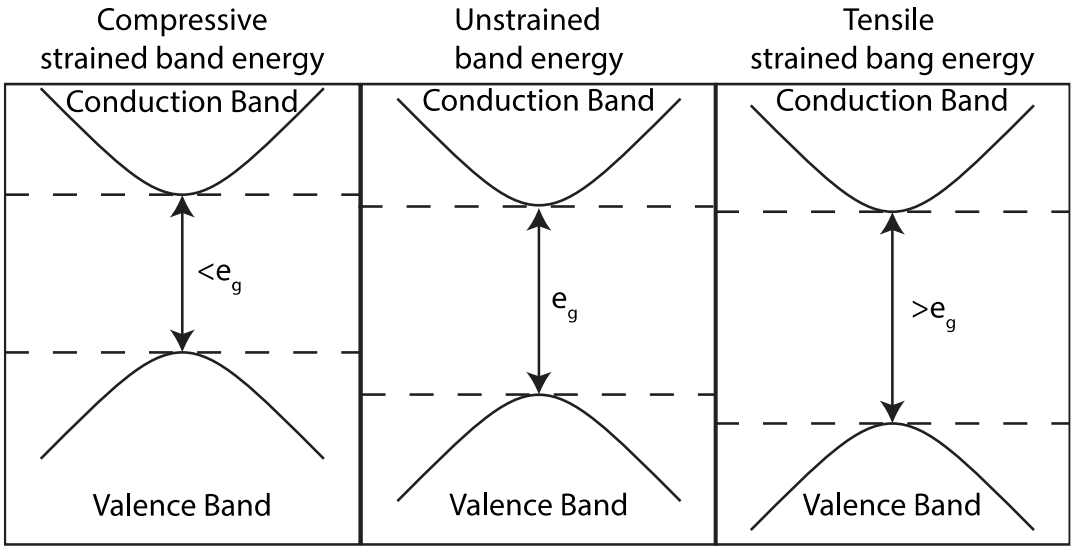

Figure 3.1. Schematic of band structure modification due to lattice strain.

To overcome this knowledge gap, we designed a series of microscopic experiments to elucidate the excited state carrier dynamics and quantify the structural heterogeneity in $CsPbBr_3$ microcrystals. In this study, we utilized time-resolved pump-probe microscopy (PPM) to characterize the excited state carrier transport in microscale single-crystalline $CsPbBr_3$ domains. We directly measured the spatial evolution of the excited state to determine carrier diffusion in lead halide perovskites domains. These results revealed that charge carrier diffusion is anisotropic in nature. We hypothesized that anisotropic diffusive motion occurs due to an inhomogeneous energetic distribution caused by structural or chemical defects in the perovskite network. To quantify lattice strain due to structural heterogeneity, we took two separate approaches. Firstly, we used electron backscatter diffraction (EBSD) microscopy to quantify local lattice strain by analyzing crystallographic changes resulting from structural deformations.

We hypothesized that charge carriers would diffuse faster in tensile strained areas and slower in compressive strained areas. Secondly, we used photoluminescence (PL) microscopy to demonstrate energetic distribution in perovskite microcrystals. We inferred that faster diffusive motion would be observed in the energetically downhill direction, and slower exciton transport would be observed in the energetically uphill direction. These experiments illuminated the importance of microscopic analysis of lattice strain to determine the excited state photophysical behaviors in lead halide perovskite thin films.

3.2 Result and Discussion

The following results were obtained from a single $CsPbBr_3$ domain that was part of a low-coverage thin film deposited on a gold-coated quartz substrate. A scanning electron microscope (SEM) image in Figure 3.2 shows A $CsPbBr_3$ domain, which is about 8 μm x 25 μm in size and representative of most of the film. Figure 3.2 panel B shows the transient reflectivity (ΔR/R) image of the domain shown in Figure 3.2(A) using a home-built pump-probe microscope. Transient reflectivity images were collected by scanning the spatially overlapped pump (400nm) and probe (800nm) beams at a set pump-probe delay time ($\Delta t = 1\ ps$) and measuring the pump-induced change in probe reflectivity. From the transient reflectivity image, 8 locations were chosen on the domain to measure carrier diffusivity. The location of diffusion measurement discussed below is indicated on the pump-probe image in Figure 3.2 panel B (white circle).

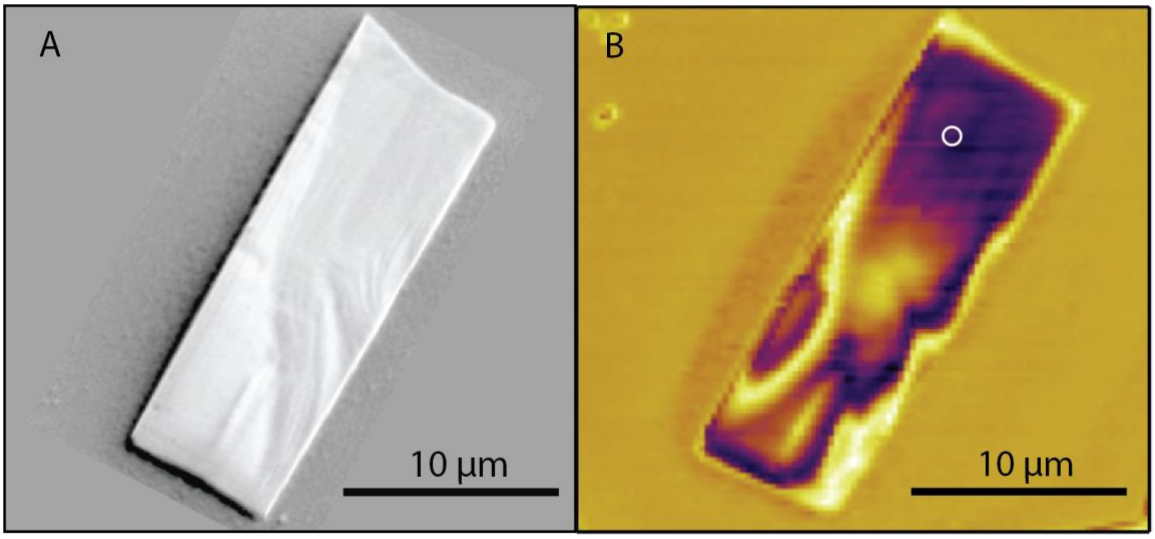

Figure 3.2. (A) SEM image (B) Pump-probe image of the same CsPbBr3 single crystalline domain.

To characterize the transport properties of individual $CsPbBr_3$ perovskite domains, we used spatially separated pump-probe microscopy to directly observe the spatial evolution of the excited state. For diffusion measurements, the probe beam is fixed on a particular location within a $CsPbBr_3$ domain, and the pump beam is scanned spatially over the field of view at various delay times (1ps, 10ps, 30ps, 80ps, 130ps, 200ps). The resulting images show the temporal and spatial evolution of the excited state. Figure 3.3 A illustrates spatially separated images at pump-probe delay times of 1, 80, and 200 ps obtained from the location marked with the white circle on the domain in Figure 3.1 panel B. The profiles (generated by integrating the images along the (0, $\pi/4$, $\pi/2$, $3\pi/4$,2π, π,$5\pi/4$,$3\pi/2$,$7\pi/4$ angles) increase in width due to the diffusive motion of the excited states from a region of high excitation density to the surrounding low-density region. We observe a linear increment of mean square deviation (MSD) of the profiles as a function of delay times. MSD vs. Δt plot along $3\pi/2$ and $\pi/2$ directions are shown in Figure 3.3, panels B and

C, respectively. To extract the diffusion coefficient, angle-resolved time-dependent profiles are fit to a numerical convolution of the experimental point spread function with Green's function solution to the diffusion equation.[93] In Figure 3.3 panel D, we observe that the diffusion coefficient reaches a value of 0.906 cm^2/s in the $3\pi/2$ direction; on the other hand, in the $\pi/2$ direction, diffusion reaches a value of 0.182 cm^2/s. Exciton diffusion is five-fold higher in the $3\pi/2$ direction compared to the $\pi/2$ direction.

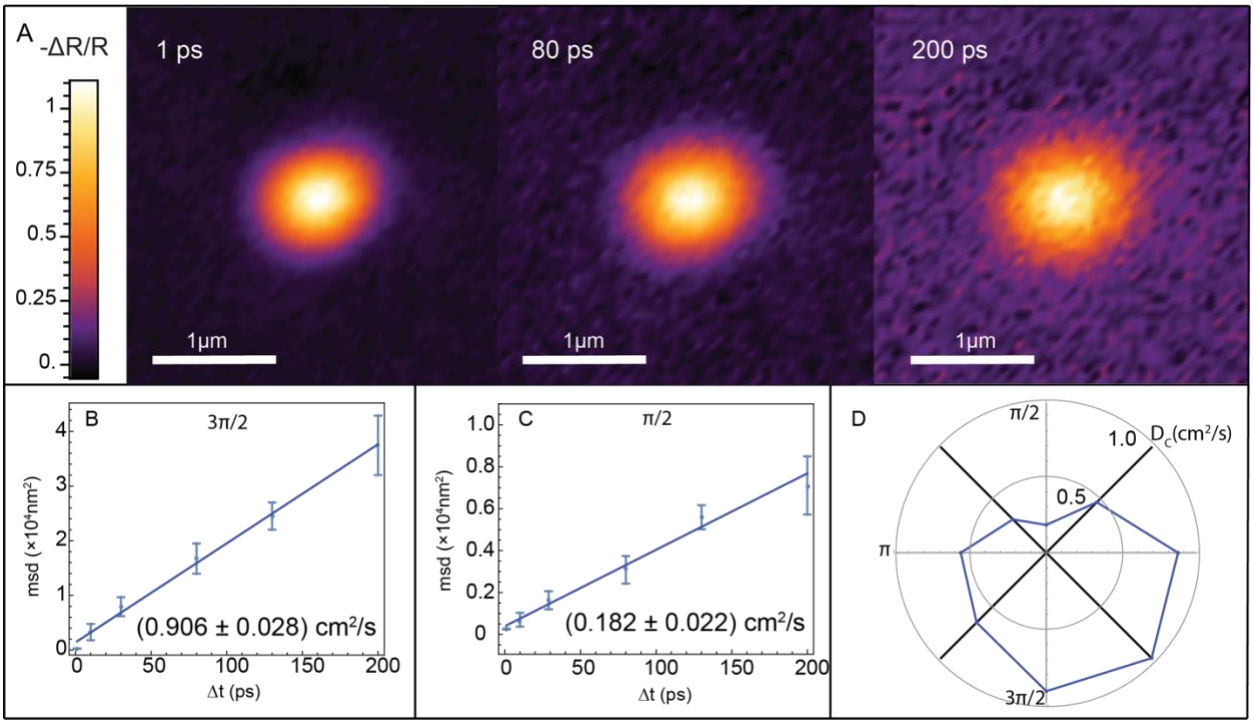

Figure 3.3. Spatially separated pump-probe measurement for determination of diffusion coefficients in $CsPbBr_3$. (A) Spatially separated TR images at Δt = 0, 80, and 200 ps. (B) and (C) The plot of MSD vs. Δt: in the $3\pi/2$ and $\pi/2$ direction, respectively (the slope is proportional to the diffusion constant). (D) The radial plot of the diffusion coefficients showed the slowest diffusion in the $\pi/2$ direction and the fastest in the $3\pi/2$ direction.

The surprising level of anisotropic carrier transport led us to hypothesize that local structural heterogeneity, in the form of lattice strain, impacts carrier transport on the sub-micron length scale. To test this hypothesis, we used EBSD (electron backscatter Diffraction) to conduct spatially resolved crystallographic measurements and investigate structural heterogeneity. Electron backscatter diffraction is a technique that can be used to precisely quantify structural heterogeneity through crystallographic analysis.[94, 95] In this technique, the accelerated electrons in the incident beam are diffracted (following Bragg's law equation 3.1) by the atomic planes in the crystalline domains, creating a distinctive Kikuchi line pattern unique to the crystal orientation.[96]

$$2d_{hkl}\sin\theta = n\lambda \qquad (3.1)$$

Each Kikuchi line in the Kikuchi pattern represents a lattice plane from which the incident electrons are diffracted.[97] A mathematical explanation given below illustrates how the Kikuchi line bandwidth (A_{hkl}) is representative of the modification of interplanar distance (d_{hkl}) due to the local lattice strain. The Kikuchi line width, A_{hkl}, is expressed by Eq 3.2,

$$A_{hkl} = 2\theta D \qquad (3.2)$$

Here, D is the detector distance of the Auger nanoprobe (shown in Chapter 2). As Bragg's angle is very small, sinθ can be replaced with θ, and substituting θ in equation 3.2 gives a direct relation between interplanar distance and Kikuchi line bandwidth (Equation 3.3).

$$d_{hkl} = \frac{\lambda D}{A_{hkl}} \qquad (3.3)$$

Equation 3.4 provides the relationship of lattice constant "a" of a cubic crystal lattice and lattice spacing, d, of the hkl plane.

$$\frac{1}{d_{hkl}^2} = \frac{h^2 + k^2 + l^2}{a^2} \qquad (3.4)$$

The lattice constant "a" for cubic crustal structure is inversely related to the Kikuchi line bandwidth, as described in equation 3.5.[98]

$$a = \frac{\lambda D}{A_{hkl}} \sqrt{h^2 + k^2 + l^2} \qquad (3.5)$$

To quantify local strain in the $CsPbBr_3$ domains shown in Figure 3.2 panel A, Electron Backscatter Diffraction (EBSD) was used to collect 2730 Kikuchi patterns with a spatial resolution of 400 nm. A Mathematica script was developed to analyze each Kikuchi pattern assuming a pseudo-cubic crystal structure to determine relative lattice strain by measuring Kikuchi line bandwidth (A_{hkl}). The procedure is summarized in Figure 3.4. To calculate the Kikuchi line bandwidth, a radon transformation was performed on each Kikuchi pattern image. The radon transform of an image is the line integral of that image along given angles.[99] When the radon transformation is applied to a Kikuchi pattern image, it generates a map with a number of peaks,[100] where each peak represents a distinct Kikuchi line (Figure 3.4B). These peaks are indicative of both the angle and position of the respective lines. The line integral of a Kikuchi line is an intensity profile, and the derivative of this profile is used to measure the line bandwidth precisely. In this domain, we analyzed the line representing the (200) plane (indicated in Figure 3.4 A), and the (200) line peak is shown on the radon transformation map in Figure 3.4 B inset.

The line bandwidth (A_{hkl}) of the (200) line was determined by taking the derivative of the intensity profile of the peak shown in Figure 3.4 panel C. Following the measurement of the (200) plane line bandwidth (A_{hkl}) for each pattern, we obtained a spatial distribution of Kikuchi line bandwidth (A_{hkl}). Subsequently, we calculated the average line bandwidth from the central region of the domain and identified that as the reference line bandwidth $(A_{hkl})_0$. Equation 3.6 shows the strain equation where "a" is the lattice constant (eqn. 3.5) and $a_0 = \frac{\lambda D}{(A_{hkl})_0}\sqrt{h^2 + k^2 + l^2}$ is the reference lattice constant. When the value of "a" and "a_0" is substituted in equation 3.6, the modified strain equation is shown by equation 3.7, which we have used to quantify relative lattice strain.

$$\mathcal{E}\% = \frac{a - a_0}{a_0} \times 100\% \qquad (3.6)$$

$$\mathcal{E}\% = \left(\frac{(A_{hkl})_0}{A_{hkl}} - 1\right) \times 100\% \qquad (3.7)$$

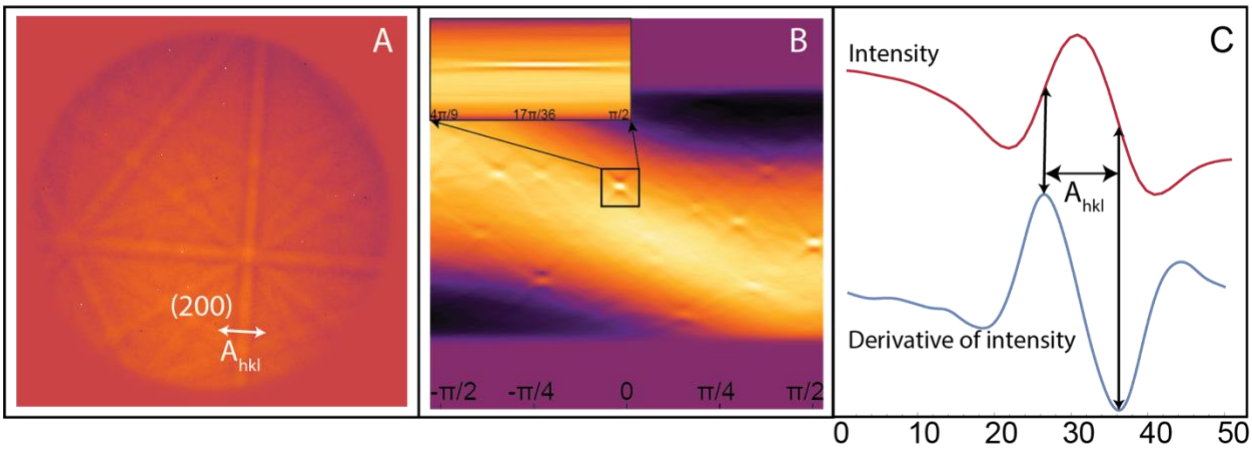

Figure 3.4: A) A Kikuchi line pattern where (200) line is indicated. B) radon transformation of the Kikuchi patterns shown in pane A. C) Bandwidth (A_{hkl}) measurement from the slope of the intensity profile.

Figure 3.4 panel B shows the spatial distribution of relative lattice strain measured using equation 3.7. We observed 10% compressive strain to 10% tensile strain in a single crystalline domain that suggests $CsPbBr_3$ microcrystals exhibit significant lattice strain due to structural deformation. We devised a method employing Mathematica to register the strain image with the pump-probe image, ensuring accurate correspondence between two images of the same domain acquired by the two instruments (Figure 3.5. Panel A and B). Upon registering the images to each other, we pinpointed the locations for diffusion measurements on the strain image and extracted strain values corresponding to the directions of diffusion components. In this way, we correlated the EBSD-determined relative strain value to each directional diffusion coefficient. Figure 3.5C shows the correlative plot of diffusion coefficients vs. lattice strain values. Although we see a variation in the diffusion constant that spans 0.6 – 1.6 cm^2/s along the direction orthogonal to the (200) plane and strain gradient variation between -5 and 1%, no clear

correlation is found along this crystal direction. Similar analyses for the strain along other crystal directions similarly show no clear correlation.

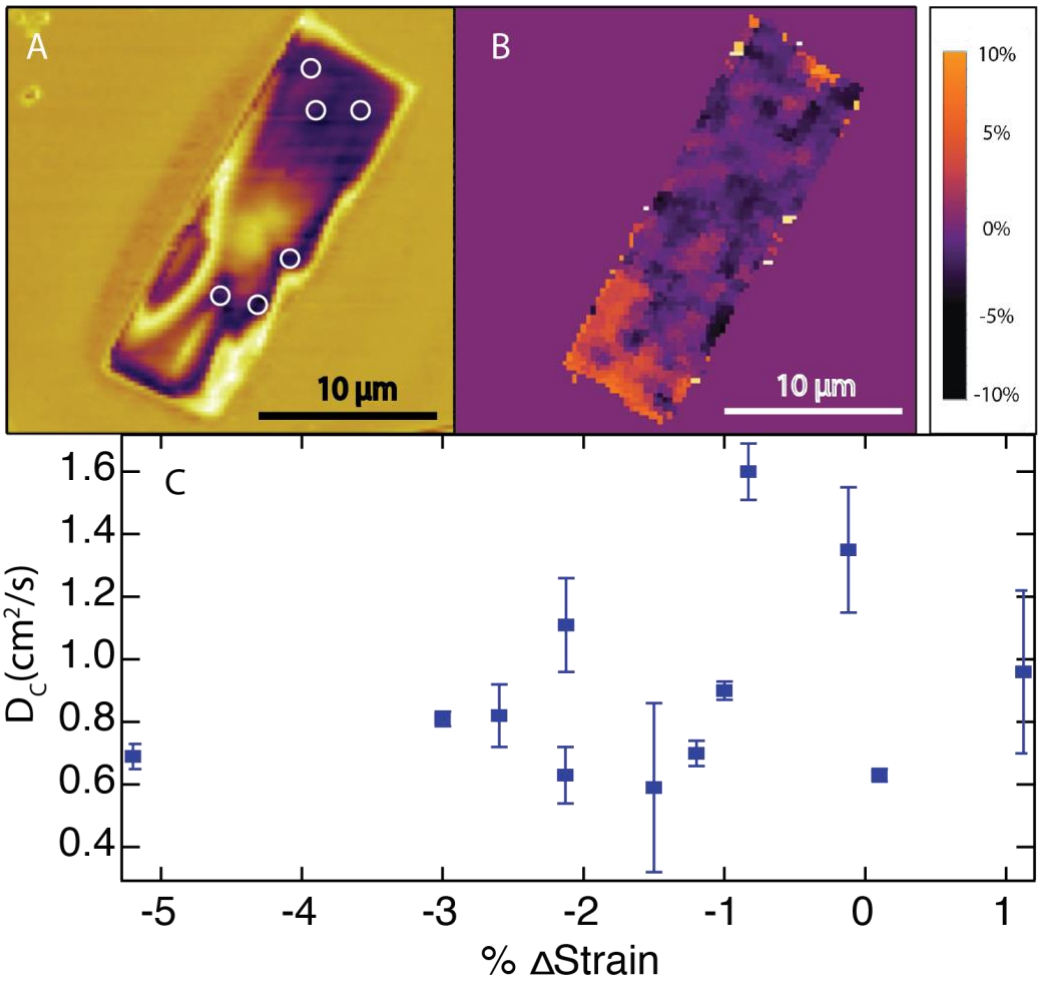

Figure 3.5. A) Pump-probe image of the CsPbBr3 domain B) Spatial distribution of percent strain map matched with the pump-probe image C) Diffusion coefficient vs. gradient of percent strain plot.

Despite a wide range of strain values and measured diffusion coefficients that span 0.6 to 1.6 cm^2/s, the correlative approach described above shows no clear relationship between the two material properties. Correlating anisotropic diffusion coefficients with quantified lattice strain presented significant challenges for several reasons. The primary challenge to making these correlative measurements lies in the computational approach to align images taken from two different instruments. The different spatial resolutions of the two techniques, potential sample drift during the course of the measurement, different image resolutions, and different pixel sizes are some of the concerns that have introduced complexities in perfectly correlating diffusion coefficients with strain. There is also the issue of the fact that diffusion happens over a region, where there may be strain gradients. Then, our analysis involved simplifying the calculation of the percentage of lattice strain by observing changes in the bandwidth of one lattice plane at a time. Yet, overlooking other planes during strain quantification fails to provide a comprehensive understanding of lattice strain. The fact that EBSD can probe only the surface of the microcrystal, whereas the optical signal is generated from the entire depth of the microcrystals, may pose another reason for not observing any correlation between lattice strain and exciton transport. Lastly, the location of pump-probe diffusion measurements was constrained by the local optical response. Consequently, measuring diffusion in regions with high-strain gradients was also highly challenging. Low signal in the regions of high strain gradient could be due to local structural heterogeneity. Correlating transport properties with lattice strain measured through EBSD was challenging for presented reasons and prevented a robust correlation.

Next, we attempted to measure strain using optical techniques. The motivation behind this effort was that it eliminated the uncertainty associated with the difference in spatial resolution and

image registry that we believed to underpin the lack of correlation observed in Figure 3.5. We modified our pump-probe microscope to enable simultaneous observation of transient reflectance signal and steady-state emission upon photoexcitation. The motivation behind this experiment was to directly measure the spatial variation of band energy resulting from modifications in the band structure due to lattice strain. Integrating photoluminescence with pump-probe measurement capabilities in a single instrument can eliminate the challenges of aligning measurements from different instruments. Spatially overlapped scanning of a domain will record a pump-probe signal and a photoluminescence spectrum for each pixel. Consequently, we obtained a pump-probe image and a band energy image (after analyzing each spectrum) of the same domain, perfectly matched to one another.

For analyzing the photoluminescence (PL) spectra, we developed an additional Mathematica script to process each spectrum, enabling us to determine the peak positions in each spectrum using Gaussian fitting. The shifts in spectral peak positions serve as indicators of changes in band energy due to structural heterogeneity. Plotting the peak positions spatially provided us with an energetic distribution within the perovskite domains (Figure 3.6 panel B). Since, the pump-probe image and the photoluminescence image are both on the same spatial coordinates, it this modification fascilitated the direct correlation between exciton transport and changes in band energy. We hypothesize that photo-generated carriers will travel faster towards energetically downhill areas, and transport will be inhibited towards regions of the high bandgap.

To test this hypothesis, we measured diffusion coefficients and steady-state photoluminescence spectra on the same domains. Figure 3.6 Panel A shows a pump-probe image of a $CsPbBr_3$ domain where we collected the PL spectra. The band energy distribution is shown in Figure 3.6, panel B. We imaged the domain in two segments to achieve a higher special resolution for observing the change in band energy. This approach allowed us to quantify the change in bandgap energy and directly correlate it with the transport measurements. We measured diffusion coefficients at 6 locations along four directions ($0,\pi/2, 2\pi, 3\pi/2$) with the previously described method. The energy gradient (ΔE) from the center of the excited state population (where the pump was parked) to 200 nm in each direction was calculated with linear fitting of the energy values in each direction. We predicted to observe slower diffusion towards energetically uphill ($-\Delta E$) directions and faster diffusion toward energetically downhill ($+\Delta E$) directions. The diffusion coefficient vs. ΔE graph shown in Figure 3.4 panel C does not show any clear correlation that lattice strain is the reason behind anisotropic exciton diffusion.

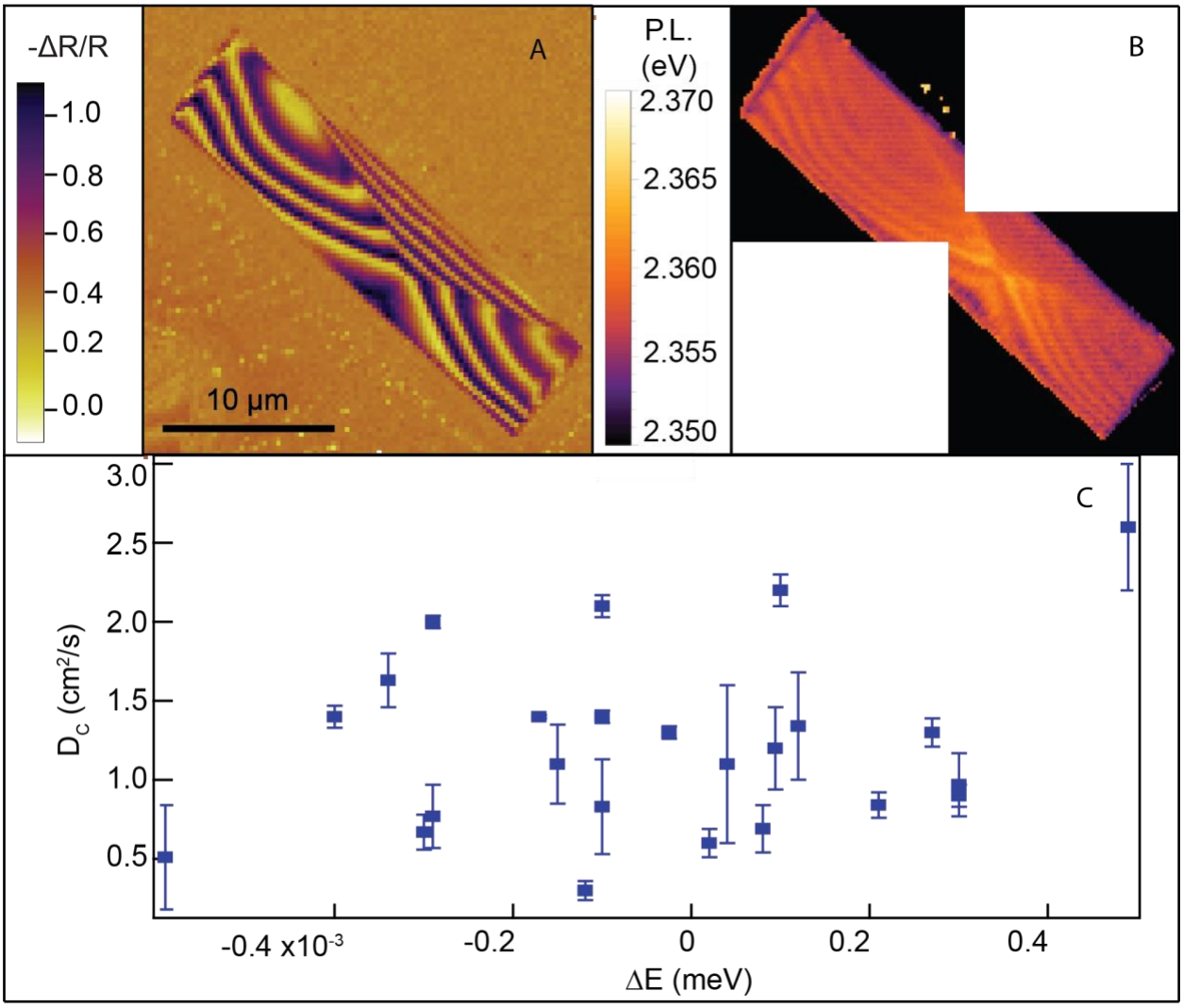

Figure 3.6 A) The pump-probe image of a $CsPbBr_3$ single crystalline domain, and B) The photoluminescence image of the same domain shows the spatial energetic distribution. C) Diffusion coefficient vs ΔE plot.

The absence of correlation encouraged us to revisit our hypothesis carefully. As photoluminescence microscopy is a direct measurement to visualize the band energy distribution, we measured energetic variation of 20meV in the entire microstructure. We observed that changes in band energy within the diffusion length are substantially smaller compared to the room-temperature ΔE value (25 meV) to effectively impact the diffusive motion of exciton. [101]

Surprisingly small energy variation is evident that there was very little structural heterogeneity. However, the mystery of anisotropy in transport measurement is still unresolved. Perhaps diffusion is affected by local point defects that are not accurately measured by PL or strain because EBSD or photoluminescence are not sensitive to local point defects. [70]

3.3 Conclusion

In conclusion, we employed pump-probe microscopy to investigate the exciton transport characteristics of single-crystal $CsPbBr_3$ domains. We analyzed lattice strain and changes in the electronic band structure of microscale structures using electron backscatter diffraction and PL microscopy. However, we could not find any correlation between the anisotropic diffusion coefficients and associated lattice strain. Our results suggest that anisotropic exciton diffusion is likely not due to mesoscopic lattice strain or energy gradient. Correlating diffusion measurements with lattice strain had experimental challenges, yet our results from EBSD and PL microscopy both quantified and illustrated lattice strain distribution in microscale perovskite domains. Although there may not be a strong correlation between structural heterogeneity and excited state dynamics, our results provide valuable insight into the experimental and fundamental limitations that need to be addressed. The fundamental reason for anisotropic exciton transport remains elusive, and designing a more careful investigation is required to determine the correlation between structural heterogeneity and anisotropic exciton diffusion.

CHAPTER FOUR

RAPID EXCITON TRANSPORT AND STRUCTURAL DEFECTS IN INDIVIDUAL PORPHYRINIC METAL ORGANIC FRAMEWORK MICROCRYSTALS

Contribution of Authors and Co-Authors

Manuscript in Chapter 4

Author: Sajia Afrin

Contributions: Characterized all samples. Collected and analyzed all ultrafast microscopy data. Assisted in writing and editing the manuscript.

Author: Xiaozhou Yang

Contributions: Synthesized the sample

Author: Amanda J. Morris

Contributions: Provided valuable feedback on early drafts of the manuscript.

Author: Erik M. Grumstrup

Contributions: Assisted with analysis and editing of the manuscript for final submission.

Manuscript Information

Sajia Afrin , Xiaozhou Yang , Amanda J. Morris, Erik M. Grumstrup

Journal of American Chemical Society

☐ Prepared for submission to a peer-reviewed journal
☐ Officially submitted to a peer-reviewed journal
☐Accepted by a peer-reviewed journal
X Published in a peer-reviewed journal

ACS Publications

Published: February 8, 2024

4.1 Abstract

To date, spectroscopic characterization of porphyrin-based metal organic frameworks (MOFs) has relied almost exclusively on ensemble techniques, which provide only structurally averaged insight into the functional properties of these promising photochemical platforms. This work employs time-resolved pump-probe microscopy to probe ultrafast dynamics in individual PCN-222 MOF single crystals. The simultaneous high spatial and temporal resolution of the technique enables the correlation of spectroscopic observables to both inter- and intra- crystal structural heterogeneity. The pump-probe measurements show that significant differences in excited state lifetime exist between individual PCN-222 crystals of an ensemble. On a single PCN-222 crystal, differences in excited state lifetime and photoluminescence quantum yield are found to correlate to microscale structural defects introduced at crystallization. Pump probe microscopy also enables direct measurement of excited state transport. Imaging of exciton diffusion on individual MOF crystals reveals rapid, but sub-diffusive exciton transport which slows on the 10s of ps timescale. Time-averaged exciton diffusion coefficients over the first 200 ps span a range of 0.27 to 1.0 cm^2/s, indicating that excited states are rapidly transported through the porphyrin network of PCN-222 before being trapped. Together, these single-particle resolved measurements provide important new insight into the role played by structural defects on the photochemical functionality of porphyrin-based MOFs.

4.2 Introduction

Metal-organic frameworks (MOFs), with their characteristic high porosity[48], large specific surface area[49], facile chemical tunability[50], and range of topological structures[52], are the subject of diverse fundamental and practical interest.[44-46] For light harvesting and photochemical applications, the highly-ordered, dense chromophore packing of MOFs can be leveraged to achieve favorable photophysical properties, including large extinction coefficients and efficient energy transfer.[51, 53, 54] Characterization of such properties often leverages steady state and time-resolved photoluminescence (PL) and absorption spectroscopies, techniques that probe a large ensemble of MOF particles.

While the current understanding of MOF excited state dynamics is largely derived from ensemble spectroscopic studies, recent work suggests that single-particle probes might reveal previously hidden links between structure and photophysical function.[102-104] For example, linkers and node site vacancies, which vary between individual particles, are increasingly recognized as important determiners of MOF functionality.[105] Many MOFs also exhibit long-range, extended electronic structure that transcends the "zeroth-order" molecular (ensemble) picture to enable long-range (~50-100 nm) energy transport[53, 54, 63, 106-111] and band-like charge transport.[112-114] The implication of such long range electronic coupling is that inter- and intra-particle differences in electronic structure, caused by local variation in morphology, may strongly influence MOF functional properties.[102-104, 115] Because ensemble probes only provide a structure-averaged observable, they may obscure important variables that are significant determiners of photophysical functionality.

Here we utilize time-resolved pump-probe microscopy (PPM) and PL microscopy to investigate individual PCN-222 (free base) MOF microrods. With its prototypical porphyrin network and large aspect ratio crystals, PCN-222 is an ideal candidate for single particle studies.[54, 116] The microscopy measurements reveal two key insights about excited state evolution in PCN-222. First, by directly measuring spatial evolution of the Q-band photoinduced absorption, we find exceptionally rapid, but sub-diffusive exciton transport through the porphyrin network. The sub-diffusive transport suggests that excitons are rapidly trapped, within the first ~50 ps after photoexcitation, due to structural or chemical defects in the PCN-222 microrods. Second, we find significant spatial variation of excited state relaxation dynamics both within and between individual PCN-222 microrods. Spatial variation in excited state lifetime and photoluminescence quantum yield is extreme in regions where the microrods are bent. These bent regions are believed to result from defects that accumulate during growth, resulting in a reoriented preferential growth direction. While specific to PCN-222, these results highlight the broader importance of crystal defects in determining the photophysical and photochemical behavior of light-active MOFs.

4.3 Result and Discussion

PCN-222 microrods were prepared by suspending $ZrOCl_2 \cdot 8H_2O$, TCPP, and DFA in DMF in a scintillation vial and placing the suspension in an oven held at 120°C for 18 hours. The resultant violet powder was centrifuged and washed with DMF and acetone. The obtained microrod powder was dried under vacuum at 60 °C overnight.[71, 72] To prepare samples for microscopy studies, The PCN-222 microrods were dispersed in ethanol, spin-coated onto a glass substrate, and heated at 200°C for 10 minutes to ensure complete solvent evaporation.

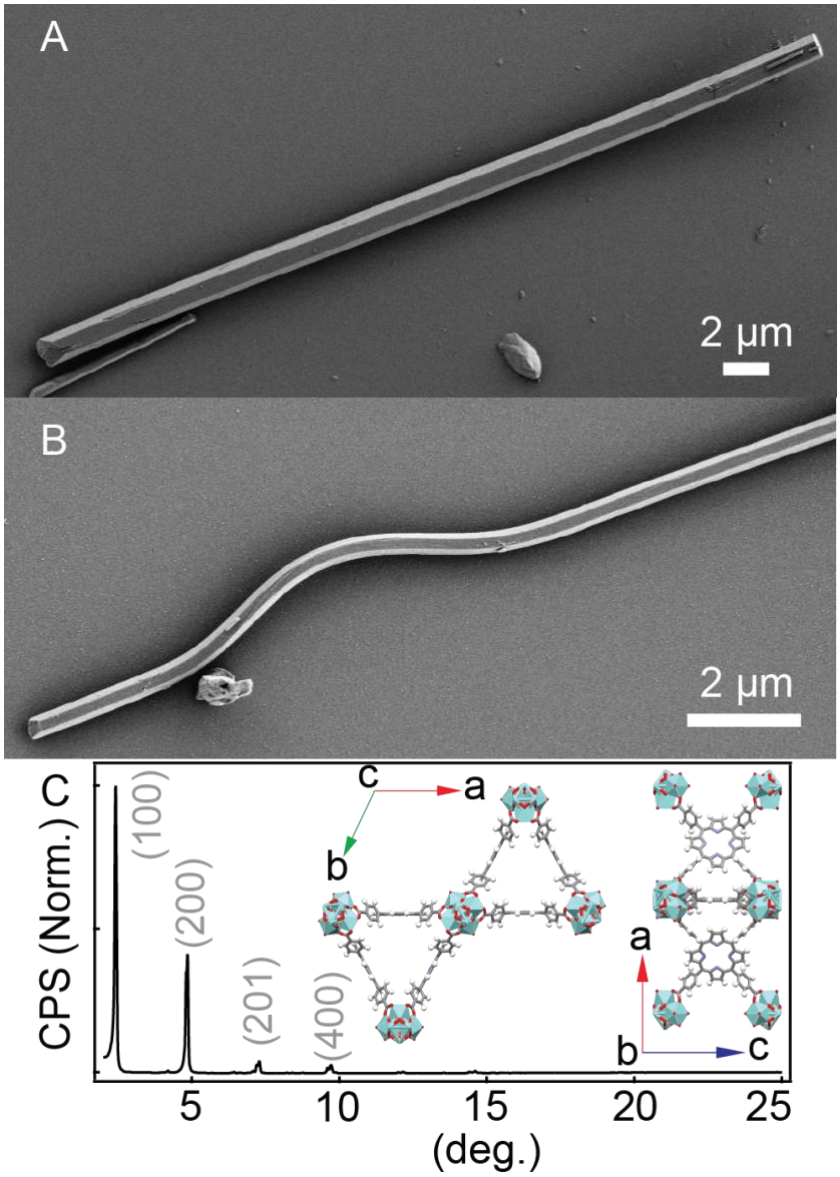

Figure 4.1. PCN-222 microrods. SEM images of a straight (A) and curved (B) rod. (C) Powder XRD pattern and crystal structure viewed along [001] and [010]. Pattern analysis shows a = 41.56 Å and c = 16.1 Å.

Figure 4.1, panels A and B, show representative scanning electron microscopy (SEM) images of straight and curved PCN-222 rods, respectively. The rods are faceted with hexagonal cross sections and, aside from the bend, show few structural defects visible on the surface. A survey of other SEM images (Figure A1) shows that the hexagonal rods can bundle together forming more complex superstructures, and that the curved rods, which tend to be smaller in diameter, constitute approximately 10-20% of the total population. The powder XRD pattern of PCN-222 is shown in Figure 4.1C, along with the crystal structure viewed along the [001] (left) and the [010] (right) direction, respectively.[56, 117] The rods preferentially grow along the c axis, reaching 10 - 40 μm in length.

In Figure 4.2A we show a PPM image of a typical PCN-222 rod, collected on a homebuilt pump-probe microscope (Appendix A).[118] The transient transmission (ΔT) image is collected by scanning spatially overlapped pump (λ: 400 nm, $1/e^2$ width: 680 nm) and probe (800 nm) beams at a pump−probe delay time of $\Delta t = 1$ ps. The negative ΔT signal arises from a combination of Q-band absorption ($S_1 \rightarrow S_n$) and a photoinduced change in reflectivity.[119] For pulse energies up to 400 fJ (41 μJ/cm^2), decay kinetics (Figure. 4.2B) are power independent. At higher pump fluence, although the initial ($\Delta t = 0$ ps) signal size scales linearly with excitation power (Figure 4.2B. inset), nonlinear exciton-exciton annihilation processes begin to influence the decay kinetics. All subsequent data presented are collected with 300 fJ pulse energy to ensure that exciton-exciton interactions are negligible.[120]

That nonlinear decay kinetics are observed for relatively low excitation densities (~1.6×10^{18} cm^{-3}) suggests that excitons are mobile and frequently encounter other excitons, particularly at early times after photoexcitation. To quantify exciton transport, we turned to spatially separated PPM, in which the probe beam is positioned at a fixed location on a rod, and the pump beam is spatially scanned over the probe. Due to the narrow microrod width, we can only measure transport along the long (c) axis. The resultant (1D) profiles (Figure A5 and A6), collected at a series of pump-probe delay times, provide a direct probe of excited state transport in real space. For diffusive transport, the mean square deviation (MSD) of the profile increases linearly with delay time, Δt. As shown in Figures. 4.2C and 4.2D, excitons in the PCN-222 rods generally exhibit sub-diffusive transport, characterized by excitation profile MSDs that increase sub-linearly with time. Typically, such behavior is fit with a power law model, eq. 1.[121, 122]

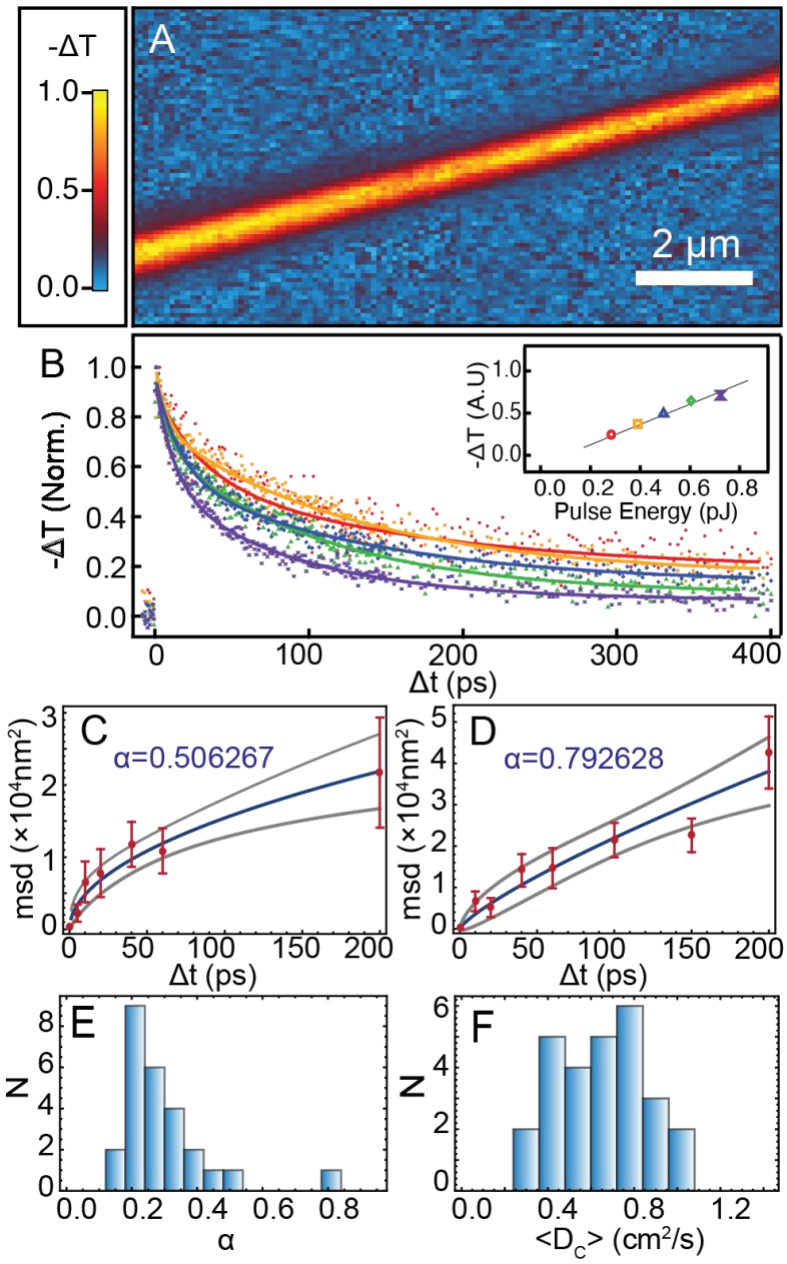

Figure 4.2. Power dependence and diffusion in individual PCN-222 rods. (A) Pump-probe image of a single rod (B) Normalized power dependent decay kinetics. (C) and (D) show representative MSD vs. Δt for two PCN-222 rods. The blue line is a fit to Eq. 1 with 90% confidence intervals in gray. (E) and (F) Histogram showing distribution of α (see Eq. 1) and Δt-averaged diffusion constants.

$$MSD(\Delta t) = A\Delta t^{\alpha} \quad (1)$$

Here A is a proportionality factor, and α is the diffusion exponent. For $\alpha = 1$, Eq. 1 describes diffusive behavior, whereas $\alpha < 1$ is characteristic of sub-diffusive transport. The time-dependent diffusion coefficient is proportional to the first derivative,

$$D_C(t) = \frac{1}{2}\alpha A t^{\alpha-1} \quad (2)$$

Figures. 4.2E and 4.2F respectively show histograms of α and the time-averaged diffusion constant $\langle D_c \rangle$, obtained by integrating Eq. 2 from Δt = 0 ps to 200 ps. 25 individual transport measurements on ten rods yield a mean α of 0.3 and $\langle D_c \rangle$ ranging between 0.27 and 1.0 cm^2/s.

Although direct transport measurements have not been previously reported for PCN-222, it is interesting to note that exciton diffusion constants (measured via PL quenching) for MOFs with comparable, aromatic linkers range between ~10^{-1} – 10^{-2} cm^2/s.[111, 123] The early time transport rates we measure for PCN-222 are larger than in these comparable systems and are larger than that predicted with Forster theory (Appendix A), suggesting that non-thermalized transport[124, 125], superradiance[106], or photon recycling[126, 127] may influence exciton transport in this system. Further single particle studies will be important to understand the impact of these processes on energy transport and their interplay with structural defects.

At delay times greater than ~ 50 ps, transport slows down to rates more consistent with PL quenching measurements. Such sub-diffusive behavior is typically associated with energetic disorder, which causes exciton trapping at low energy sites. As trap sites are increasingly populated after photoexcitation, the population-averaged transport slows. We hypothesized that both sub-diffusive transport (Figures. 4.2C-E) and the overall distribution of $\langle D_c \rangle$ values we observed (Figure. 4.2F) reflect local energetic disorder, presumably a consequence of structural

defects in the extended crystal.[128] To begin to address this hypothesis, we measured excited state decay kinetics for twelve PCN-222 microrods. Three representative datasets are shown in Figure 4.3. In general, we find that the kinetics collected from a single rod (over approximately 6 μm) are highly uniform. For example, each rod shows only a 15 ps variation in average relaxation lifetime (based on a triple exponential fit, see Table A1) measured between the 3 locations. On the other hand, when comparing kinetics between rods, the average decay lifetime of rods (i), (iii), and (ii) are 203 ps, 82 ps, and 61 ps, respectively.

The kinetic similarity observed over a short distance on a single rod, combined with the disparate kinetics observed between rods suggests that variation in defect density, likely in the form of linker or node vacancies, is responsible for the differences in excited state lifetime.[129] No correlation was found between excited-state lifetime and rod diameter (Figure. A4), suggesting that bulk defects, rather than surface states, are responsible for the difference in behavior. Variation in precursor or modulator concentrations, either spatially in the reaction vessel or over the growth period duration, is a likely cause of variable defect concentration.[20, 104]

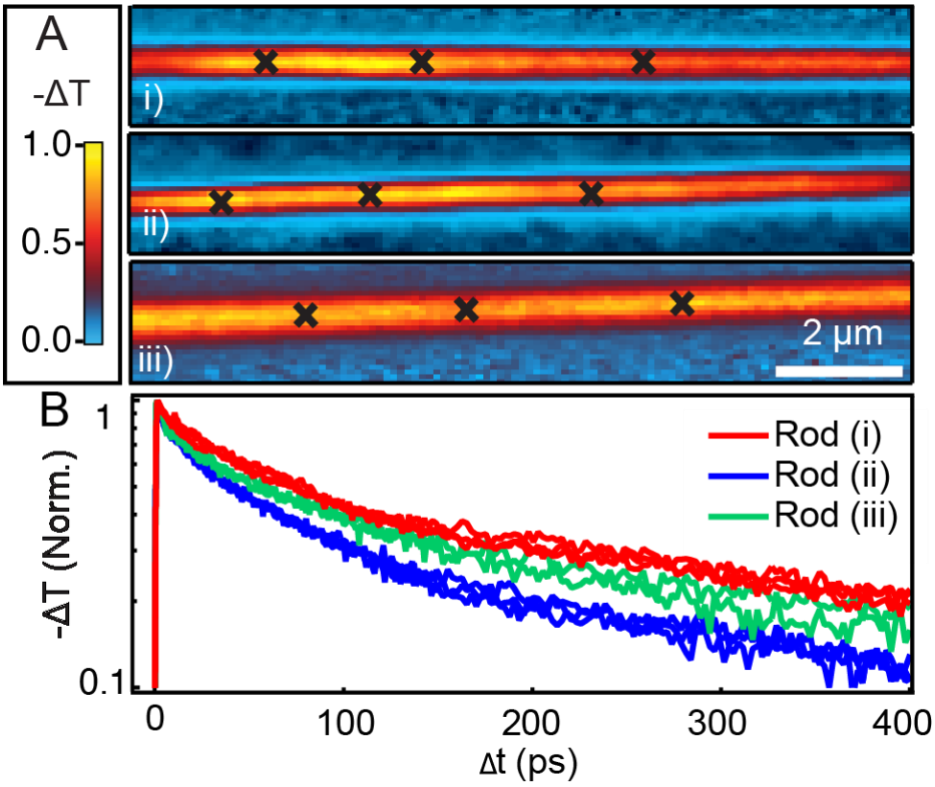

Figure 4.3. (A) Transient transmission images of rods (i), (ii), (iii). (B) Normalized kinetics collected from marked locations in panel (A).

Another indication of the impact of multi-scale structural defects can be observed when comparing the photophysical behavior of straight rods to those of bent rods (Figure 4.1A, B). Deposition of the rods on pre-stretched flexible substrates suggests the rods are brittle (Figure. A9). We, therefore, hypothesized that the observed bends are a direct manifestation of regions with high defect concentration – that is, the growth direction changes because defects accumulate in the crystal structure – and that distinct differences in photophysical behavior should be present in these regions.

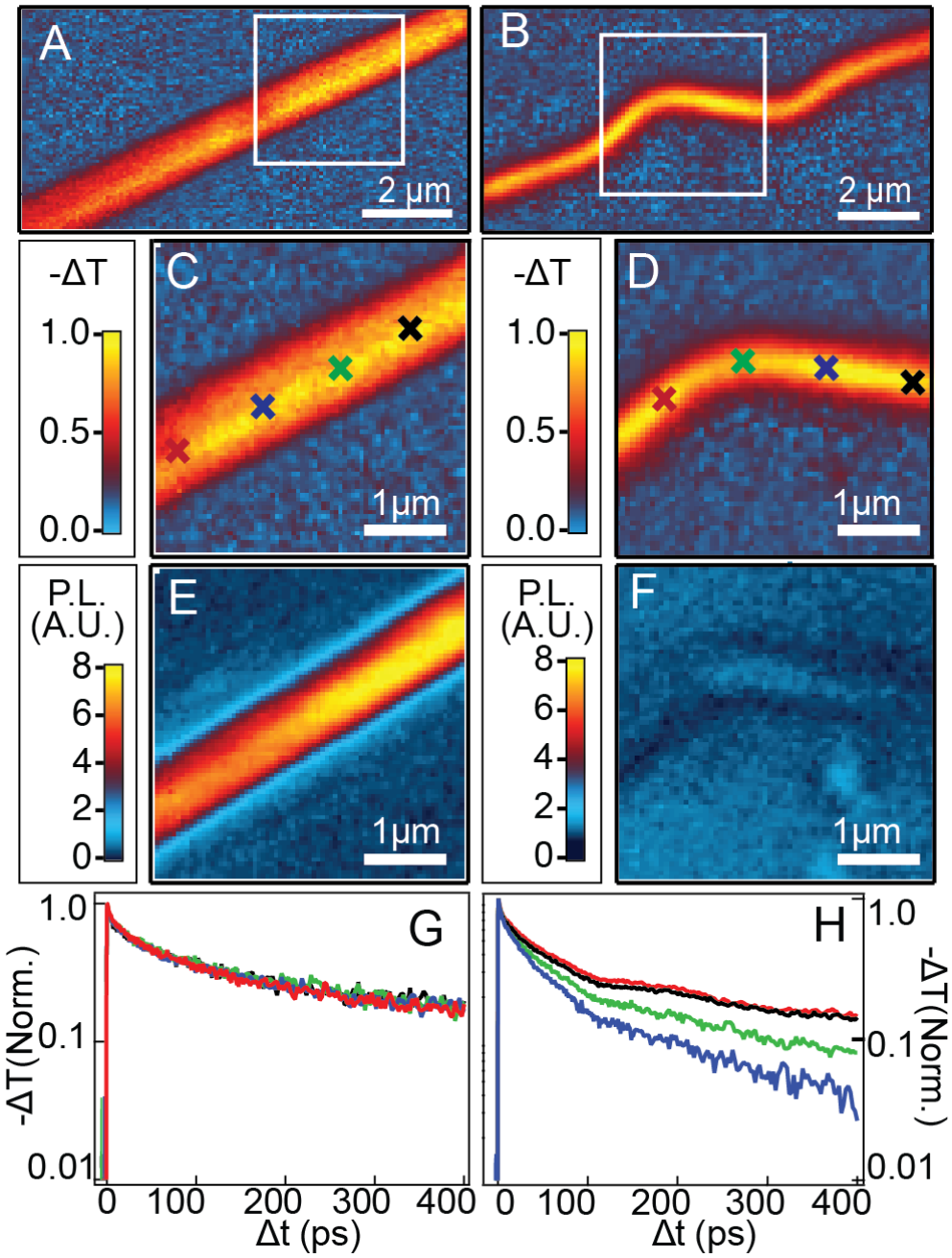

Figure 4.4. Spectroscopic comparison of straight and bent rods. (A) and (B) show transient transmission images of two rods. The boxed region in each is magnified in panels (C) and (D). Panels (E) and (F) show PL images of the straight and bent rods, respectively. (G) and (H) show transient transmission kinetics collected from the locations indicated in panels (C) and (D).

To test this hypothesis, we compared both ΔT kinetics and PL quantum yield of straight and bent rods. Transient transmission images collected at Δt = 1 ps are shown in Figures. 4.4A and 4.4B, with high-resolution images of the boxed region shown in Figures. 4.4C and 4.4D. Although these images are normalized, the ΔT signal magnitude in the bent rod is comparable to that of any other straight rod on the substrate. The primary difference is in the relaxation kinetics: whereas the kinetics collected on the straight rod (Figure. 4.4G) are consistent with previous results (Figure. 4.3C), the curved rod kinetics (Figure. 4.4H) decay faster and exhibit significant variation of ~150 ps in average lifetime. We also collected steady-state photoluminescence images of the same region of each rod. The spectrally integrated PL images are shown in Figures. 4.4E and 4.4F, and while PL from the straight rod is clearly visible, PL from the bent rod is strongly quenched and difficult to distinguish from the background.

Without additional microscopic insight into both defect identity and their effect on the local and long-range electronic structure, it is difficult to know the precise origin of the difference in photophysical behavior. Nevertheless, the collection of results above suggests several important conclusions. First, it appears that exciton transport is exceptionally rapid in PCN-222, at least in the first 10-100 ps after photoexcitation. Second, the presence of defects shortens both the excited state lifetime and the diffusion length. The nearly complete PL quenching in bent regions, where we expect defect density to be disproportionately high, suggests that defects facilitate non-radiative relaxation, perhaps in the form of a charge-transfer state or other low-energy trap with strong vibronic coupling to the ground state. Finally, because energy transport is efficient, defects are likely to have long-range impact on excited state

dynamics, posing important challenges to light harvesting and other electronic and optoelectronic applications.

4.4 Conclusion

In conclusion, we have employed pump-probe and PL microscopy to investigate the excited state dynamics of single-crystal PCN-222 microrods. The micron-scale spectroscopic probes reveal exceptionally rapid exciton transport and important new insight into the effects of structural heterogeneity on excited state dynamics. These results highlight the importance of local spectroscopic probes to elucidate structure-function properties in MOF systems.

CHAPTER FIVE

ENERGETICALLY DEPENDENT TRANSPORT AND RELAXATION DYNAMICS WITHIN A SINGLE POPHYRINIC METAL-ORGANIC FRAMEWORK MICROCRYSTAL

Contribution of Authors and Co-Authors

Manuscript in Chapter 4

Author: Sajia Afrin

Contributions: Characterized all samples. Collected and analyzed all ultrafast microscopy data. Assisted in writing and editing the manuscript.

Author: Skyler Hollinbeck

Contributions: Characterized all samples. Collected and analyzed all ultrafast microscopy data. Assisted in writing and editing the manuscript.

Author: Amanda J. Morris
Contributions: Provided valuable feedback on early drafts of the manuscript.

Author: Erik M. Grumstrup
Contributions: Assisted with analysis and editing of the manuscript for final submission.

Manuscript Information

Sajia Afrin, Skyler Hollinbeck, Amanda J. Morris, Erik M. Grumstrup

X Prepared for submission to a peer-reviewed journal
☐ Officially submitted to a peer-reviewed journal
☐Accepted by a peer-reviewed journal
☐Published in a peer-reviewed journal

5.1 Abstract

Spectroscopic characterization of porphyrinic metal-organic frameworks has primarily been performed through ensemble measurements in the suspended phase. These measurements only reveal structurally averaged functional properties. In this work, broadband and two-color time-resolved pump-probe microscopy measurements are presented to elucidate the ultrafast dynamics within individual PCN-222 MOF single crystals. The simultaneous high spatial, temporal, and spectral resolution of these techniques facilitates the observations of time-resolved spectroscopic evolution within single microcrystals. The transient broadband spectra from PCN-222 microrods exhibit ground-state bleach of the Q bands, stimulated emission peaks and transient absorption features, and their relaxation dynamics. A significant red shift in the broadband spectra was observed in the bent regions relative to the straight regions in the microrods, which was attributed to microscale structural defects introduced during crystallization. Two-color pump-probe microscopy enables direct measurement of excited state transport and the imaging of exciton diffusion with the Soret band and Q band excitation on the same MOF crystal. The results show that Soret band excitation causes rapid but sub-diffusive exciton transport where hot carriers are rapidly transported through the porphyrin network of PCN-222 before becoming trapped. In contrast, Q band excitation yields no evidence of exciton transport, and excited states do not travel far through the porphyrin network of PCN-222. Collectively, these measurements offer valuable new perspectives on light harvesting MOF system functionality by defining the influence of excitation energy and structural heterogeneity on the excited state characteristics and dynamics within a single structure.

5.2 Introduction

Metal-organic frameworks (MOFs) comprise a category of molecular assemblies where organic linkers connect metal clusters, forming an ordered porous network of chromophores.[47] This structural arrangement in MOFs is the foundation of their strong potential in light harvesting and photochemical applications, achieving advantageous photophysical properties, such as high extinction coefficients and efficient energy transfer, with highly organized and densely packed chromophores.[51, 53, 54] Zr-TCPP-based MOFs have gained enormous attention due to their exceptional chemical stability even under harsh experimental conditions and their diverse range of functionalities, including catalysis, light harvesting, gas storage, and sensing.[55-58]

While the existing comprehension of excited state dynamics in MOFs is mainly derived from ensemble spectroscopic studies, recent research suggests that employing single-structure probes can reveal undiscovered relations between the structure and photophysical function within MOF crystals.[54, 72, 130] Ensemble measurements have only provided structure-averaged spectroscopic observables, which conceal the impact of structural heterogeneity in determining photophysical properties in MOF microstructures. A recent study investigated the transport properties and relaxation dynamics of individual porphyrinic MOF microstructures and reported rapid sub-diffusive exciton transport and significant lifetime variation correlated with structural heterogeneity.[131] However, the experimentally measured values of the time-averaged diffusion coefficient were a factor of 20 larger than those predicted by Forester theory. To achieve a comprehensive understanding of the excited state dynamics in porphyrinic MOF microstructures, broadband transient absorption microscopy can be a substantial tool. With broadband transient

absorption microscopy, the time-resolved spectral and spatial evolution of the Q bands can be observed to explain the exciton transport more clearly.

We have employed broadband transient absorption microscopy to study the spectral intricacies of individual microrods in the PCN-222 MOF. PCN-222 (or MOF-545), based on Tetrakis (4-carboxyphenyl)-porphyrin (H_2TCPP) is a highly stable mesoporous zirconium−porphyrin MOF where the H_2TCPP ligand in PCN-222 functions as a visible-light-harvesting unit.[56, 59]The spectroscopic measurements unveil some crucial understanding regarding the excited state dynamics in this porphyrin-based MOF. Initially, we directly measure the transient absorption spectra of an individual structure that aligns with the steady-state spectra of the H_2TCPP ligand monomer. The transient absorption spectrum relaxes without significant transformation biexponentially with a long lived offset. Secondly, we observe significant spatial variations in transient spectral peak positions within each PCN-222 microrod. The spatial shift in spectra is particularly pronounced in regions where the microrods exhibit bending. It is hypothesized that these bent regions result from defects that accumulate during growth, leading to a reoriented preferential growth direction. Previous work exciting with 400nm light, has correlated variation in relaxation dynamics with structural heterogeneity.[130] However, we observe spatially homogenous relaxation dynamics within a microstructure when pumping with 517nm light. Finally, to understand this phenomenon we compare excited state relaxation and transport arising from 400nm and 520nm excitation within a single domain. The results show that the nature of excited state transport and the relaxation dynamics in PCN-222 microrods depend strongly on excitation energy and reveal valuable insight for the future design of PCN-222 based light harvesting systems.

5.3 Synthesis PCN-222

PCN-222 microrods were synthesized by suspending of $ZrOCl_2 \cdot 8H_2O$, TCPP, and DFA in DMF within a scintillation vial. The suspension was placed in an oven set at 120°C for 18 hours. The resulting violet powder underwent centrifugation and was then washed with DMF and acetone. Subsequently, the microrod powder was dried under vacuum at 60°C overnight.[71, 72] For microscopy sample preparation, PCN-222 microrods were dispersed in ethanol, spin-coated onto a glass substrate, and heated at 200°C for 10 minutes on a hot plate to ensure complete solvent evaporation. Then the annealed PCN-222 thin film was encapsulated with a styrene ethylene butylene styrene (SEBS) bead coating to prevent sample from photodegradation.

5.4 Result and Discussion

Figure 5.1, panel A, shows a representative scanning electron microscopy (SEM) image of a straight PCN-222 microrod. The rods are faceted with hexagonal cross-sections and show few structural defects visible on the surface. The hexagonal microstructures can have bent structures or can bundle to form complex superstructures. In Figure 5.1 panel B, we show a PPM image of a typical PCN-222 rod collected on a homebuilt transient broadband pump-probe microscope. The transient transmission ($\Delta T/T$) image is collected by scanning overlapped pump (λ = 517 nm) and probe (626 nm) beams with a spatial convolution of ~1μm at a pump−probe delay time of Δt = 1 ps. The negative $\Delta T/T$ signal arises from a combination of Q-band photo-induced absorption ($S_1 \rightarrow S_n$).[132] Figure 5.1C illustrates the normalized absorption spectra of solid-state PCN-222 microstructures (red trace) and H_2TCPP suspended in THF (blue trace).

Normalized emission spectra of solid state PCN-222 (red trace) and H_2TCPP suspended in THF (blue trace) are shown in Figure 5.1D.

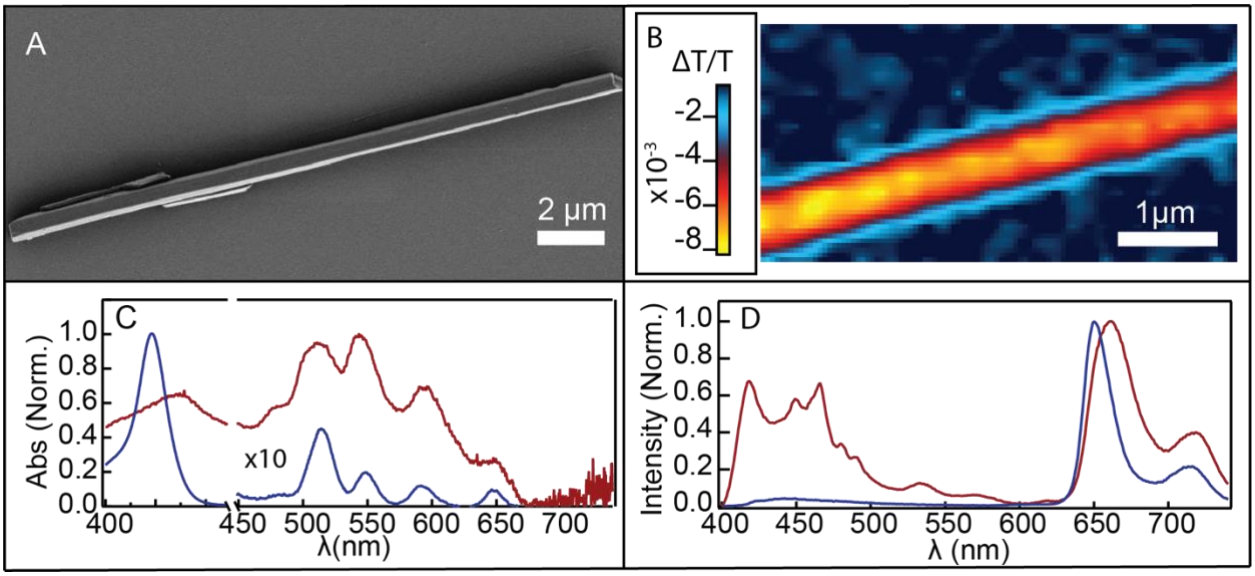

Figure 5.1. PCN-222 microrod. (A) SEM image of a straight rod. (C) Transient transmission image of a single rod (B) Normalized absorption spectra of PCN-222 (red trace) and H_2TCPP (blue trace) (D) Normalized emission spectra of PCN-222 (red trace) and H_2TCPP (blue trace).

The spectroscopic character of PCN-222 in the visible is defined by the organic ligand TCPP, and the absorption bands of TCPP, shown in blue in Figure 5.1C, arise from π-π* electronic transitions on the porphyrin macrocycle.[61, 133] The solid-state PCN-222 absorptance shown in red(Figure. 5.1C) highlights some important differences from the suspended TCPP monomer, but first a discussion of the theory behind TCPP photophysics is warranted. The lower energy absorption peaks (450nm-660nm) are called Q-band transitions (HOMO(HOMO-1)→LUMO) and are split by vibronic coupling and macrocycle protonation in free base porphyrin. The higher energy transition at 418nm (HOMO→LUMO+1) is termed the Soret (or B) band. The relative intensity of these absorption bands is strongly affected by molecular

symmetry and dipole moment interactions, where the two transition dipole moments that give rise to the Q-band transitions exhibit alternancy symmetry. The two dipole moments of opposite sign mix, leading to the cancellation of their intensities.[133] The two analogous transitions for the Soret-band have synchronous symmetry and reinforce each other leading to a strong transition dipole moment.[133, 134] Because the Q-band transitions are pseudo-forbidden the absorption is weak relative to the Soret-band absorbance (Figure 5.1C). The assembly of TCPP into the MOF PCN-222 shifts the observed Soret-band absorption by 83meV, however the Q-band absorptions do not significantly shift in energy but gain significant intensity relative to the soret-band[64]. In PCN-222 microrods, Q-band and Soret-band absorption are on the same order of magnitude indicating incorporation of the ligand into the framework may relax the parity constraints (Fig 5.1 Panel C). We believe the spectroscopic changes of TCPP that occur from monomer to PCN-222 are a consequence of electronic coupling between the chromophore linkers particularly affecting Soret-band excitation. The stronger energetic effect shown by the Soret-band can be interpreted through the lens dipole-dipole coupling where coupling energy is proportional to product of the interacting dipole moments.[135] A theoretical analysis of porphyrin aggregation presented by Zimmerman et. al in 2003 supports the hypothesis that the spectral effects we have observed in PCN-222 likely arise from excitonic coupling between TCPP linkers.[134] Similarly enhanced absorption of the Q-bands has been reported in aggregated free base porphyrin and in covalent organic frameworks(COF) with enforced J-aggregate conformations. [136, 137] In the J-aggregate COF molecular coupling led to lengthened excited state lifetimes as well as facilitation of excited state delocalization.[136] The changes in ground state absorption between TCPP

monomers to PCN-222 evidence coupling between TCPP linkers, and inform how the structural properties of the framework affects the electronic properties of the material.

Another important difference between the TCPP monomer in isolation and PCN-222 is found in the steady state fluorescence profile (Figure. 5.1D). In TCPP, 400nm excitation into the Soret-band is followed by rapid, femtosecond time scale, relaxation to the Q-bands where vibrational cooling and fluorescence occurs.[60, 61] Thus, very little emission is observed from the Soret-band or any other band but the $Q_{x(0,0)}$ and $Q_{x(0,1)}$ transitions shown by the blue spectrum in Figure 5.1D. On the other hand, solid-state PCN-222 (red spectrum in Figure. 5.1D) shows considerable emission intensity from the Soret-band and subtle emission from higher vibrational energy Q-band transitions. The reason for the enhancement of Soret-band emission is not fully elucidated, but the lifetime of these emissive states is investigated further below, and the presence of substantial emission intensity suggests that the Soret-band in PCN-222 is longer lived.

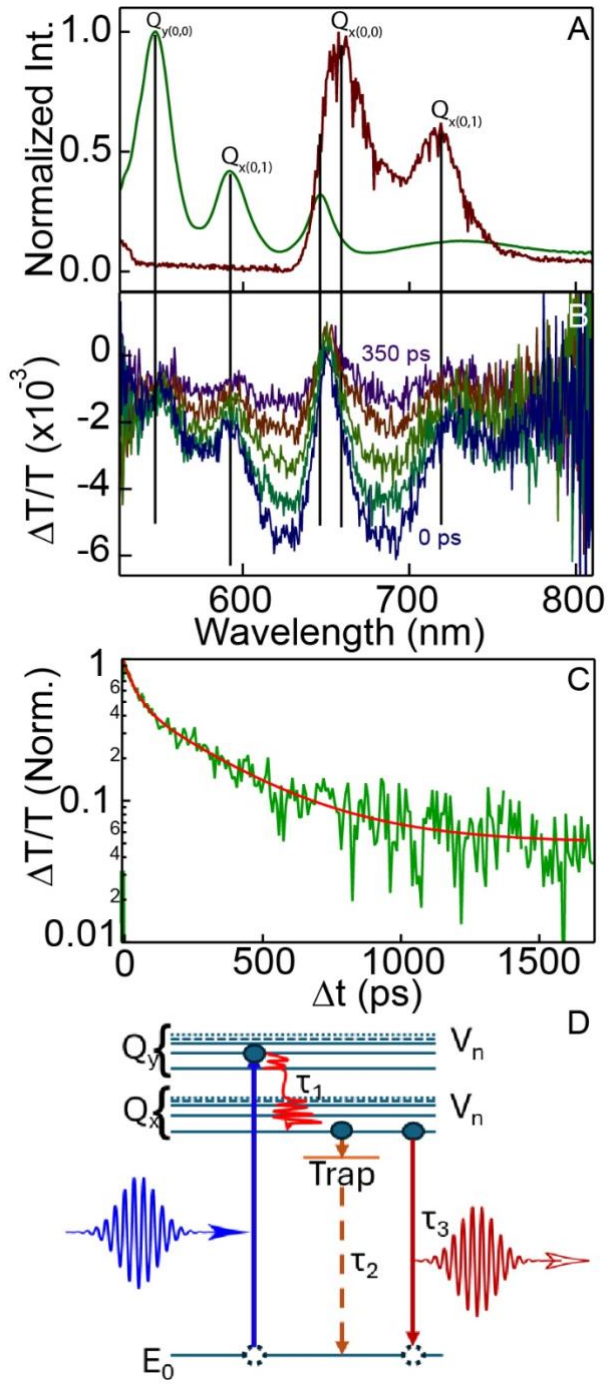

Figure 5.2: PCN-222 Spectroscopic and dynamic characterization. A) Normalized steady state absorbance(green) and emission(red) of single PCN-222 microstructure. Lines are drawn highlighting the alignment of the main spectral features in the steady state spectra and features in pump-probe spectra (Panel B). Time resolved spectra shows the temporal progression of 1, 11.3, 21.6, 46.7, 83.4, 145.5, 248.6, and 351.6ps. C) Kinetic trace of normalized PIA signal at 526nm

with biexponential decay fit (τ_1=41.245±3.56ps, τ_2=306.81±21.2ps). D) Energy level diagram lifetime assignments of relaxation dynamics.

We next turn to transient transmission microscopy to investigate how the electronic coupling of the TCPP liners, shown in ground state spectra, affects the evolution of photogenerated excited state species. To establish a microscopic steady state baseline, we first measure the extinction of an individual straight microrod by comparing the transmission of our white light continuum (WLC) probe through the glass substrate and through the sampled domain, as well as the spontaneous emission arising from excitation of the domain with our 517nm pump. The spectral window of our WLC encompasses the $Q_{y(0,0)}$, $Q_{x(0,1)}$, $Q_{x(0,0)}$ absorption and the Q_x emission bands that are also shown in the steady state spectra (Figure 5.2 panel A).[60] Figure 5.2 Panel B shows the temporal progression of transient transmission ($\Delta T/T$) after photoexcitation of the 517nm pump. The positive-shaped spectral features are overlayed with a broad photoinduced absorption (PIA), resulting in a net negative signal. The positive shaped peaks can be assigned to ground state bleach (GSB) of $Q_{y(0,0)}$ and $Q_{x(0,1)}$, as they align with the steady state features. The peak positions do not appear to shift over the 350ps time frame examined. The positive shaped peak at 651nm is red of the $Q_{x(0,0)}$ absorption feature by 7nm. We attribute this peak position to a convolution of the GSB and the Stokes shifted $Q_{x(0,0)}$ stimulated emission (SE). The $Q_{x(0,1)}$ SE peak is also visible near 725nm. The transient transmission spectra show features that relax without any noticeable shift in peak position, indicating that the nature of the observable excited state in the spectral window does not evolve after photoexcitation. However, the positions of the Q band features vary between different microrods, revealing the presence of structural heterogeneity within different structures.

A normalized kinetic trace of PIA relaxation for solid-state PCN-222 at 626nm is shown in Figure 5.2C. Biexponential fitting yielded decay lifetimes of 41ps and 307ps with an unresolved long-lived component approximated with an offset accounting for roughly 10 percent of the excited population. Several different relaxation mechanisms have been reported for porphyrin-based MOFs suspended in various solvents, with the first and second lifetimes attributed to solvent-induced vibrational reorganization and vibrational cooling respectively[64] as well as shallow trap states[138], and the longest lifetime to fluorescence[137] and deep trap states[138]. We have assigned the shortest lifetime to vibrational cooling of the excited state from the photoexcited $Q_{y(1)}$ to the $Q_{x(0)}$ state affecting Frank-Condon overlap between the excited state and higher lying states and decreasing PIA intensity. We assign the long live-lived population to a stable radiative state that relaxes to the ground state without further transformation. The ~10 percent quantum yield of TCPP[64] and the ~10 percent long-lived signal in pump-probe measurements led to the investigation of this excited state population with Time Correlated Single Photon Counting (TCSPC). TCSPC yielded single exponential decay kinetics from Q_x emission at 652nm with a lifetime of 832ps (Figure 5.6).[130] Fits of kinetic taken in different location and on different microrods yield variation in lifetimes, but despite limitations in signal to noise imposed by sample photosensitivity and instrument limitations reveal a trend. Figure 2D summarizes our hypotheses that photoexcitation into the Q_{y1} state results in an excited state that relaxes vibrationally to the Q_{x0} state in tens of picoseconds followed by trap mediated relaxation with lifetimes that range from 100 to 300ps. The remaining excited state species then relax radiatively with a lifetime of ~800ps. The contradictory reported assignments of relaxation

mechanisms in PCN-222[137, 138] and the subtle variability in early relaxation dynamics necessitate investigation with alternative techniques.

Broadband transient spectra exhibited distinct spectral shifts in Q band ground-state bleach (GSB) and stimulated emission (SE) features across various microstructures. A plausible explanation for the spectral shift is attributed to microscale structural heterogeneity in PCN-222 rods. Two-color pump-probe study on PCN-222 bend rods indicated that bends are correlated to higher defect density.[131] To investigate the correlation between the spectral shift and local microscale structural heterogeneity, we obtained hyperspectral transient transmission images of bent single crystals. Figure 5.3 Panel A illustrates a transient transmission image of a bent domain captured at $\Delta t = 1$ ps (probed at 626nm). Every pixel within the transient transmission image captures a broadband spectrum, illustrating how local microscale structural heterogeneity manifests via spatial variations in the spectral shift. To quantify the spectral shift in a single structure, each spectrum has been analyzed through background subtraction and a Gaussian fitting function to identify the SE ($Q_{x(0,0)}$) peak position precisely. Upon plotting the SE ($Q_{x(0,0)}$) peak positions, we observe an energetic distribution that illustrates a redshift (up to 19 nm) as the microstructure deviates from its straight to a bent trajectory (Figure 5.3B). The transient spectra 1, 2, and 3 in Figure 5.3 Panel C illustrate the apparent spectral shifts. The locations where transient spectra were collected along the length of the wire are indicated in Figure 5.3, panel A, with white circles. The spectral red shift in the bent regions where we expect structural defects to be higher suggests that defects facilitate the change in peak position, perhaps due to peak broadening and low energy trap states. The presence of structural heterogeneity in a bent rod will supposedly impact the relaxation dynamics of the transient spectra. Our hypothesis was that the

excited state would relax faster because of the low-energy trap states. Therefore, Spectra 3 (blue trace Figure 5.3 Panel C) was expected to show the fastest relaxation lifetime, while Spectra 4 (red trace Figure 5.3 Panel C) would exhibit a longer relaxation lifetime. The average relaxation lifetime does not show any trend to support our hypothesis. The kinetic traces (shown in Figure B1) collected along the length of the rod exhibit very subtle variation in the averaged relaxation lifetime (fitting parameters are shown in Table B1). Even though we observe a distinct red shift due to local defect sites, the impact of local structural heterogeneity on the relaxation dynamics remains elusive.

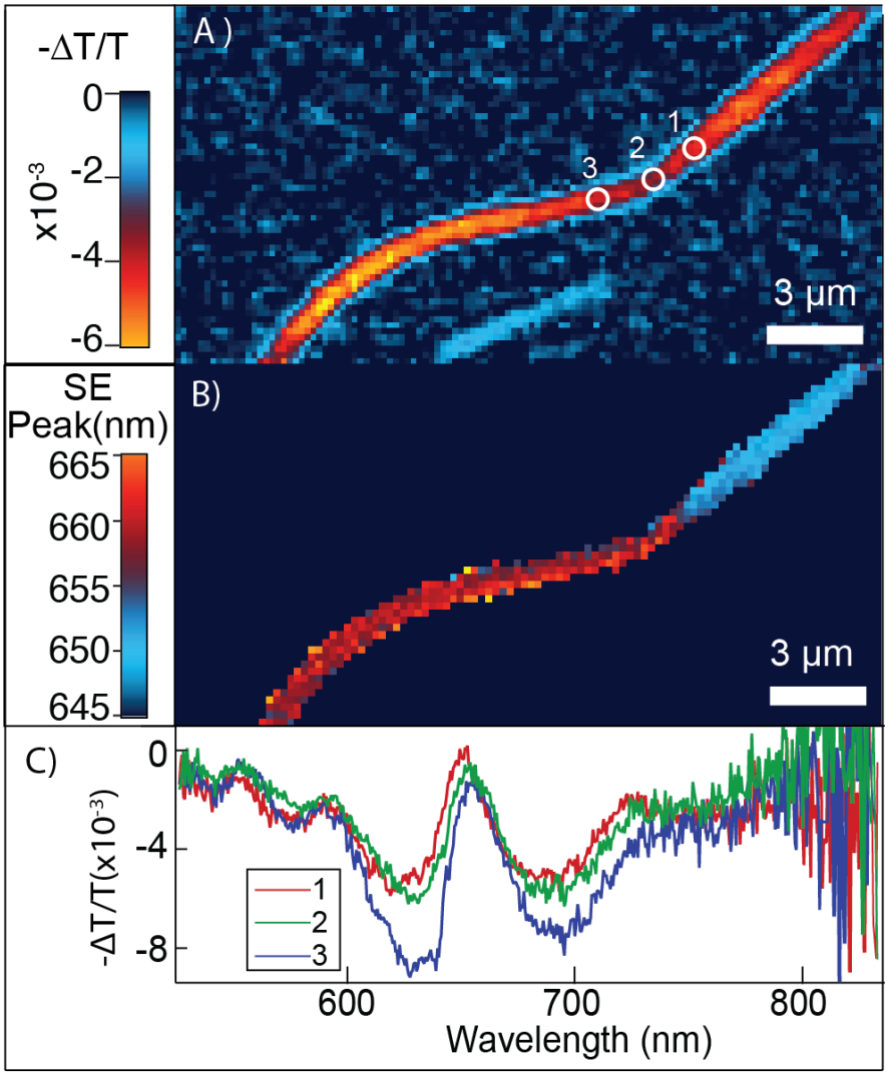

Figure 5.3: Spectral evolution within a bent structure. (A) Transient transmission image of a bent rod. (B) transient transmission spectra collected on marked spots shown in panel (A). (C)Stimulated emission peak position image of the bent rod shown in panel (A).

The fact that a two-color pump-probe study on PCN-222 bent rod with 400 nm excitation has shown a ~100 ps variation of averaged relaxation lifetime suggests that the structural heterogeneity influences the excited state relaxation dynamic.[131] However, this behavior is not consistent with the relaxation dynamics observed in the broadband transient spectra. To investigate this inconsistency between broadband (at 517 nm) and two-color (at 400 nm) relaxation dynamics, we made a direct comparison of the excited state relaxation on a bent rod excited at 400 nm and 530 nm using two-color pump-probe microscopy. We hypothesized that exciting at 400 nm, which excites into the Soret band, would create excited states that are delocalized due to enhanced coupling, resulting in more mobile excited states that are likely to access the defect sites, where trap-mediated recombination results in shorter lifetimes in highly defect-concentrated locations. [139] On the contrary, exciting at 530 nm , which excites into the Q bands, yields excited states with much lower mobility due to reduced coupling, which has a low probability of encountering local defect sites excitation.

To test this hypothesis, we used two-color pump-probe microscopy to measure kinetics on a bent PCN-222 rod at the same location upon photoexcitation at the Soret band (400 nm) and Q band (530 nm), probing at 800 nm. The transient transmission image in Figure 5.4 panel A shows the microrod, where the kinetics shown in Figures 5.4B and 5.4C were collected. In the straight part of the rod, the kinetics from both 400 nm and 530 nm excitation show similar relaxation (black and purple trace in panels B and C), suggesting that the straight region supposedly have lower defect density. On the contrary, in the bent region, kinetics from 400 nm excitation exhibit a significant variation in lifetime (green, blue, and red traces in Figure 5.4 panel B). The kinetics from 530 nm excitation do not show this variability and closely match the

kinetics collected in the straight regions, as shown in Figure 5.4C (Fitting parameters are in Table B2 and B3). The subtle variation in relaxation within a microrod observed in dual color pump-probe with Q band excitation is consistent with our observation made in broadband pump-probe microscopy. Perhaps Q band excitation creates excited states that are spatially separated from defects, and therefore, Q band excited states never encounter them, resulting in small variations in relaxation. The comparison of kinetics relaxation for Soret and Q band excitation supports our theory that excitation into the Soret band produces excited states that are more likely to transport and encounter local trap sites, resulting in heterogeneous relaxation.

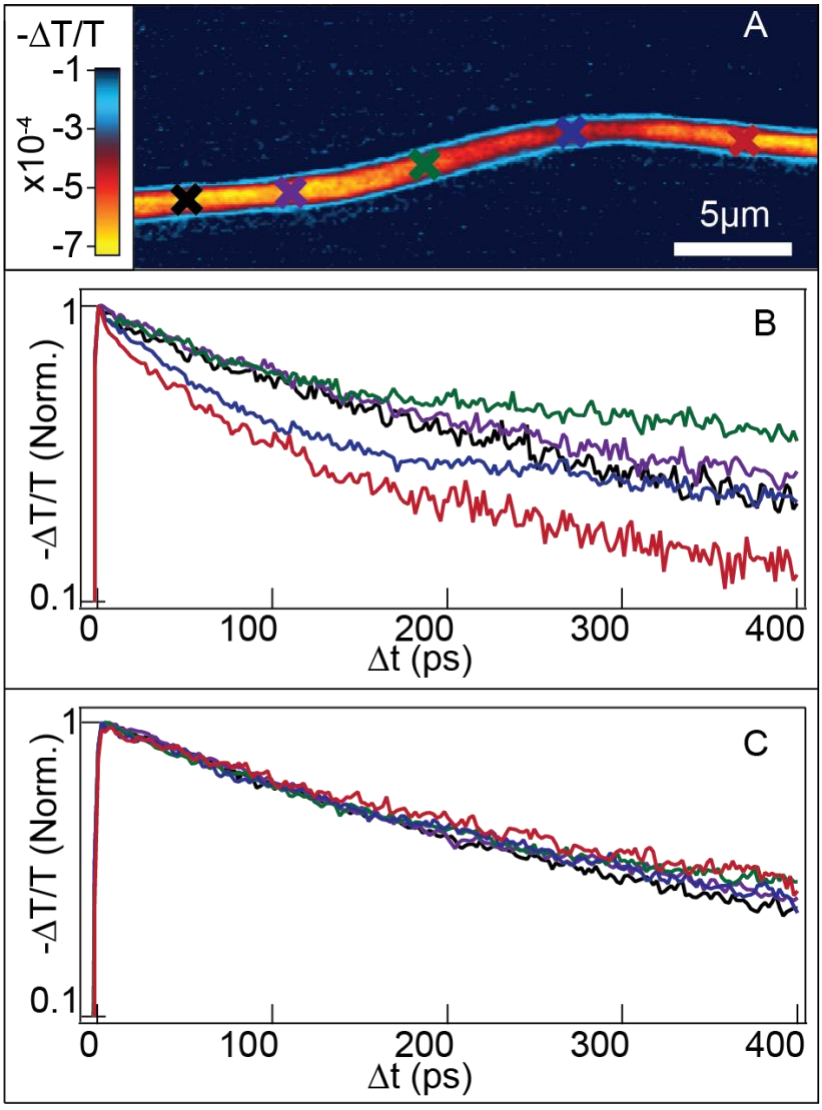

Figure 5.4:(A) Pump-probe image of a bent rod, cross marks are where relaxation kinetics are collected (B) relaxation kinetics from Soret band excitation. (C) relaxation kinetics from Q band excitation.

The excited state transport measurement from the Soret band and Q band excitation can provide concrete evidence of the mobility of the excited state resulting from enhanced or reduced coupling. Soret band excitation has shown power-independent lifetimes below power densities of 41μJ/cm^2 (8.25x10^{13} photons/cm^2), whereas the Q band excitation shows power independence up

to 80.5μJ/cm^2 (2.09x10^{14} photons/cm^2)(Power study shown in the Figure B2). The power studies strongly support our hypothesis that Soret band excitation yields more mobile excited state species than Q band excitation. Excited state transport in PCN-222 microstructures has been reported to be rapid (0.27 to 1 cm^2/s) and sub-diffusive, consistent with the cooling and subsequent trapping of hot carriers [140]. We measured the transport properties of the excited state from the Soret band and Q band excitation to prove our hypothesis.

In order to measure exciton transport, we used spatially separated pump-probe microscopy. The probe beam was fixed at a certain location on the rod (Figure 5.5A) while the pump beam was scanned over the probe. Since the microrod width is narrow, we could only measure transport along the long (c) axis. The resulting profiles, collected at various pump-probe delay times, allowed us to directly probe excited state transport in real space. In the case of diffusive transport, the mean square deviation (MSD) of the profile increases linearly with delay time, Δt. In Figure 5.5 panel B, the MSD is increasing sublinearly, resulting in subdiffusive transport from the Soret band excitation (blue trace). [121] In Figure 5.5 panel B the green trace is representing the transport measurement from Q band excitation, where the MSD is not showing any increase with delay time resulting in no evidence of exciton transport. These two transport measurements were conducted at the locations indicated in Figure 5.5 4A. The plot in Figure 5.5C illustrates the distribution of time-averaged diffusion coefficients, resulting from three measurements each for Soret (blue) and Q band excitation (green). Q band excitation generates carriers that show no detectable transport, yet the excited state generated from Soret band excitation displays rapid sub-diffusive transport.

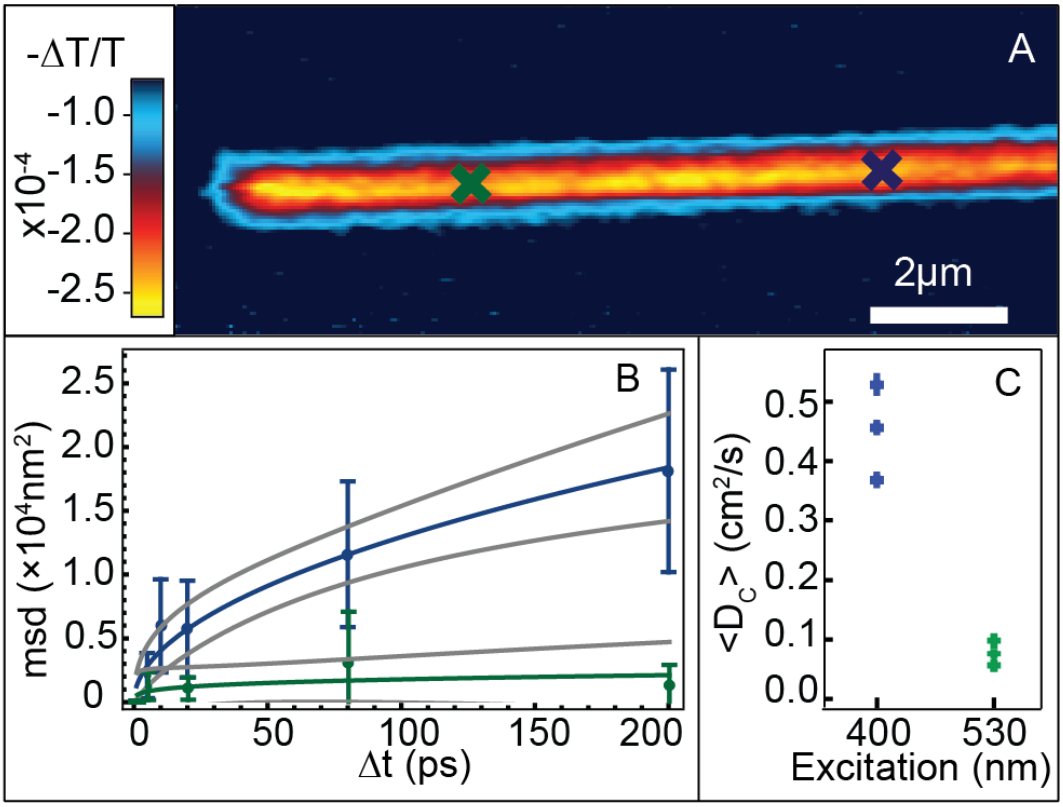

Figure 5.5 (A) Pump-probe image of a microrod the transport measurements are conducted (B) MSD vs. Δt for 400nm (blue) and 520nm (green) excitation, blue and green line are the fits with confidence intervals in gray (C) Exciton dependent time averaged diffusion coefficients for 400nm (blue) and 520nm (green) excitation collected on a same domain.

The results presented above lead to several important conclusions. Firstly, the transport of excitons in PCN-222 is rapid and sub-diffusive when carriers are excited with excess energy into the Soret band. As shown by the exciton transport measurements shown in Figure 5.5, excitons are highly mobile after photogeneration using 400 nm light. The diffusion length of these excitons varies from crystal to crystal but generally is around 100 nm. This large diffusion length means that the excitons are likely to sample many sites in the crystal structure and are likely to encounter relatively low-concentration defect sites and relax by getting trapped into the defect sites (relaxation shown in Figure 5.4 panel B). Secondly, Q band excitation generates less mobile excitons that do not show any measurable transport, as shown in Figure 5.5 , and they are also less likely to encounter the local defect sites and show very small variation in relaxation in figure 5.4 panel C. The difference in excited state behavior between 400 nm excitation and 530 nm excitation is surprising because previous reports have shown that porphyrin MOFs have exhibited relaxation from the Soret band into the Q band in the femtosecond timescale.[54, 111, 141] In such conditions, we would not observe any difference between the Soret band and the Q band relaxation and transport properties. Our fluorescence measurements show strong Soret band emission (Figure 5.1 panel D), which is not possible according to Kasha's rule as the Soret band is not the lowest excited state.[142] The lifetime of the fluorescence measured by TCSPC is shown in Figure (5.6). The Soret band fluorescence lifetime is evident that the Soret band excited state does not relax into the Q band within the femtosecond timescale. Hence, we observe the difference in excited state behavior between the Soret band excitation and the Q band excitation.

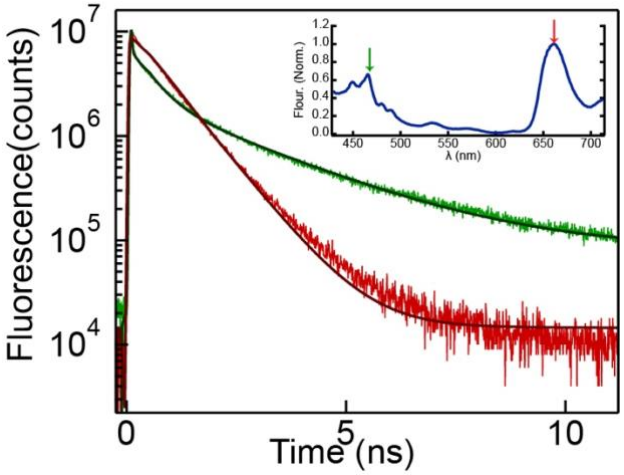

Figure 5.6: Time-correlated single photon counting (TCSPC) measurements showing time-resolved Soret-band emission (466nm) in green and Q_x-band emission (650nm) in red. Q_x-band emission was fit with a single exponential decay(dark red) with a lifetime of 832±9 ps. Soret band emission was fit with a biexponentical decay shown in dark green (τ_1=443±11 ps, τ_2=2.4±0.1ns).

5.5 Conclusion

In summary, we have investigated the excited state dynamics of single-crystal PCN-222 microrods using broadband and two-color pump-probe microscopy. Microscopic steady-state and the first broadband pump-probe spectra demonstrate the spectroscopic features with minimal scattering effects on a single PCN-222 microrod. The hyperspectral broadband imaging illustrates a ~19 nm spectral shift of the $Q_{x(0,0)}$ peak in a microstructure due to local structural heterogeneity. We have revealed that the Soret band and Q band excitation determine the coupling of the chromophores, resulting into more or less mobile excited states. The ability of the excitons to access local trap sites depends on the excitation energy. Rapid (0.39-0.52 cm^2/s) and subdiffusive behavior in transport properties stem from excitons getting trapped in local defect sites when excited into the Soret band. Excited state relaxation also exhibits ~100s ps variation in lifetime for Soret band excitation. Q band excited states do not exhibit the long-range

influence of structural heterogeneity in transport and relaxation. These results highlight the unique transport and relaxation properties of MOF structures arising from different photoexcitation energies and the impact of structural heterogeneity on the excited state dynamics.

CHAPTER SIX

CONCLUSIONS AND FUTURE DIRECTIONS

6.1 Conclusions

The primary goal of this dissertation has been to investigate the influences of structural heterogeneity on the excited state dynamics in solution-processed materials. Chapter 3 outlines the characterization of the excited state dynamics of $CsPbBr_3$ using ultrafast microscopy. In this chapter, we discovered anisotropic exciton diffusion in single crystalline perovskite domains. Moreover, we conducted a thorough analysis of lattice strain, ranging from 10% compressive to 10% tensile strain, and endeavored to establish a correlation between anisotropic diffusion and local lattice strain. Additionally, our investigations delved into the energetic distribution of band energy within microscale domains that showed 20 meV of energy variation within a microstructure. This research revealed the remarkable level of anisotropy in exciton diffusion that is specific to solution-processed lead halide perovskites. Notably, despite efforts, we found no conclusive correlation between diffusion coefficient and lattice strain, suggesting that anisotropic diffusion may be influenced by other forms of structural heterogeneity beyond local lattice strain.

In Chapter 4, we shifted our focus solely to a different class of material called PCN-222 metal-organic frameworks. Specifically, we studied the transport properties, and our experiments showed rapid exciton transport (0.27-1cm^2/s) in a subdiffusive manner. Our transport measurement shows carrier transport 20 times faster than the estimated through forester calculation. Additional information regarding the domain-to-domain heterogeneity of relaxation

dynamics was also reported. Further analysis of relaxation dynamics in straight and bent structures revealed a high structural heterogeneity in bend regions that showed heterogeneous relaxation lifetime. Photoluminescence quenching in bent regions revealed high defect density and defect-mediated nonradiative relaxation.

Finally, in Chapter 5, we carried out a series of two color and broadband pump-probe microscopic investigation experiments on the excited state properties of PCN-222 MOF. PCN-222 showed notably homogeneous relaxation dynamics with broadband pump-probe Microscopy with Q band (517nm) excitation. The hyperspectral imaging illustrates a ~19 nm spectral shift of the $Q_{x(0,0)}$ peak in a microstructure due to local structural heterogeneity. Moreover, with two color investigations, Q band (530 nm) relaxation results in no observable transport and homogeneous relaxation. However, we observed rapid exciton transport (0.39-0.52cm^2/s) and heterogeneous relaxation dynamics with Soret band excitation. This work reveals the surprising fact that Soret band excitation creates excited states with a strong coupling that creates more mobile excitons that have longer diffusion lengths and can access local defect sites. The distinct behavior of the Soret and Q band excitation revealed that the Soret band excited state does not relax into the Q band within the femtosecond timescale, and it is evident from the long-lived fluorescence from the Soret band. These conclusions highlight the distinct transport and relaxation characteristics exhibited by MOF structures, influenced by different photoexcitation energies, and reveal the impact of structural heterogeneity on excited state dynamics.

6.2 Future work

The research in this dissertation presents progress in characterizing the excited state dynamics in solution-processed materials. However, this work also presents some important questions related

to the impact of chemical and structural heterogeneity in porphyrin-based metal-organic frameworks. Specifically, the future aims of this research are to determine (1) the spectral evolution of the Soret band in PCN-222 MOF. (2) what is the cause of observed blueshift in PCN-222 MOF. (3) how excited state dynamics behave in other porphyrin-based MOFs such as PCN-223 and PCN-224.

6.2.1 Understanding the Soret Band Evolution:

The body of work presented in Chapter 5 illustrates transport and relaxation dynamics from both the Soret band and Q band excitation. Spectroscopic investigations reported that exited state species relax into the Q band in the femtosecond timescale. However, we observed long-lived fluorescence from 466nm (Figure 5.6) with time-correlated single photon counting.[126] The steady-state absorption and emission spectra of TCPP monomer and PCN-222 metal-organic framework (solid-state) are shown in Figure 6.1panel A and B, respectively. According to Kasha's rule, fluorescence occurs only from the lowest excited state. [142] Yet, Figure 6.1panel B clearly shows fluorescence from multiple states above the lowest excited state $Q_x(0,0)$ in solid state PCN-222 MOF structures. Peak broadening and redshift of the absorption bands from TCPP monomer to PCN-222 metal-organic framework is a strong indication of chromophore coupling. The ultrafast broadband microscope has allowed us to photoexcite at 517 nm and probe in the wavelength range from 526nm to 800 nm and observe the coupling effect in only Q peaks. Our next steps will be to design experiments to probe from 420nm to 500nm to investigate the long-lived fluorescence from the Soret band and its relaxation pathways. It can also help us understand the change of relative oscillator strength of the Soret band and Q band from TCPP monomer to PCN-222 metal-organic framework. Investigating the spectral evolution in MOF

single structures without solvent effect will elucidate the newfound excited state dynamics in porphyrin MOFs.

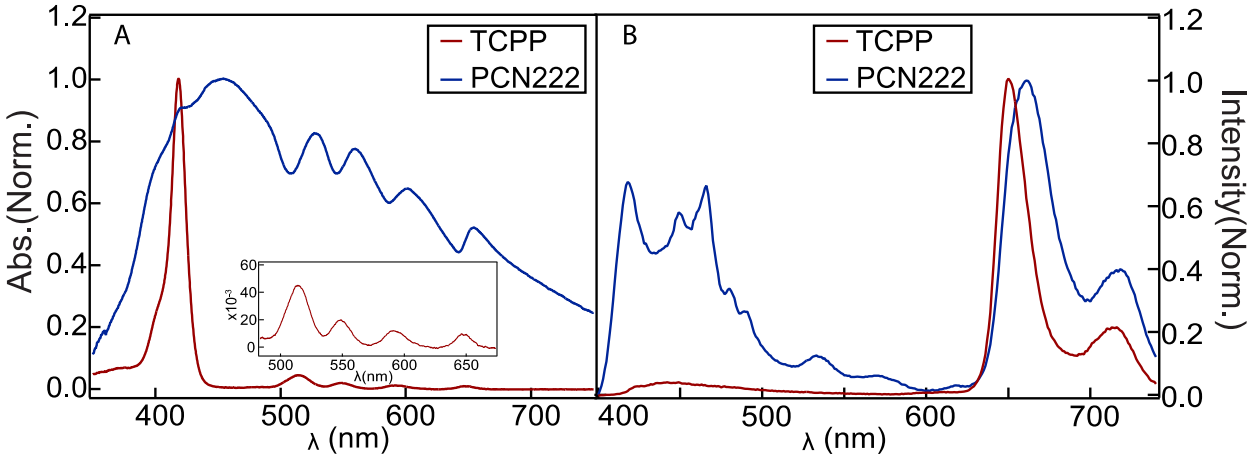

Figure 6.1: The steady-state absorption (panel A) and emission (Panel B) spectra of TCPP monomer and PCN-222 metal-organic framework (solid-state).

6.2.2 Determining the Observed Blue Shift Of The $Q_x(0,0)$ Peak In Structures With Chemical Heterogeneity:

While investigating the broadband spectra of PCN-222 microcrystals, we observed anomalies in the broadband spectra of different synthesized batches of PCN-222. We observed the blueshift of the $Q_x(0,0)$ peak with time, as shown in Figure 6.2. At the same time, we also observed complete quenching of the $Q_x(0,1)$ peak, as shown in the boxed area in Figure 6.2. One potential reason behind this blue shift is the structures are more chemical heterogeneity, or in other words, there are more reaction sites created in the structure. Upon photoexcitation, the reaction sites are actively reacting, creating low energy states resulting in a blue shift in the spectra. Complete quenching of the $Q_x(0,1)$ is evidence of a structure with higher defect density. One potential way to investigate this blue shift will be to synthesize PCN-222 structures with controlled introduction of heterogeneity by changing the chemical composition and aspect ratio.

Consequently, ultrafast broadband pump-probe measurement can quantify the blue shift and a correlation of the spectral shift as a function of introduced defect density will elucidate the foundation of the blue shift of $Q_x(0,0)$ peak.

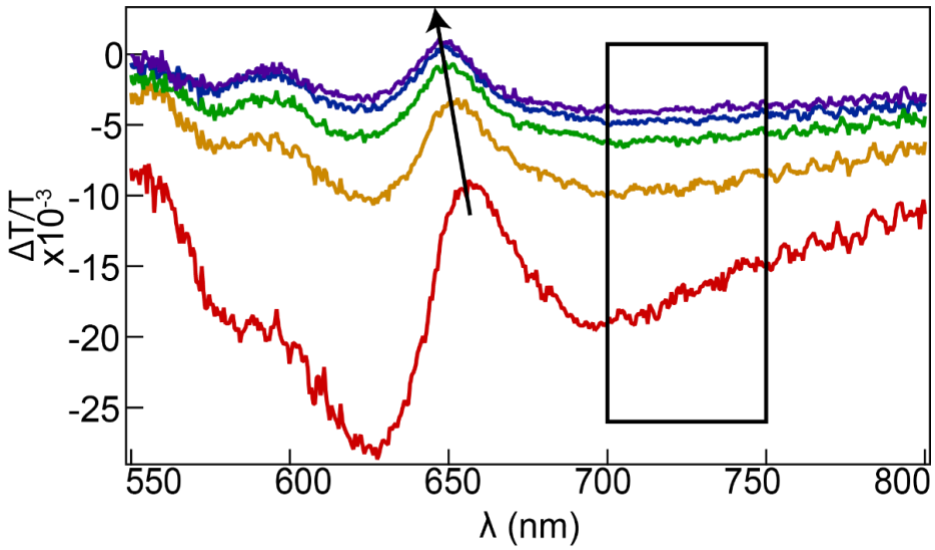

Figure 6.2: Time evolution of broadband spectra illustrating the blue shift.

6.2.3 Careful Synthesis and Characterization Of Excited State Dynamics In Other Porphyrin MOF Structures:

In order to understand structure dependence on the excited state dynamics, we investigated another porphyrin MOF called PCN-223. In SEM images in panel A, we can see two distinctive structures Figure 6.3 panel A. Figure 6.3 Panel A(ii) is more similar to the PCN-224 structure[143]. The XRD of the PCN-223 sample (red trace) shows some overlap of PCN-223(blue) and PCN-224 (green trace) peaks. Then, it is evident that the PCN-223 sample we were investigating is not phase pure. The transient transmission broadband spectra clearly show blue-shifted spectra on round-shaped structures (supposed PCN-224) compared to pill-shaped PCN-223 structures (Figure 6.3 panel C). The relaxation dynamics also showed faster relaxation

for round-shaped structures (supposed PCN-224). However, there is no way to distinguish between two different structures other than their shape. To understand structure-dependent excited state dynamics, we need careful growth of phase pure PCN-223 and PCN-224 to determine a correlation between the excited state dynamics and chemical structure.

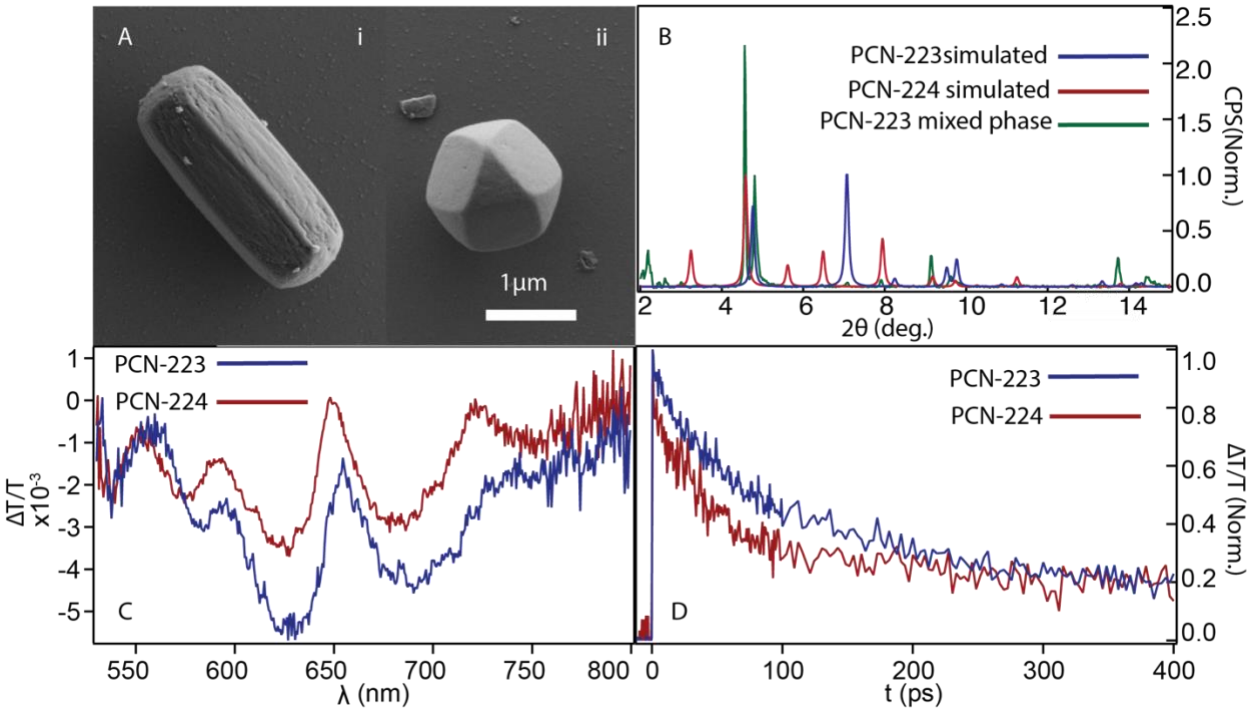

Figure 6.3 excited state dynamics in different structures. Panel (A) SEM images of 223 structures i) and ii) show pill-shaped and round-shaped PCN-223 structures, respectively. B) XRD peaks illustrating XRD peaks collected from PCN-223, which showed peaks from both PCN-223 and PCN-224. C) Broadband spectra of pill-shaped (PCN-223) and round-shaped (PCN-224) showed spectral shift. D) Kinetics traces from both structures showed relaxation lifetime variation.

CUMULATIVE REFERENCES CITED

(1) Eslamian, M. Spray-on Thin Film PV Solar Cells: Advances, Potentials and Challenges. *Coatings* **2014**, *4* (1), 60-84. DOI: 10.3390/coatings4010060.

(2) Shah, A.; Torres, P.; Tscharner, R.; Wyrsch, N.; Keppner, H. Photovoltaic technology: The case for thin-film solar cells. *Science* **1999**, *285* (5428), 692-698. DOI: DOI 10.1126/science.285.5428.692.

(3) Pastuszak, J.; Wegierek, P. Photovoltaic Cell Generations and Current Research Directions for Their Development. *Materials* **2022**, *15* (16). DOI: ARTN 5542 10.3390/ma15165542.

(4) Kichou, S.; Silvestre, S.; Nofuentes, G.; Torres-Ramírez, M.; Chouder, A.; Guasch, D. Characterization of degradation and evaluation of model parameters of amorphous silicon photovoltaic modules under outdoor long term exposure. *Energy* **2016**, *96*, 231-241. DOI: 10.1016/j.energy.2015.12.054.

(5) Wang, Q.; Xie, Y.; Soltani-Kordshuli, F.; Eslamian, M. Progress in emerging solution-processed thin film solar cells - Part I: Polymer solar cells. *Renew Sust Energ Rev* **2016**, *56*, 347-361. DOI: 10.1016/j.rser.2015.11.063.

(6) Green, M. A.; Ho-Baillie, A.; Snaith, H. J. The emergence of perovskite solar cells. *Nat Photonics* **2014**, *8* (7), 506-514. DOI: 10.1038/Nphoton.2014.134.

(7) Eslamian, M. Inorganic and Organic Solution-Processed Thin Film Devices. *Nanomicro Lett* **2017**, *9* (1), 3. DOI: 10.1007/s40820-016-0106-4 From NLM PubMed-not-MEDLINE.

(8) Yip, H. L.; Jen, A. K. Y. Recent advances in solution-processed interfacial materials for efficient and stable polymer solar cells. *Energ Environ Sci* **2012**, *5* (3), 5994-6011. DOI: 10.1039/c2ee02806a.

(9) Voznyy, O.; Sutherland, B. R.; Ip, A. H.; Zhitomirsky, D.; Sargent, E. H. Engineering charge transport by heterostructuring solution-processed semiconductors. *Nat Rev Mater* **2017**, *2* (6). DOI: ARTN 17026 10.1038/natrevmats.2017.26.

(10) Lu, K. K.; Li, X. M.; Sun, Q. Q.; Pang, X. C.; Chen, J. Z.; Minari, T.; Liu, X. Y.; Song, Y. L. Solution-processed electronics for artificial synapses. *Mater Horiz* **2021**, *8* (2), 447-470. DOI: 10.1039/d0mh01520b.

(11) Park, S.; Kim, T.; Yoon, S.; Koh, C. W.; Woo, H. Y.; Son, H. J. Progress in Materials, Solution Processes, and Long-Term Stability for Large-Area Organic Photovoltaics. *Adv Mater* **2020**, *32* (51). DOI: ARTN 2002217 10.1002/adma.202002217.

(12) Butt, M. A. Thin-Film Coating Methods: A Successful Marriage of High-Quality and Cost-Effectiveness-A Brief Exploration. *Coatings* **2022**, *12* (8). DOI: ARTN 1115 10.3390/coatings12081115.

(13) Xing, G. C.; Mathews, N.; Lim, S. S.; Yantara, N.; Liu, X. F.; Sabba, D.; Grätzel, M.; Mhaisalkar, S.; Sum, T. C. Low-temperature solution-processed wavelength-tunable perovskites for lasing. *Nat Mater* **2014**, *13* (5), 476-480. DOI: 10.1038/Nmat3911.

(14) Kislenko, V. A.; Pavlov, S. V.; Kislenko, S. A. Influence of defects in graphene on electron transfer kinetics: The role of the surface electronic structure. *Electrochim Acta* **2020**, *341*. DOI: ARTN 136011 10.1016/j.electacta.2020.136011.

(15) Liu, W.; Yu, H. R.; Li, Y. L.; Hu, A. Q.; Wang, J.; Lu, G. W.; Li, X. F.; Yang, H.; Dai, L.; Wang, S. F.; Gong, Q. H. Mapping Trap Dynamics in a CsPbBr Single-Crystal Microplate by Ultrafast Photoemission Electron Microscopy. *Nano Lett* **2021**, *21* (7), 2932-2938. DOI: 10.1021/acs.nanolett.1c00014.

(16) Polishchuk, S.; Puppin, M.; Crepaldi, A.; Gatti, G.; Dirin, D. N.; Nazarenko, O.; Colonna, N.; Marzari, N.; Kovalenko, M. V.; Grioni, M.; Chergui, M. Nanoscale-Resolved Surface-to-Bulk Electron Transport in CsPbBr Perovskite. *Nano Lett* **2022**, *22* (3), 1067-1074. DOI: 10.1021/acs.nanolett.1c03941.

(17) Jones, T. W.; Osherov, A.; Alsari, M.; Sponseller, M.; Duck, B. C.; Jung, Y. K.; Settens, C.; Niroui, F.; Brenes, R.; Stan, C. V.; et al. Lattice strain causes non-radiative losses in halide perovskites. *Energ Environ Sci* **2019**, *12* (2), 596-606. DOI: 10.1039/c8ee02751j.

(18) Zhao, J. J.; Deng, Y. H.; Wei, H. T.; Zheng, X. P.; Yu, Z. H.; Shao, Y. C.; Shield, J. E.; Huang, J. S. Strained hybrid perovskite thin films and their impact on the intrinsic stability of perovskite solar cells. *Sci Adv* **2017**, *3* (11). DOI: ARTN eaao5616 10.1126/sciadv.aao5616.

(19) Ameloot, R.; Vermoortele, F.; Hofkens, J.; De Schryver, F. C.; De Vos, D. E.; Roeffaers, M. B. J. Three-Dimensional Visualization of Defects Formed during the Synthesis of Metal-Organic Frameworks: A Fluorescence Microscopy Study. *Angew Chem Int Edit* **2013**, *52* (1), 401-405. DOI: 10.1002/anie.201205627.

(20) Cai, W. X.; Lee, T.; Lee, M.; Cho, W.; Han, D. Y.; Choi, N.; Yip, A. C. K.; Choi, J. Thermal Structural Transitions and Carbon Dioxide Adsorption Properties of Zeolitic Imidazolate Framework-7 (ZIF-7). *J Am Chem Soc* **2014**, *136* (22), 7961-7971. DOI: 10.1021/ja5016298.

(21) Zhu, T.; Snaider, J. M.; Yuan, L.; Huang, L. B. Ultrafast Dynamic Microscopy of Carrier and Exciton Transport. *Annu Rev Phys Chem* **2019**, *70*, 219-244. DOI: 10.1146/annurev-physchem-042018-052605.

(22) Schnedermann, C.; Sung, J.; Pandya, R.; Verma, S. D.; Chen, R. Y. S.; Gauriot, N.; Bretscher, H. M.; Kukura, P.; Rao, A. Ultrafast Tracking of Exciton and Charge Carrier Transport in Optoelectronic Materials on the Nanometer Scale. *J Phys Chem Lett* **2019**, *10* (21), 6727-6733. DOI: 10.1021/acs.jpclett.9b02437.

(23) Nishida, J.; Johnson, S. C.; Chang, P. T. S.; Wharton, D. M.; Dönges, S. A.; Khatib, O.; Raschke, M. B. Ultrafast infrared nano-imaging of far-from-equilibrium carrier and vibrational dynamics. *Nat Commun* **2022**, *13* (1). DOI: ARTN 1083 10.1038/s41467-022-28224-9.

(24) Huang, L. B.; Cheng, J. X. Nonlinear Optical Microscopy of Single Nanostructures. *Annu Rev Mater Res* **2013**, *43*, 213-236. DOI: 10.1146/annurev-matsci-071312-121652.

(25) Mukamel, S. *Principles of nonlinear optical spectroscopy*; Oxford University Press, 1995.

(26) Sabbah, A. J.; Riffe, D. M. Femtosecond pump-probe reflectivity study of silicon carrier dynamics. *Phys Rev B* **2002**, *66* (16). DOI: ARTN 165217 10.1103/PhysRevB.66.165217.

(27) Bennett, B. R.; Soref, R. A.; Delalamo, J. A. Carrier-Induced Change in Refractive-Index of Inp, Gaas, and Ingaasp. *Ieee J Quantum Elect* **1990**, *26* (1), 113-122. DOI: Doi 10.1109/3.44924.

(28) Uskoković, D. P.; Milonjić, S. K.; Raković, D. I. *Recent developments in advanced materials and processes*; Trans Tech Publications Ltd, 2006.

(29) Yu, Z. G.; Krishnamurthy, S.; Guha, S. Photoexcited-carrier-induced refractive index change in small bandgap semiconductors. *J Opt Soc Am B* **2006**, *23* (11), 2356-2360. DOI: Doi 10.1364/Josab.23.002356.

(30) Esser, A.; Kutt, W.; Strahnen, M.; Maidorn, G.; Kurz, H. Femtosecond Transient Reflectivity Measurements as a Probe for Process-Induced Defects in Silicon. *Appl Surf Sci* **1990**, *46* (1-4), 446-450. DOI: Doi 10.1016/0169-4332(90)90187-5.

(31) Hill, A. H.; Kennedy, C. L.; Massaro, E. S.; Grumstrup, E. M. Perovskite Carrier Transport: Disentangling the Impacts of Effective Mass and Scattering Time Through Microscopic Optical Detection. *J Phys Chem Lett* **2018**, *9* (11), 2808-2813. DOI: 10.1021/acs.jpclett.8b00652.

(32) Li, Z. H.; He, J. X.; Lv, X. H.; Chi, L. F.; Egbo, K. O.; Li, M.-D.; Tanaka, T.; Guo, Q. X.; Yu, K. M.; Liu, C. P. Optoelectronic properties and ultrafast carrier dynamics of copper iodide thin films. *Nat Commun* **2022**, *13* (1), 6346. DOI: 10.1038/s41467-022-34117-8.

(33) Prasankumar, R. P.; Chow, W. W.; Urayama, J.; Attaluri, R. S.; Shenoi, R. V.; Krishna, S.; Taylor, A. J. Density-dependent carrier dynamics in a quantum dots-in-a-well heterostructure. *Applied Physics Letters* **2010**, *96* (3). DOI: 10.1063/1.3294309 (acccessed 4/16/2024).

(34) Kennedy, C. L.; Hill, A. H.; Massaro, E. S.; Grumstrup, E. M. Ultrafast Excited-State Transport and Decay Dynamics in Cesium Lead Mixed Halide Perovskites. *Acs Energy Lett* **2017**, *2* (7), 1501-1506. DOI: 10.1021/acsenergylett.7b00257.

(35) Feron, K.; Belcher, W. J.; Fell, C. J.; Dastoor, P. C. Organic solar cells: understanding the role of Förster resonance energy transfer. *Int J Mol Sci* **2012**, *13* (12), 17019-17047. DOI: 10.3390/ijms131217019 From NLM.

(36) Wenk, H.-R.; Bulakh, A. G. *Minerals : their constitution and origin*; Cambridge University Press, 2004.

(37) Kim, M.; Kim, J. H.; Kim, M.; Kim, C. S.; Choi, J. W.; Choi, K.; Lee, J. H.; Park, J.; Kang, Y. C.; Jin, S. H.; Song, M. Enhanced photoluminescence quantum efficiency and stability of water assisted CsPbBr
perovskite nanocrystals. *J Ind Eng Chem* **2020**, *88*, 84-89. DOI: 10.1016/j.jiec.2020.04.027.

(38) Tennyson, E. M.; Doherty, T. A. S.; Stranks, S. D. Heterogeneity at multiple length scales in halide perovskite semiconductors. *Nat Rev Mater* **2019**, *4* (9), 573-587. DOI: 10.1038/s41578-019-0125-0.

(39) deQuilettes, D. W.; Vorpahl, S. M.; Stranks, S. D.; Nagaoka, H.; Eperon, G. E.; Ziffer, M. E.; Snaith, H. J.; Ginger, D. S. Impact of microstructure on local carrier lifetime in perovskite solar cells. *Science* **2015**, *348* (6235), 683-686. DOI: 10.1126/science.aaa5333.

(40) Guo, Z.; Manser, J. S.; Wan, Y.; Kamat, P. V.; Huang, L. B. Spatial and temporal imaging of long-range charge transport in perovskite thin films by ultrafast microscopy. *Nat Commun* **2015**, *6*. DOI: ARTN 7471
10.1038/ncomms8471.

(41) Leblebici, S. Y.; Leppert, L.; Li, Y.; Reyes-Lillo, S. E.; Wickenburg, S.; Wong, E.; Lee, J.; Melli, M.; Ziegler, D.; Angell, D. K.; et al. Facet-dependent photovoltaic efficiency variations in single grains of hybrid halide perovskite. *Nat Energy* **2016**, *1*. DOI: Artn 16093
10.1038/Nenergy.2016.93.

(42) Landsberg, P. T. Non-Radiative Transitions in Semiconductors. *Phys Status Solidi* **1970**, *41* (2), 457-+. DOI: DOI 10.1002/pssb.19700410202.

(43) Zhu, Y. Z.; Cui, Q. N.; Chen, J. P.; Chen, F.; Shi, Z. L.; Zhao, X. W.; Xu, C. X. Inhomogeneous Trap-State-Mediated Ultrafast Photocarrier Dynamics in CsPbBr Microplates. *Acs Applied Materials & Interfaces* **2021**, *13* (5), 6820-6829. DOI: 10.1021/acsami.0c20733.

(44) Long, J. R.; Yaghi, O. M. The pervasive chemistry of metal-organic frameworks. *Chem Soc Rev* **2009**, *38* (5), 1213-1214. DOI: 10.1039/b903811f.

(45) Zhou, H. C.; Long, J. R.; Yaghi, O. M. Introduction to Metal-Organic Frameworks. *Chem Rev* **2012**, *112* (2), 673-674. DOI: 10.1021/cr300014x.

(46) O'Keeffe, M.; Yaghi, O. M. Deconstructing the Crystal Structures of Metal-Organic Frameworks and Related Materials into Their Underlying Nets. *Chem Rev* **2012**, *112* (2), 675-702. DOI: 10.1021/cr200205j.

(47) Tranchemontagne, D. J.; Mendoza-Cortés, J. L.; O'Keeffe, M.; Yaghi, O. M. Secondary building units, nets and bonding in the chemistry of metal–organic frameworks. *Chem Soc Rev* **2009**, *38* (5), 1257-1283, 10.1039/B817735J. DOI: 10.1039/B817735J.

(48) Rowsell, J. L. C.; Yaghi, O. M. Metal-organic frameworks: a new class of porous materials. *Micropor Mesopor Mat* **2004**, *73* (1-2), 3-14. DOI: 10.1016/j.micromeso.2004.03.034.

(49) Jiao, L.; Seow, J. Y. R.; Skinner, W. S.; Wang, Z. U.; Jiang, H. L. Metal-organic frameworks: Structures and functional applications. *Mater Today* **2019**, *27*, 43-68. DOI: 10.1016/j.mattod.2018.10.038.

(50) Hu, Z. J.; Meng, J.; Wang, X. M.; Li, W. T.; Chen, X. W. Tailoring the Surface Properties of Co-based Metal-Organic Frameworks for Highly Efficient and Selective Enrichment of Immunoglobulin G. *Acs Applied Materials & Interfaces* **2020**, *12* (49), 55453-55459. DOI: 10.1021/acsami.0c16821.

(51) Xu, H. Q.; Hu, J. H.; Wang, D. K.; Li, Z. H.; Zhang, Q.; Luo, Y.; Yu, S. H.; Jiang, H. L. Visible-Light Photoreduction of CO2 in a Metal-Organic Framework: Boosting Electron-Hole Separation via Electron Trap States. *J Am Chem Soc* **2015**, *137* (42), 13440-13443. DOI: 10.1021/jacs.5b08773.

(52) Kim, D.; Liu, X. F.; Lah, M. S. Topology analysis of metal-organic frameworks based on metal-organic polyhedra as secondary or tertiary building units. *Inorg Chem Front* **2015**, *2* (4), 336-360. DOI: 10.1039/c4qi00236a.

(53) Lee, C. Y.; Farha, O. K.; Hong, B. J.; Sarjeant, A. A.; Nguyen, S. T.; Hupp, J. T. Light-Harvesting Metal-Organic Frameworks (MOFs): Efficient Strut-to-Strut Energy Transfer in Bodipy and Porphyrin-Based MOFs. *J Am Chem Soc* **2011**, *133* (40), 15858-15861. DOI: 10.1021/ja206029a.

(54) Shaikh, S. M.; Chakraborty, A.; Alatis, J.; Cai, M.; Danilov, E.; Morris, A. J. Light harvesting and energy transfer in a porphyrin-based metal organic framework. *Faraday Discuss* **2019**, *216*, 174-190. DOI: 10.1039/c8fd00194d.

(55) So, M. C.; Wiederrecht, G. P.; Mondloch, J. E.; Hupp, J. T.; Farha, O. K. Metal–organic framework materials for light-harvesting and energy transfer. *Chem Commun* **2015**, *51* (17), 3501-3510, 10.1039/C4CC09596K. DOI: 10.1039/C4CC09596K.

(56) Feng, D. W.; Gu, Z. Y.; Li, J. R.; Jiang, H. L.; Wei, Z. W.; Zhou, H. C. Zirconium-Metalloporphyrin PCN-222: Mesoporous Metal-Organic Frameworks with Ultrahigh Stability as Biomimetic Catalysts. *Angew Chem Int Edit* **2012**, *51* (41), 10307-10310. DOI: 10.1002/anie.201204475.

(57) Jiang, H.-L.; Feng, D.; Wang, K.; Gu, Z.-Y.; Wei, Z.; Chen, Y.-P.; Zhou, H.-C. An Exceptionally Stable, Porphyrinic Zr Metal–Organic Framework Exhibiting pH-Dependent Fluorescence. *J Am Chem Soc* **2013**, *135* (37), 13934-13938. DOI: 10.1021/ja406844r.

(58) Deria, P.; Gómez-Gualdrón, D. A.; Hod, I.; Snurr, R. Q.; Hupp, J. T.; Farha, O. K. Framework-Topology-Dependent Catalytic Activity of Zirconium-Based (Porphinato)zinc(II) MOFs. *J Am Chem Soc* **2016**, *138* (43), 14449-14457. DOI: 10.1021/jacs.6b09113.

(59) Morris, W.; Volosskiy, B.; Demir, S.; Gándara, F.; McGrier, P. L.; Furukawa, H.; Cascio, D.; Stoddart, J. F.; Yaghi, O. M. Synthesis, Structure, and Metalation of Two New Highly Porous Zirconium Metal–Organic Frameworks. *Inorg Chem* **2012**, *51* (12), 6443-6445. DOI: 10.1021/ic300825s.

(60) Baskin, J. S.; Yu, H.-Z.; Zewail, A. H. Ultrafast Dynamics of Porphyrins in the Condensed Phase: I. Free Base Tetraphenylporphyrin. *The Journal of Physical Chemistry A* **2002**, *106* (42), 9837-9844. DOI: 10.1021/jp020398g.

(61) Hanna, L.; Movsesian, E.; Orozco, M.; Bernot Jr, A. R.; Asadinamin, M.; Shenje, L.; Ullrich, S.; Zhao, Y.; Marshall, N.; Weeks, J. A.; et al. Spectroscopic investigation of the electronic and excited state properties of para-substituted tetraphenyl porphyrins and their electrochemically generated ions. *Spectrochimica Acta Part A: Molecular and Biomolecular Spectroscopy* **2022**, *278*, 121300. DOI: https://doi.org/10.1016/j.saa.2022.121300.

(62) Hashimoto, T.; Choe, Y. K.; Nakano, H.; Hirao, K. Theoretical study of the Q and B bands of free-base, magnesium, and zinc porphyrins, and their derivatives. *J Phys Chem A* **1999**, *103* (12), 1894-1904. DOI: DOI 10.1021/jp984807d.

(63) Jin, S. Y.; Son, H. J.; Farha, O. K.; Wiederrecht, G. P.; Hupp, J. T. Energy Transfer from Quantum Dots to Metal-Organic Frameworks for Enhanced Light Harvesting. *J Am Chem Soc* **2013**, *135* (3), 955-958. DOI: 10.1021/ja3097114.

(64) Shaikh, Shaunak M.; Chakraborty, A.; Alatis, J.; Cai, M.; Danilov, E.; Morris, A. J. Light harvesting and energy transfer in a porphyrin-based metal organic framework. *Faraday Discussions* **2019**, *216* (0), 174-190, 10.1039/C8FD00194D. DOI: 10.1039/C8FD00194D.

(65) Xu, H. Q.; Hu, J. H.; Wang, D. K.; Li, Z. H.; Zhang, Q.; Luo, Y.; Yu, S. H.; Jiang, H. L. Visible-Light Photoreduction of CO
in a Metal-Organic Framework: Boosting Electron-Hole Separation via Electron Trap States. *J Am Chem Soc* **2015**, *137* (42), 13440-13443. DOI: 10.1021/jacs.5b08773.

(66) Hill, A. H.; Smyser, K. E.; Kennedy, C. L.; Massaro, E. S.; Grumstrup, E. M. Screened Charge Carrier Transport in Methylammonium Lead Iodide Perovskite Thin Films. *J Phys Chem Lett* **2017**, *8* (5), 948-953. DOI: 10.1021/acs.jpclett.7b00046.

(67) Piland, G.; Grumstrup, E. M. High-Repetition Rate Broadband Pump-Probe Microscopy. *J Phys Chem A* **2019**, *123* (40), 8709-8716. DOI: 10.1021/acs.jpca.9b03858.

(68) Grazulis, S.; Daskevic, A.; Merkys, A.; Chateigner, D.; Lutterotti, L.; Quiros, M.; Serebryanaya, N. R.; Moeck, P.; Downs, R. T.; Le Bail, A. Crystallography Open Database (COD): an open-access collection of crystal structures and platform for world-wide collaboration. *Nucleic Acids Res* **2012**, *40* (Database issue), D420-427. DOI: 10.1093/nar/gkr900 From NLM Medline.

(69) Quirós, M.; Grazulis, S.; Girdzijauskaite, S.; Merkys, A.; Vaitkus, A. Using SMILES strings for the description of chemical connectivity in the Crystallography Open Database. *J Cheminformatics* **2018**, *10*. DOI: ARTN 23 10.1186/s13321-018-0279-6.

(70) Hickey, C. L.; Grumstrup, E. M. Direct Correlation of Charge Carrier Transport to Local Crystal Quality in Lead Halide Perovskites. *Nano Lett* **2020**, *20* (7), 5050-5056. DOI: 10.1021/acs.nanolett.0c01244.

(71) Bonnett, B. L.; Smith, E. D.; De La Garza, M.; Cai, M.; Haag, J. V. I. V.; Serrano, J. M.; Cornell, H. D.; Gibbons, B.; Martin, S. M.; Morris, A. J. PCN-222 Metal–Organic Framework Nanoparticles with Tunable Pore Size for Nanocomposite Reverse Osmosis Membranes. *ACS Applied Materials & Interfaces* **2020**, *12* (13), 15765-15773. DOI: 10.1021/acsami.0c04349.

(72) Yang, X. Z.; Bonnett, B. L.; Spiering, G. A.; Cornell, H. D.; Gibbons, B. J.; Moore, R. B.; Foster, E. J.; Morris, A. J. Understanding the Mechanical Reinforcement of Metal-Organic Framework-Polymer Composites: The Effect of Aspect Ratio. *Acs Applied Materials & Interfaces* **2021**, *13* (44), 51894-51905. DOI: 10.1021/acsami.1c05430.

(73) Sadhukhan, P.; Roy, A.; Sengupta, P.; Das, S.; Mallick, T. K.; Nazeeruddin, M. K.; Sundaram, S. The emergence of concentrator photovoltaics for perovskite solar cells. *Appl Phys Rev* **2021**, *8* (4). DOI: Artn 041324 10.1063/5.0062671.

(74) Jung, H. S.; Park, N. G. Perovskite Solar Cells: From Materials to Devices. *Small* **2015**, *11* (1), 10-25. DOI: 10.1002/smll.201402767.

(75) Hu, Z. S.; Lin, Z. H.; Su, J.; Zhang, J. C.; Chang, J. J.; Hao, Y. A Review on Energy Band-Gap Engineering for Perovskite Photovoltaics. *Sol Rrl* **2019**, *3* (12). DOI: ARTN 1900304 10.1002/solr.201900304.

(76) Zhang, H. L.; Ji, X.; Xu, H. Y.; Zhang, R.; Zhang, H. Design and modification of perovskite materials for photocatalytic performance improvement. *J Environ Chem Eng* **2023**, *11* (1). DOI: ARTN 109056
10.1016/j.jece.2022.109056.

(77) Kulkarni, S. A.; Baikie, T.; Boix, P. P.; Yantara, N.; Mathews, N.; Mhaisalkar, S. Band-gap tuning of lead halide perovskites using a sequential deposition process. *J Mater Chem A* **2014**, *2* (24), 9221-9225. DOI: 10.1039/c4ta00435c.

(78) Yang, F.; Jang, D.; Dong, L. R.; Qiu, S. D.; Distler, A.; Li, N.; Brabec, C. J.; Egelhaaf, H. J. Upscaling Solution-Processed Perovskite Photovoltaics. *Adv Energy Mater* **2021**, *11* (42). DOI: ARTN 2101973
10.1002/aenm.202101973.

(79) Saki, Z.; Byranvand, M. M.; Taghavinia, N.; Kedia, M.; Saliba, M. Solution-processed perovskite thin-films: the journey from lab- to large-scale solar cells. *Energ Environ Sci* **2021**, *14* (11), 5690-5722. DOI: 10.1039/d1ee02018h.

(80) Chilvery, A.; Das, S.; Guggilla, P.; Brantley, C.; Sunda-Meya, A. A perspective on the recent progress in solution-processed methods for highly efficient perovskite solar cells. *Sci Technol Adv Mat* **2016**, *17* (1), 650-658. DOI: 10.1080/14686996.2016.1226120.

(81) Cao, X. B.; Zhi, L. L.; Jia, Y.; Li, Y. H.; Zhao, K.; Cui, X.; Ci, L. J.; Zhuang, D. M.; Wei, J. Q. A Review of the Role of Solvents in Formation of High-Quality Solution-Processed Perovskite Films. *Acs Applied Materials & Interfaces* **2019**, *11* (8), 7639-7654. DOI: 10.1021/acsami.8b16315.

(82) Sum, T. C.; Mathews, N.; Xing, G. C.; Lim, S. S.; Chong, W. K.; Giovanni, D.; Dewi, H. A. Spectral Features and Charge Dynamics of Lead Halide Perovskites: Origins and Interpretations. *Accounts Chem Res* **2016**, *49* (2), 294-302. DOI: 10.1021/acs.accounts.5b00433.

(83) Price, M. B.; Butkus, J.; Jellicoe, T. C.; Sadhanala, A.; Briane, A.; Halpert, J. E.; Broch, K.; Hodgkiss, J. M.; Friend, R. H.; Deschler, F. Hot-carrier cooling and photoinduced refractive index changes in organic-inorganic lead halide perovskites. *Nat Commun* **2015**, *6*. DOI: ARTN 8420
10.1038/ncomms9420.

(84) Kandada, A. R. S.; Petrozza, A. Photophysics of Hybrid Lead Halide Perovskites: The Role of Microstructure. *Accounts Chem Res* **2016**, *49* (3), 536-544. DOI: 10.1021/acs.accounts.5b00464.

(85) Sun, S. J.; Fang, Y. N.; Kieslich, G.; White, T. J.; Cheetham, A. K. Mechanical properties of organic-inorganic halide perovskites, CH
NH

PbX
(X = I, Br and Cl), by nanoindentation. *J Mater Chem A* **2015**, *3* (36), 18450-18455. DOI: 10.1039/c5ta03331d.

(86) Dolabella, S.; Borzí, A.; Dommann, A.; Neels, A. Lattice Strain and Defects Analysis in Nanostructured Semiconductor Materials and Devices by High-Resolution X-Ray Diffraction: Theoretical and Practical Aspects. *Small Methods* **2022**, *6* (2). DOI: ARTN 2100932 10.1002/smtd.202100932.

(87) Zhu, C.; Niu, X. X.; Fu, Y. H.; Li, N. X.; Hu, C.; Chen, Y. H.; He, X.; Na, G. R.; Liu, P. F.; Zai, H. C.; et al. Strain engineering in perovskite solar cells and its impacts on carrier dynamics. *Nat Commun* **2019**, *10*. DOI: ARTN 815 10.1038/s41467-019-08507-4.

(88) Wang, D.; Yang, H. G.; Kitamura, T.; Nakashima, H. Influence of freely diffusing excitons on the photoluminescence spectrum of Si thick films with depth distribution of strain. *J Appl Phys* **2010**, *107* (3). DOI: Artn 033511 10.1063/1.3305463.

(89) Morris, D.; Roth, A. P.; Masut, R. A.; Lacelle, C.; Brebner, J. L. Photoluminescence Study of Strain Relaxation in Ga1-Xinxas/Gaas Single Heterostructures. *J Appl Phys* **1988**, *64* (8), 4135-4140. DOI: Doi 10.1063/1.341324.

(90) Huang, Y.; Sun, Q. D.; Xu, W.; He, Y.; Yin, W. J. Halide Perovskite Materials for Solar Cells: a Theoretical Review. *Acta Phys-Chim Sin* **2017**, *33* (9), 1730-1751. DOI: 10.3866/Pku.Whxb201705042.

(91) Meloni, S.; Palermo, G.; Ashari-Astani, N.; Grätzel, M.; Rothlisberger, U. Valence and conduction band tuning in halide perovskites for solar cell applications. *J Mater Chem A* **2016**, *4* (41), 15997-16002. DOI: 10.1039/c6ta04949d.

(92) Kim, H. S.; Park, N. G. Importance of tailoring lattice strain in halide perovskite crystals. *Npg Asia Mater* **2020**, *12* (1). DOI: ARTN 78 10.1038/s41427-020-00265-w.

(93) Hickey, C. L.; Grumstrup, E. M. Reduced Artifact Approach for Determining Diffusion Coefficients in Time-Resolved Microscopy. *J Phys Chem C* **2020**, *124* (25), 14016-14021. DOI: 10.1021/acs.jpcc.0c02302.

(94) Randle, V. Applications of electron backscatter diffraction to materials science: status in 2009. *J Mater Sci* **2009**, *44* (16), 4211-4218. DOI: 10.1007/s10853-009-3570-0.

(95) Wright, S. I.; Nowell, M. M.; Field, D. P. A Review of Strain Analysis Using Electron Backscatter Diffraction. *Microsc Microanal* **2011**, *17* (3), 316-329. DOI: 10.1017/S1431927611000055.

(96) Baba-Kishi, K. Z. Review - Electron backscatter Kikuchi diffraction in the scanning electron microscope for crystallographic analysis. *J Mater Sci* **2002**, *37* (9), 1715-1746. DOI: Doi 10.1023/A:1014964916670.

(97) Winkelmann, A.; Cios, G.; Tokarski, T.; Nolze, G.; Hielscher, R.; Koziel, T. EBSD orientation analysis based on experimental Kikuchi reference patterns. *Acta Mater* **2020**, *188*, 376-385. DOI: 10.1016/j.actamat.2020.01.053.

(98) Saowadee, N.; Agersted, K.; Bowen, J. R. Lattice constant measurement from electron backscatter diffraction patterns. *J Microsc-Oxford* **2017**, *266* (2), 200-210. DOI: 10.1111/jmi.12529.

(99) Zhang, Q. P.; Couloigner, I. Accurate centerline detection and line width estimation of thick lines using the radon transform. *Ieee T Image Process* **2007**, *16* (2), 310-316. DOI: 10.1109/Tip.2006.887731.

(100) Paternain, G. P.; Salo, M.; Uhlmann, G. The Radon Transform in the Plane. *Cam St Ad M* **2023**, *204*, 1-24. DOI: Book_Doi 10.1017/9781009039901.

(101) Shen, P. C.; Liu, H.; Zhuang, Z. Y.; Zeng, J. J.; Zhao, Z. J.; Tang, B. Z. Through-Space Conjugated Electron Transport Materials for Improving Efficiency and Lifetime of Organic Light-Emitting Diodes. *Adv Sci* **2022**, *9* (15). DOI: ARTN 2200374 10.1002/advs.202200374.

(102) Schrimpf, W.; Ossato, G.; Hirschle, P.; Wuttke, S.; Lamb, D. C. Investigation of the Co-Dependence of Morphology and Fluorescence Lifetime in a Metal-Organic Framework. *Small* **2016**, *12* (27), 3651-3657. DOI: 10.1002/smll.201600619 From NLM PubMed-not-MEDLINE.

(103) Chen, X.; Jagadesan, P.; Valandro, S.; Hupp, J. T.; Schanze, K. S.; Goswami, S. Identifying the Polymorphs of Zr-Based Metal–Organic Frameworks via Time-Resolved Fluorescence Imaging. *ACS Materials Letters* **2022**, *4* (2), 370-377. DOI: 10.1021/acsmaterialslett.1c00754.

(104) Ameloot, R.; Vermoortele, F.; Hofkens, J.; De Schryver, F. C.; De Vos, D. E.; Roeffaers, M. B. Three-dimensional visualization of defects formed during the synthesis of metal-organic frameworks: a fluorescence microscopy study. *Angewandte Chemie* **2013**, *52* (1), 401-405. DOI: 10.1002/anie.201205627 From NLM PubMed-not-MEDLINE.

(105) Fang, Z. L.; Bueken, B.; De Vos, D. E.; Fischer, R. A. Defect-Engineered Metal-Organic Frameworks. *Angew Chem Int Edit* **2015**, *54* (25), 7234-7254. DOI: 10.1002/anie.201411540.

(106) Rajasree, S. S.; Yu, J.; Pratik, S. M.; Li, X.; Wang, R.; Kumbhar, A. S.; Goswami, S.; Cramer, C. J.; Deria, P. Superradiance and Directional Exciton Migration in Metal-Organic Frameworks. *Journal of the American Chemical Society* **2022**, *144* (3), 1396-1406. DOI: 10.1021/jacs.1c11979 From NLM PubMed-not-MEDLINE.

(107) Son, H. J.; Jin, S. Y.; Patwardhan, S.; Wezenberg, S. J.; Jeong, N. C.; So, M.; Wilmer, C. E.; Sarjeant, A. A.; Schatz, G. C.; Snurr, R. Q.; et al. Light-Harvesting and Ultrafast Energy Migration in Porphyrin-Based Metal-Organic Frameworks. *J Am Chem Soc* **2013**, *135* (2), 862-869. DOI: 10.1021/ja310596a.

(108) Deria, P.; Yu, J. R.; Balaraman, R. P.; Mashni, J.; White, S. N. Topology-dependent emissive properties of zirconium-based porphyrin MOFs. *Chem Commun* **2016**, *52* (88), 13031-13034. DOI: 10.1039/c6cc07343c.

(109) Rajasree, S. S.; Li, X. L.; Deria, P. Physical properties of porphyrin-based crystalline metal-organic frameworks. *Commun Chem* **2021**, *4* (1). DOI: ARTN 47 10.1038/s42004-021-00484-4.

(110) Goswami, S.; Chen, M.; Wasielewski, M. R.; Farha, O. K.; Hupp, J. T. Boosting Transport Distances for Molecular Excitons within Photoexcited Metal-Organic Framework Films. *Acs Applied Materials & Interfaces* **2018**, *10* (40), 34409-34417. DOI: 10.1021/acsami.8b14977.

(111) Gu, C.; Zhang, H.; Yu, J. H.; Shen, Q.; Luo, G. Q.; Chen, X.; Xue, P.; Wang, Z. B.; Hu, J. B. Assembled Exciton Dynamics in Porphyrin Metal-Organic Framework Nanofilms. *Nano Lett* **2021**, *21* (2), 1102-1107. DOI: 10.1021/acs.nanolett.0c04492.

(112) Skorupskii, G.; Le, K. N.; Cordova, D. L. M.; Yang, L. M.; Chen, T. Y.; Hendon, C. H.; Arguilla, M. Q.; Dinca, M. Porous lanthanide metal-organic frameworks with metallic conductivity. *P Natl Acad Sci USA* **2022**, *119* (34). DOI: ARTN e2205127119 10.1073/pnas.2205127119.

(113) Dong, R.; Han, P.; Arora, H.; Ballabio, M.; Karakus, M.; Zhang, Z.; Shekhar, C.; Adler, P.; Petkov, P. S.; Erbe, A.; et al. High-mobility band-like charge transport in a semiconducting two-dimensional metal-organic framework. *Nat Mater* **2018**, *17* (11), 1027-1032. DOI: 10.1038/s41563-018-0189-z From NLM PubMed-not-MEDLINE.

(114) Clough, A. J.; Skelton, J. M.; Downes, C. A.; de la Rosa, A. A.; Yoo, J. W.; Walsh, A.; Melot, B. C.; Marinescu, S. C. Metallic Conductivity in a Two-Dimensional Cobalt Dithiolene Metal–Organic Framework. *J Am Chem Soc* **2017**, *139* (31), 10863-10867. DOI: 10.1021/jacs.7b05742.

(115) Snider, J. L.; Su, J.; Verma, P.; El Gabaly, F.; Sugar, J. D.; Chen, L. N.; Chames, J. M.; Talin, A. A.; Dun, C. C.; Urban, J. J.; et al. Stabilized open metal sites in bimetallic metal-organic

framework catalysts for hydrogen production from alcohols. *J Mater Chem A* **2021**, *9* (17), 10869-10881. DOI: 10.1039/d1ta00222h.

(116) Yang, X.; Bonnett, B. L.; Spiering, G. A.; Cornell, H. D.; Gibbons, B. J.; Moore, R. B.; Foster, E. J.; Morris, A. J. Understanding the Mechanical Reinforcement of Metal-Organic Framework-Polymer Composites: The Effect of Aspect Ratio. *ACS applied materials & interfaces* **2021**, *13* (44), 51894-51905. DOI: 10.1021/acsami.1c05430 From NLM PubMed-not-MEDLINE.

(117) Nazri, S.; Khajeh, M.; Oveisi, A. R.; Luque, R.; Rodriguez-Castellon, E.; Ghaffari-Moghaddam, M. Thiol-functionalized PCN-222 MOF for fast and selective extraction of gold ions from aqueous media. *Sep Purif Technol* **2021**, *259*. DOI: ARTN 118197 10.1016/j.seppur.2020.118197.

(118) Hill, A. H.; Smyser, K. E.; Kennedy, C. L.; Massaro, E. S.; Grumstrup, E. M. Screened Charge Carrier Transport in Methylammonium Lead Iodide Perovskite Thin Films. *The Journal of Physical Chemistry Letters* **2017**, *8* (5), 948-953. DOI: 10.1021/acs.jpclett.7b00046.

(119) Mandal, A. K.; Taniguchi, M.; Diers, J. R.; Niedzwiedzki, D. M.; Kirmaier, C.; Lindsey, J. S.; Bocian, D. F.; Holten, D. Photophysical Properties and Electronic Structure of Porphyrins Bearing Zero to Four meso-Phenyl Substituents: New Insights into Seemingly Well Understood Tetrapyrroles. *J Phys Chem A* **2016**, *120* (49), 9719-9731. DOI: 10.1021/acs.jpca.6b09483.

(120) Grumstrup, E. M. Spatiotemporal coupling of excited state dynamics in time-resolved microscopies. *Opt Express* **2019**, *27* (22), 31385-31393. DOI: 10.1364/Oe.27.031385.

(121) Akselrod, G. M.; Prins, F.; Poulikakos, L. V.; Lee, E. M. Y.; Weidman, M. C.; Mork, A. J.; Willard, A. P.; Bulovic, V.; Tisdale, W. A. Subdiffusive Exciton Transport in Quantum Dot Solids. *Nano Lett* **2014**, *14* (6), 3556-3562. DOI: 10.1021/nl501190s.

(122) Bouchaud, J. P.; Georges, A. Anomalous Diffusion in Disordered Media - Statistical Mechanisms, Models and Physical Applications. *Phys Rep* **1990**, *195* (4-5), 127-293. DOI: Doi 10.1016/0370-1573(90)90099-N.

(123) Zhang, Q. Q.; Zhang, C. K.; Cao, L. Y.; Wang, Z.; An, B.; Lin, Z. K.; Huang, R. Y.; Zhang, Z. M.; Wang, C.; Lin, W. B. Forster Energy Transport in Metal-Organic Frameworks Is Beyond Step-by-Step Hopping. *J Am Chem Soc* **2016**, *138* (16), 5308-5315. DOI: 10.1021/jacs.6b01345.

(124) Deng, S.; Shi, E.; Yuan, L.; Jin, L.; Dou, L.; Huang, L. Long-range exciton transport and slow annihilation in two-dimensional hybrid perovskites. *Nature communications* **2020**, *11* (1), 664. DOI: 10.1038/s41467-020-14403-z.

(125) Pandya, R.; Chen, R. Y. S.; Gu, Q.; Gorman, J.; Auras, F.; Sung, J.; Friend, R.; Kukura, P.; Schnedermann, C.; Rao, A. Femtosecond Transient Absorption Microscopy of Singlet Exciton

Motion in Side-Chain Engineered Perylene-Diimide Thin Films. *J Phys Chem A* **2020**, *124* (13), 2721-2730. DOI: 10.1021/acs.jpca.0c00346 From NLM PubMed-not-MEDLINE.

(126) Bercegol, A.; Ory, D.; Suchet, D.; Cacovich, S.; Fournier, O.; Rousset, J.; Lombez, L. Quantitative optical assessment of photonic and electronic properties in halide perovskite. *Nature communications* **2019**, *10* (1), 1586. DOI: 10.1038/s41467-019-09527-w.

(127) Diab, H.; Arnold, C.; Ledee, F.; Trippe-Allard, G.; Delport, G.; Vilar, C.; Bretenaker, F.; Barjon, J.; Lauret, J. S.; Deleporte, E.; Garrot, D. Impact of Reabsorption on the Emission Spectra and Recombination Dynamics of Hybrid Perovskite Single Crystals. *J Phys Chem Lett* **2017**, *8* (13), 2977-2983. DOI: 10.1021/acs.jpclett.7b00998.

(128) Shaikh, S. M.; Usov, P. M.; Zhu, J.; Cai, M.; Alatis, J.; Morris, A. J. Synthesis and Defect Characterization of Phase-Pure Zr-MOFs Based on Meso-tetracarboxyphenylporphyrin. *Inorg Chem* **2019**, *58* (8), 5145-5153. DOI: 10.1021/acs.inorgchem.9b00200.

(129) Sholl, D. S.; Lively, R. P. Defects in Metal-Organic Frameworks: Challenge or Opportunity? *J Phys Chem Lett* **2015**, *6* (17), 3437-3444. DOI: 10.1021/acs.jpclett.5b01135.

(130) Afrin, S.; Yang, X.; Morris, A. J.; Grumstrup, E. M. Rapid Exciton Transport and Structural Defects in Individual Porphyrinic Metal Organic Framework Microcrystals. *J Am Chem Soc* **2024**, *146* (7), 4309-4313. DOI: 10.1021/jacs.3c12275 From NLM PubMed-not-MEDLINE.

(131) Afrin, S.; Yang, X. Z.; Morris, A. J.; Grumstrup, E. M. Rapid Exciton Transport and Structural Defects in Individual Porphyrinic Metal Organic Framework Microcrystals. *J Am Chem Soc* **2024**. DOI: 10.1021/jacs.3c12275.

(132) Mandal, A. K.; Taniguchi, M.; Diers, J. R.; Niedzwiedzki, D. M.; Kirmaier, C.; Lindsey, J. S.; Bocian, D. F.; Holten, D. Photophysical Properties and Electronic Structure of Porphyrins Bearing Zero to Four
-Phenyl Substituents: New Insights into Seemingly Well Understood Tetrapyrroles. *J Phys Chem A* **2016**, *120* (49), 9719-9731. DOI: 10.1021/acs.jpca.6b09483.

(133) Hashimoto, T.; Choe, Y.-K.; Nakano, H.; Hirao, K. Theoretical Study of the Q and B Bands of Free-Base, Magnesium, and Zinc Porphyrins, and Their Derivatives. *The Journal of Physical Chemistry A* **1999**, *103* (12), 1894-1904. DOI: 10.1021/jp984807d.

(134) Zimmermann, J.; Siggel, U.; Fuhrhop, J.-H.; Röder, B. Excitonic Coupling between B and Q Transitions in a Porphyrin Aggregate. *The Journal of Physical Chemistry B* **2003**, *107* (25), 6019-6021. DOI: 10.1021/jp0340865.

(135) Kasha, M.; Rawls, H. R.; El-Bayoumi, M. A. The exciton model in molecular spectroscopy. *Pure and Applied Chemistry* **1965**, *11* (3-4), 371-392. DOI: doi:10.1351/pac196511030371 (acccessed 2023-07-22).

(136) Keller, N.; Calik, M.; Sharapa, D.; Soni, H. R.; Zehetmaier, P. M.; Rager, S.; Auras, F.; Jakowetz, A. C.; Görling, A.; Clark, T.; Bein, T. Enforcing Extended Porphyrin J-Aggregate Stacking in Covalent Organic Frameworks. *Journal of the American Chemical Society* **2018**, *140* (48), 16544-16552. DOI: 10.1021/jacs.8b08088.

(137) Khairutdinov, R. F.; Serpone, N. Photoluminescence and Transient Spectroscopy of Free Base Porphyrin Aggregates. *The Journal of Physical Chemistry B* **1999**, *103* (5), 761-769. DOI: 10.1021/jp980869s.

(138) Xu, H.-Q.; Hu, J.; Wang, D.; Li, Z.; Zhang, Q.; Luo, Y.; Yu, S.-H.; Jiang, H.-L. Visible-Light Photoreduction of CO2 in a Metal–Organic Framework: Boosting Electron–Hole Separation via Electron Trap States. *Journal of the American Chemical Society* **2015**, *137* (42), 13440-13443. DOI: 10.1021/jacs.5b08773.

(139) Pratik, S. M.; Gagliardi, L.; Cramer, C. J. Engineering Electrical Conductivity in Stable Zirconium-Based PCN-222 MOFs with Permanent Mesoporosity. *Chem Mater* **2020**, *32* (14), 6137-6149. DOI: 10.1021/acs.chemmater.0c01847.

(140) Guo, Z.; Wan, Y.; Yang, M.; Snaider, J.; Zhu, K.; Huang, L. Long-range hot-carrier transport in hybrid perovskites visualized by ultrafast microscopy. *Science* **2017**, *356* (6333), 59-62. DOI: doi:10.1126/science.aam7744.

(141) Li, X. X.; Gong, C. H.; Gurzadyan, G. G.; Gelin, M. F.; Liu, J. X.; Sun, L. C. Ultrafast Relaxation Dynamics in Zinc Tetraphenylporphyrin Surface-Mounted Metal Organic Framework. *J Phys Chem C* **2018**, *122* (1), 50-61. DOI: 10.1021/acs.jpcc.7b08696.

(142) Kasha, M. Characterization of Electronic Transitions in Complex Molecules. *Discuss Faraday Soc* **1950**, (9), 14-19. DOI: DOI 10.1039/df9500900014.

(143) Carrasco, S.; Orcajo, G.; Martinez, F.; Imaz, I.; Arenas-Esteban, D.; Maspoch, D.; Bals, S.; Calleja, G.; Horcajada, P. Hf/porphyrin-based metal-organic framework PCN-224 for CO2 cycloaddition with epoxides. *Mater Today Adv* **2023**, *19*. DOI: ARTN 100390 10.1016/j.mtadv.2023.100390.

(144) Shaikh, S. M.; Chakraborty, A.; Alatis, J.; Cai, M.; Danilov, E.; Morris, A. J. Light harvesting and energy transfer in a porphyrin-based metal organic framework. *Faraday Discuss* **2019**, *216* (0), 174-190. DOI: 10.1039/c8fd00194d From NLM PubMed-not-MEDLINE.

APPENDICES

APPENDIX A

SUPPORTING INFORMATION FOR CHAPTER 4

Transient kinetics and pump probe image data collection

Transient kinetics and pump probe images were collected using a custom LabView software that interfaces to the hardware described above. The transient kinetics were polarization independent, aside from a slight variation in signal intensity, attributable to the larger extinction coefficient along the c axis relative to the a/b axes (see Figure S7 and S8). Diffusion measurements were collected for crystals oriented horizontally (relative to the optical table) to facilitate signal averaging. Generally, the fitted profiles (Figs. S5, S6) were collected by averaging of 20-30 individual 1 dimensional spatial scans of the pump to improve signal to noise.

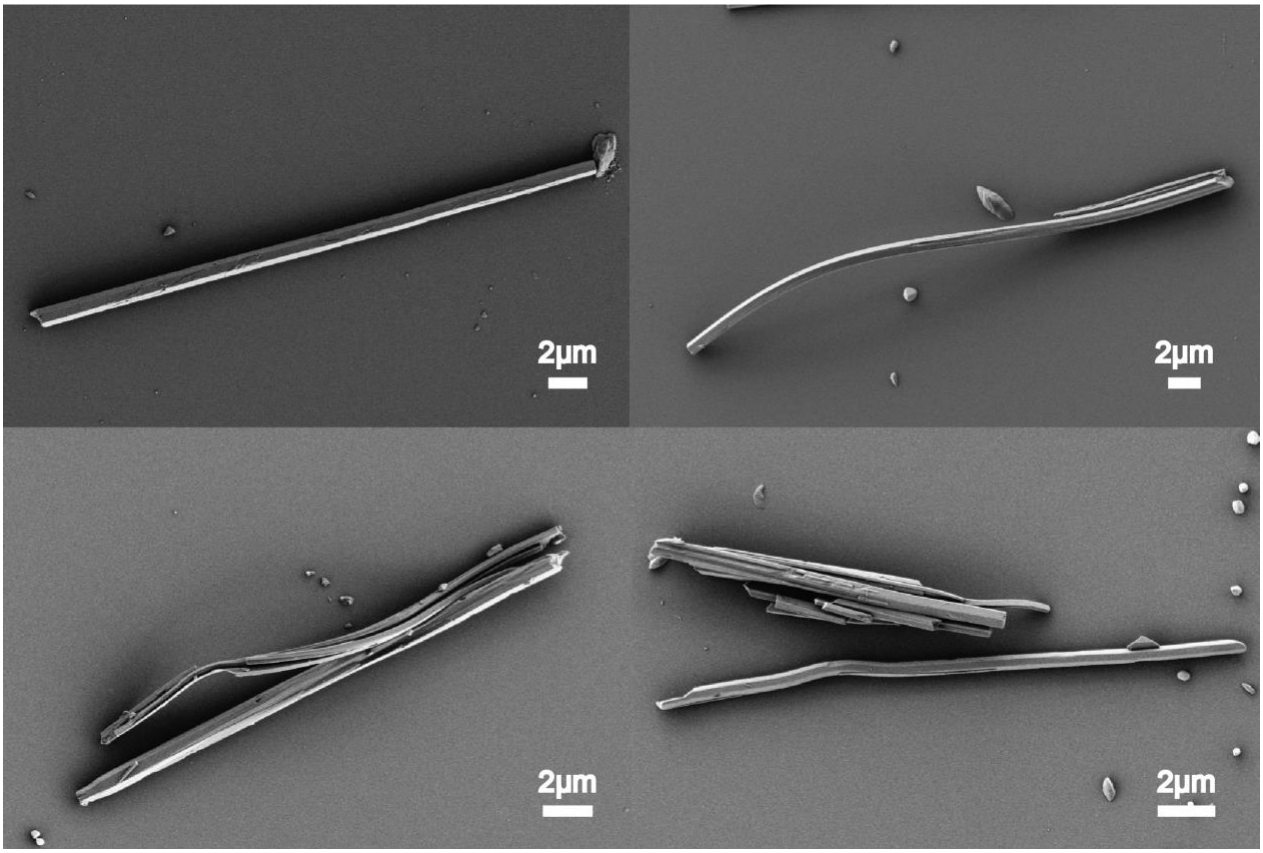

Fig. A1 FE-SEM images of PCN-222 microrods and bundles.

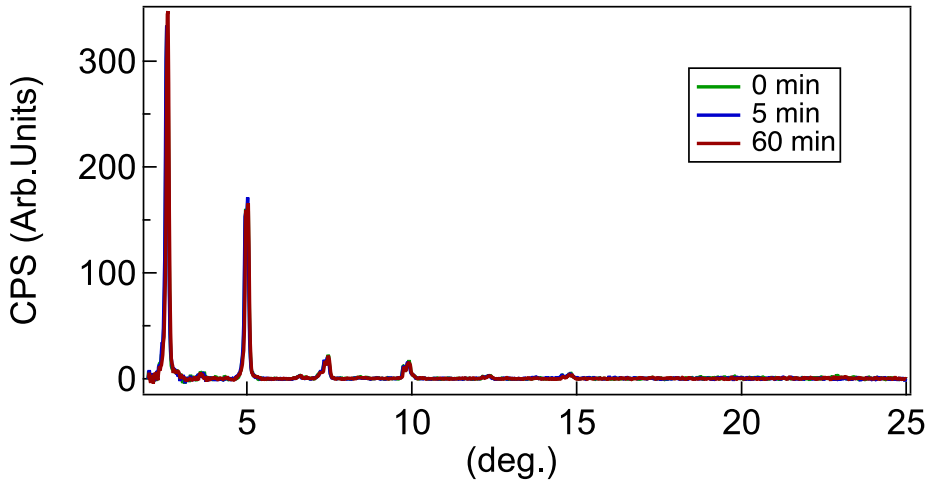

Fig. A2 Powder XRD pattern before and after 0, 5, and 60 minutes illumination with a Xe lamp continuum. Fluence was 42 mW/cm^2.

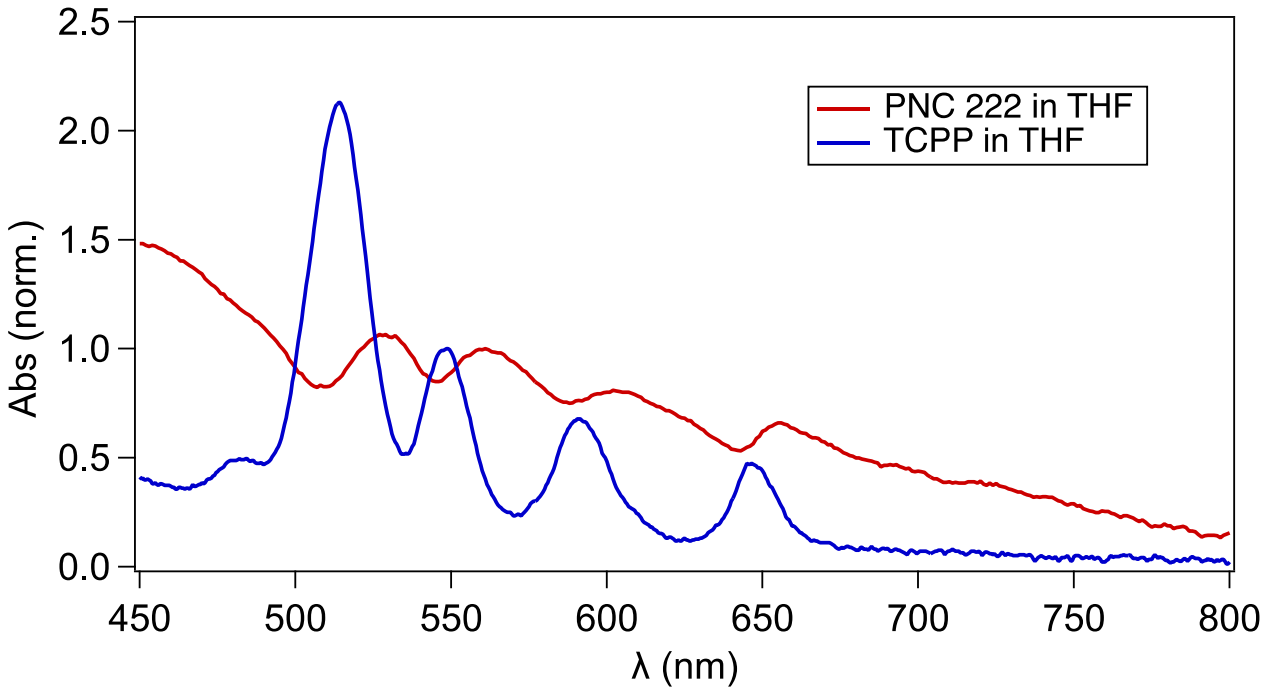

Fig. A3 UV vis absorption of TCPP linker and PCN-222 MOF.

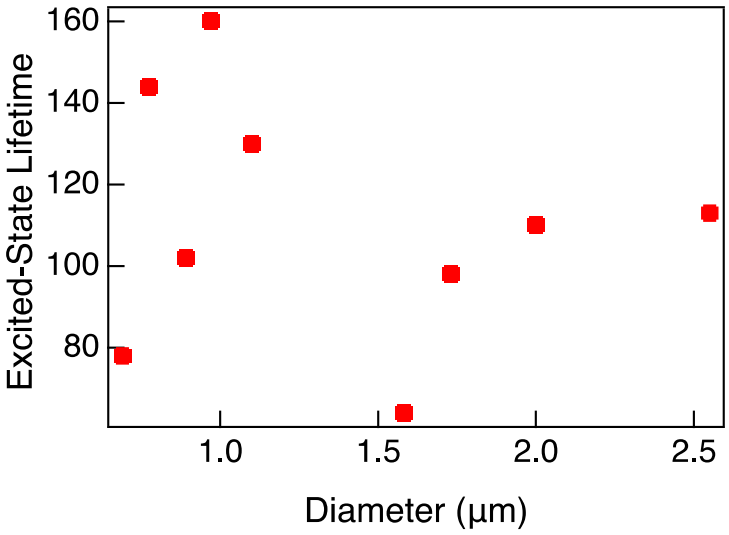

Fig. A4 A Correlation plot of average excited-state lifetime vs. rod diameter. No correlation is found, suggesting surface recombination is not relevant in PPM kinetics. Average lifetime is determined from a triple exponential fit according to $\langle \boldsymbol{\tau} \rangle = \sum_{i=1}^{3} \boldsymbol{a_i \tau_i} / \sum_{i=1}^{3} \boldsymbol{a_i}$.

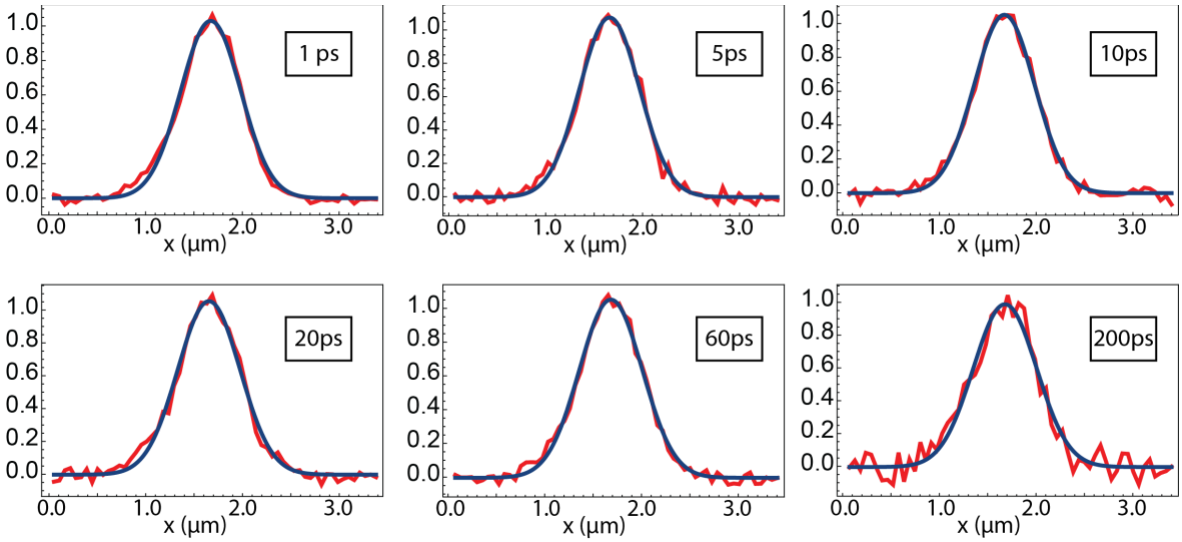

Fig. A5 Spatially separated ppm data (red) and fits (blue) used to extract MSD data in Fig 2c.

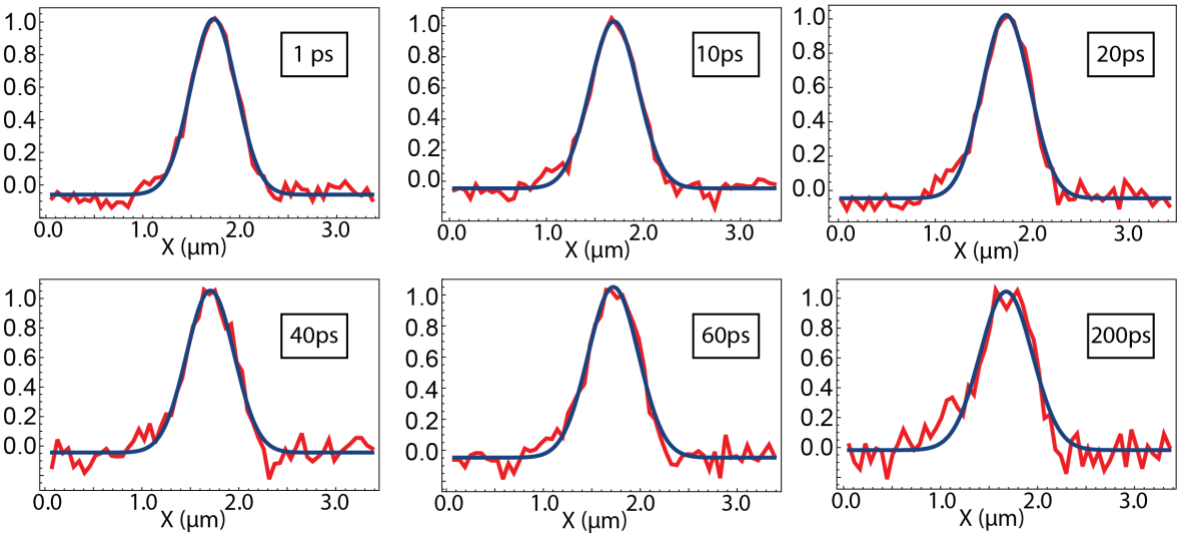

Fig. A6 Spatially separated ppm data (red) and fits (blue) used to extract MSD data in Fig 2d.

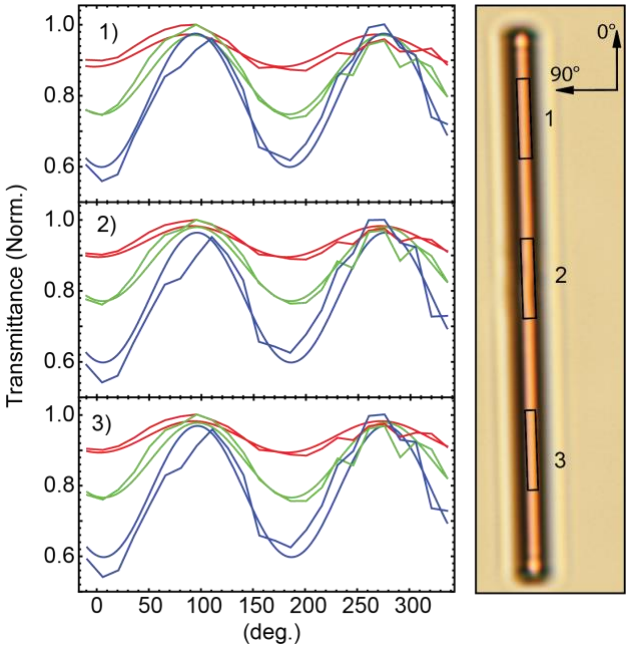

Fig. A7 Polarization dichroism of a straight rod. Maximum transmittance is orthogonal to the direction of crystal growth. The (fitted) minimum transmittance angle of the blue channel (of a rgb camera) for area 1, 2 and 3 are 2.32°, 1.41° and 1.76° degrees respectively.

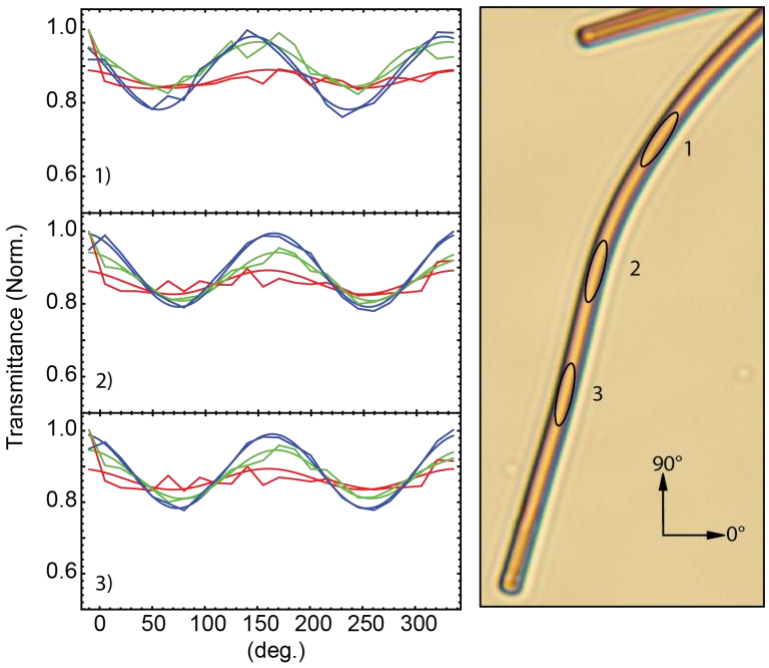

Fig. A8 Polarization dichroism of a bent rod. Maximum transmittance remains orthogonal to the long axis of the crystal. The (fitted) minimum transmittance angle of the blue pixels for area 1, 2 and 3 are 56.15°, 75.03° and 77.35° respectively, which follows the direction of crystal growth, indicating the c axis remains the preferential growth direction, despite the bend.

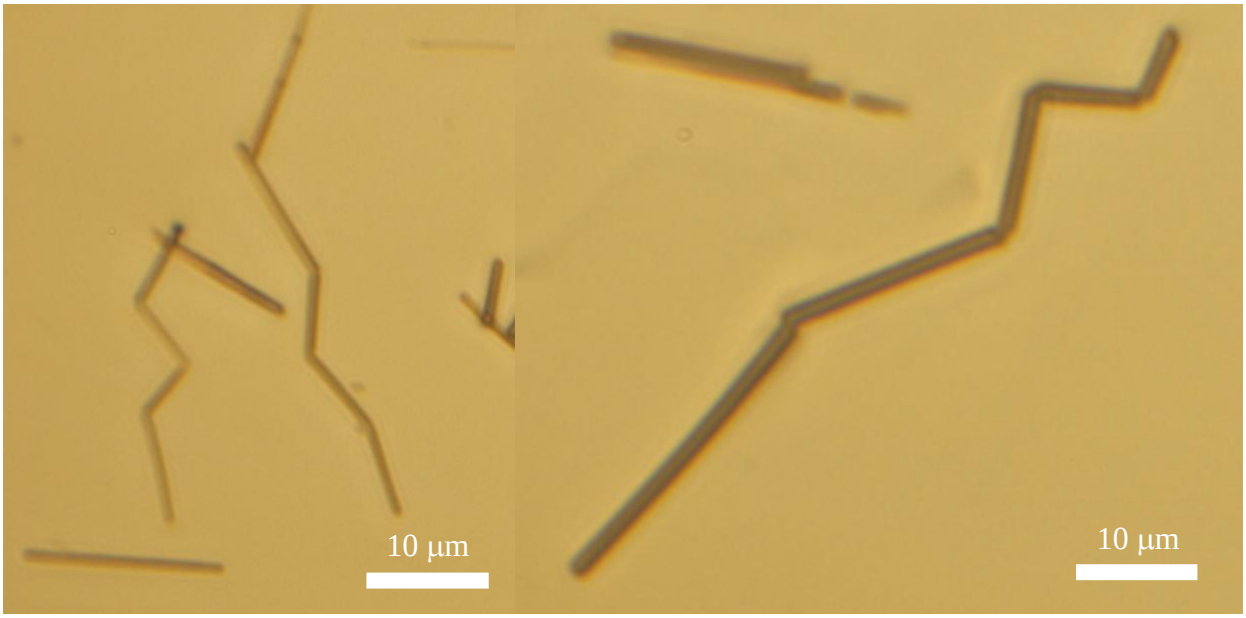

Fig. A9 Bright field microscopy images of PCN-222 rods deposited on pre-stretched flexible substrates made from poly-dimethyl siloxane. Upon relaxation of the substrate, the rods break into segments, indicating the structures are inflexible and brittle.

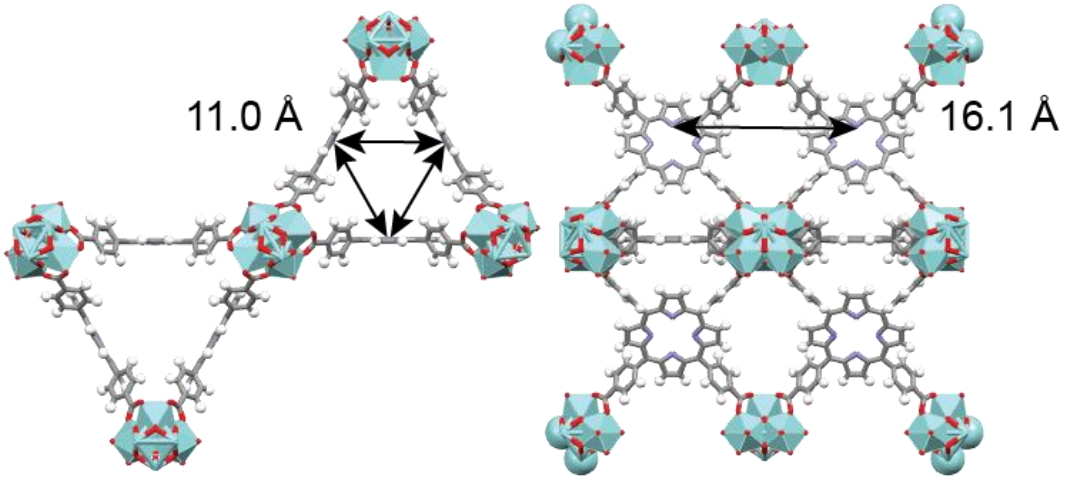

Fig. A10 Closest Chromophore distances

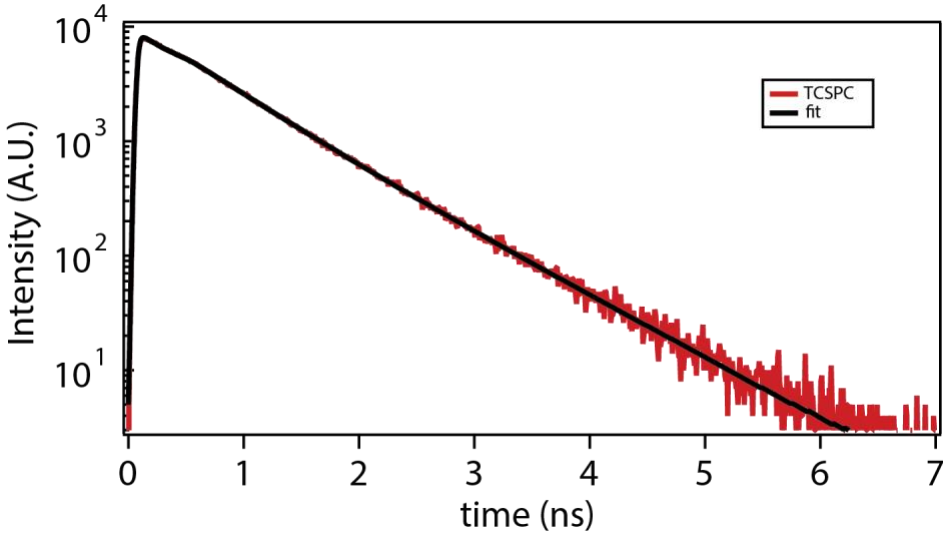

Fig. A11 Time correlated single photon counting. Excitation at 400 nm. Emission detected at 657 nm. The single exponential fit recovers a time constant of $\tau = 748\, ps$.

Estimation of Förster Rate

An estimation of the Förster-limited diffusion coefficient can be made by considering the Förster energy transfer rate. If we assume the Förster radius of the structurally analogous PCN-223, (R_0=5.45 nm)[144], an upper limit for the hopping rate is given by $k_{hop} = \frac{1}{\tau}\left(\frac{R_0}{r}\right)^6$, where τ is the PL lifetime. Using $\tau = 748\,ps$ from the fit of the TCSPC kinetics (Fig. S11), and r = 1.61 nm (for c-axis diffusion) from the crystal structure (Fig. S10) yields $k_{hop} = 2\,ps^{-1}$. Assuming 1D site-to-site diffusion ($D = \frac{1}{2}r^2 k_{hop}$), $D = 2.6 \times 10^{-2}\,cm^2/s$, approximately a factor of 20 slower than that observed. This discrepancy suggests that exciton transport, particularly at early times, proceeds through states that are more strongly coupled than that assumed by the point dipole Förster mechanism.

Trace	A_1	A_2	A_3	τ_1(ps)	τ_2 (ps)	τ_3 (ps)
Red (1)	0.09± 0.01	0.53± 0.01	0.38±0.01	1.97 ± 0.52	61.1 ± 2.5	656.2 ± 55.2
Red (2)	0.06± 0.01	0.47± 0.01	0.46±0.01	1.95 ± 0.80	47.8 ± 2.0	519.1 ± 23.4
Red (3)	0.16± 0.01	0.45± 0.01	0.38±0.01	5.08 ± 0.51	65.5 ± 3.3	609.8 ± 45
Green (1)	0.21 ± 0.01	0.36± 0.01	0.43±0.01	3.37 ± 0.39	47.1 ± 2.8	443.9 ± 20.5
Green (2)	0.18 ± 0.01	0.37 ± 0.01	0.45±0.01	1.77 ± 0.27	46.1 ± 2.7	322.5 ± 13.1
Green (3)	0.19± 0.01	0.44 ± 0.02	0.37±0.02	4.56 ± 0.64	61.7 ± 4.8	441.1 ± 41.8
Blue (1)	0.26 ± 0.01	0.55± 0.01	0.19±0.02	7.40 ± 0.67	69.4 ± 3.9	966.6 ± 264
Blue (2)	0.19± 0.01	0.53 ± 0.01	0.28±0.01	3.11 ± 0.38	53.6 ± 2.2	447.6 ± 35.7
Blue (3)	0.17± 0.01	0.50 ± 0.01	0.33±0.01	2.45 ± 0.29	46.6 ± 1.6	400.3 ± 18.8

Table A1 Fit parameters for kinetics shown in Figure 3B

trace	A_1	A_2	A_3	τ_1(ps)	τ_2(ps)	τ_3(ps)
black	0.27± 0.01	0.36± 0.01	0.37±0.01	2.50 ± 0.29	46.9 ± 3.1	533.9 ± 36.6
green	0.21± 0.01	0.37± 0.01	0.42±0.01	1.91 ± 0.27	39.6 ± 2.2	447.7 ± 20.6
blue	0.22± 0.01	0.38± 0.01	0.40±0.01	2.63 ± 0.37	37.3 ± 2.0	447.9 ± 19.0
red	0.23± 0.01	0.39± 0.01	0.38±0.01	4.07 ± 0.48	44.3 ± 2.8	457.7 ± 25.6

Table A2 Fit parameters for kinetics shown in Figure 4G

trace	A_1	A_2	A_3	τ_1 (ps)	τ_2 (ps)	τ_3 (ps)
red	0.20 ± 0.00	0.48± 0.00	0.32±0.01	2.38 ± 0.15	39.2± 0.7	495.5 ± 13.1
black	0.23± 0.00	0.49 ± 0.00	0.28±0.01	2.47± 0.14	39.2 ± 0.7	556.1 ± 17.0
blue	0.26± 0.01	0.54± 0.01	0.19±0.01	2.90 ± 0.16	35.6 ± 0.8	254.1 ± 10.1
green	0.25± 0.01	0.51± 0.01	0.23±0.01	4.34± 0.27	38.5± 1.0	372.8 ± 14.1

Table A3 Fit parameters for kinetics shown in Figure 4H

APPENDIX B

SUPPORTING INFORMATION FOR CHAPTER 5

Figure B1: Normalized relaxation kinetics collected from the domain showed in figure 5.3 panel A

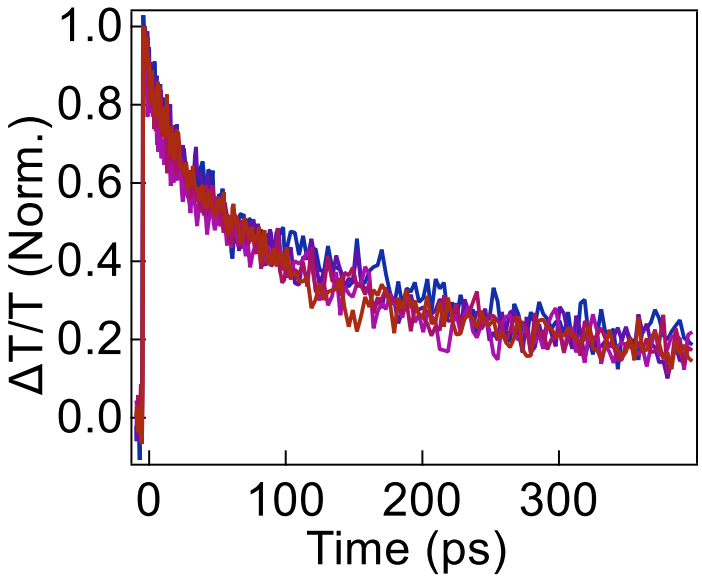

Spot	A1	A2	Tao1(ps)	Tao2(ps)
1	0.32±0.04	0.52±0.01	17.18±2	179.39±26.1
2	0.26 ±0.03	0.51±0.02	17.55±4.4	192.31±54.3
3	0.32±0.02	0.52±0.01	24.45±3.2	187.2±34
4	0.34±0.01	0.49±0.01	17.73±33	260.07±24
5	0.27±0.02	0.52±0.02	18.36±1.8	213.18±14.1
6	0.22±0.01	0.54±0.02	12.78±2.2	133.7±11.7
7	0.25±0.02	0.63±0.01	15.1±1.73	130.15±12.4
8	0.17±0.01	0.52±0.02	8.98±1.83	97.94±4.84

Table B1: Fit parameters for kinetics shown in Figure B1

Figure B2: Normalized power-dependent broadband decay kinetics for 517nm photoexcitation, probed at 626nm.

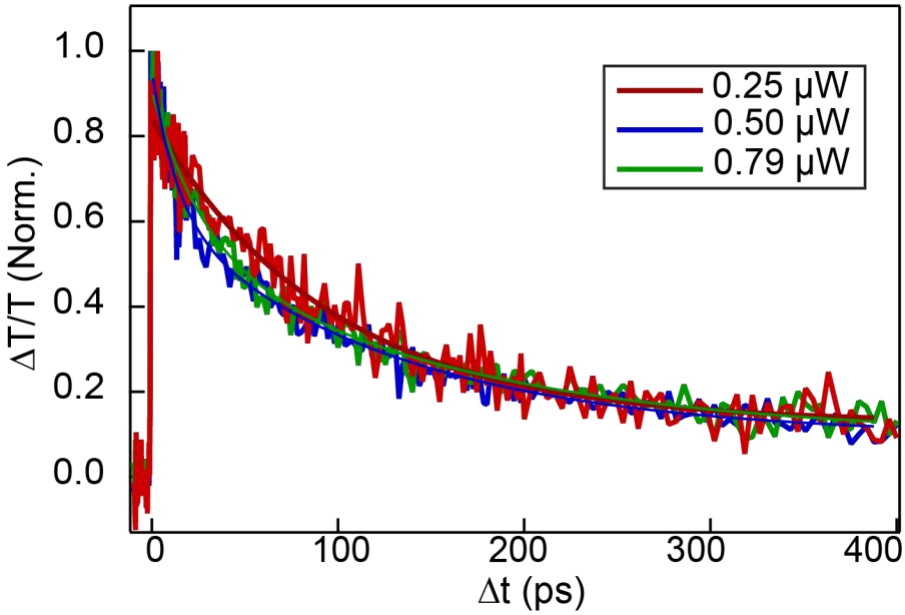

Figure B3: Thermogravimetric curve of PCN-222

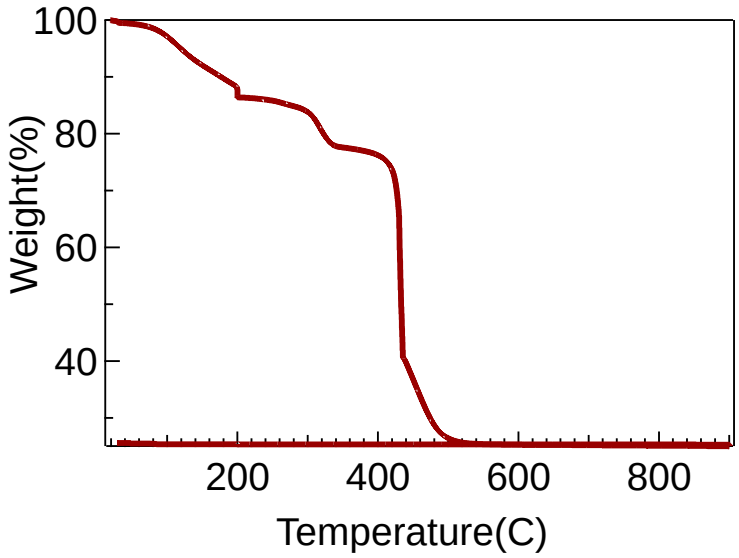

Thermogravimetric analysis (TGA) :

TGA in Figure B3 demonstrated the weight loss of the sample used in this work. For PCN-222, the initial weight loss below 200°C is due to the evaporation of acetone from the pores, followed by a gradual loss associated with DMF. The dehydroxylation of the Zr_6O_8 node occurs at 327°C. At 470°C, the TCPP ligands decompose, leaving only ZrO_2 behind. From the remaining molecular weight of ZrO_2, we estimated the molecular weight of PCN-222. Comparing the estimated weight with the actual weight of PCN-222, we had projected the number of missing linkers in our sample was ~7%.

trace	A0	A1	Tao1	Tao2	Tao3
black	0.10228	0.485	10.088	122.27	539.66
purple	0.044016	0.55564	17.326	117.18	796.04
green	0.032065	0.43044	0.84992	70.313	1123.4
blue	0.037772	0.61739	2.10	53.19	970.57
red	0.15325	0.53329	4.1666	55.281	453.95

Table B2: Fit parameters for kinetics are shown in Figure 5.4 panel B

trace	A1	A2	Tao1	Tao2
black	0.15437	0.70266	79.27	82.027
purple	0.41067	0.39113	146.4	187.23
green	0.082775	0.68986	26.18	156.15
blue	0.39236	0.77274	89.699	687.55
red	0.375	0.35476	179.77	178.06

Table B3: Fit parameters for kinetics are shown in Figure 5.4 panel C